

11-2018

Variable Fidelity Studies in Wake Vortex Evolution, Safety, and Control

Petr Kazarin

Follow this and additional works at: <https://commons.erau.edu/edt>



Part of the [Space Vehicles Commons](#)

Scholarly Commons Citation

Kazarin, Petr, "Variable Fidelity Studies in Wake Vortex Evolution, Safety, and Control" (2018).
Dissertations and Theses. 429.
<https://commons.erau.edu/edt/429>

This Dissertation - Open Access is brought to you for free and open access by Scholarly Commons. It has been accepted for inclusion in Dissertations and Theses by an authorized administrator of Scholarly Commons. For more information, please contact commons@erau.edu.

VARIABLE FIDELITY STUDIES IN WAKE VORTEX EVOLUTION, SAFETY,
AND CONTROL

A Dissertation

Submitted to the Faculty

of

Embry-Riddle Aeronautical University

by

Petr Kazarin

In Partial Fulfillment of the

Requirements for the Degree

of

Doctor of Philosophy in Aerospace Engineering

November 2018

Embry-Riddle Aeronautical University

Daytona Beach, Florida

**VARIABLE FIDELITY STUDIES IN WAKE VORTEX EVOLUTION, SAFETY,
AND CONTROL**

By

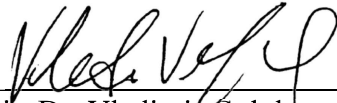
Petr Kazarin

This Dissertation was prepared under the direction of the candidate's Dissertation Committee Chair, Dr. Vladimir Golubev, Department of Aerospace Engineering, and has been approved by the members of the dissertation committee. It was submitted to College of Engineering and was accepted in partial fulfillment of the requirements for the

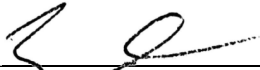
Degree of

Doctor of Philosophy in Aerospace Engineering

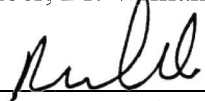
DISSERTATION COMMITTEE



Chair, Dr. Vladimir Golubev



Member, Dr. William MacKunis



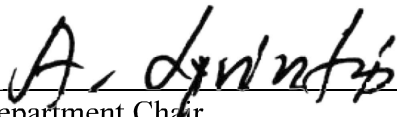
Member, Dr. Reda Mankbadi



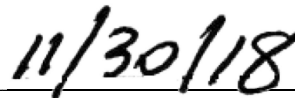
Member, Dr. Nashat Ahmad



Member, Dr. William Engblom



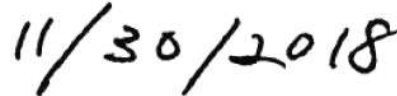
Department Chair,
Dr. Tasos Lyrintzis



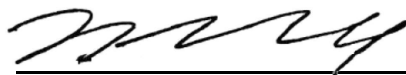
Date



Dean, College of Engineering,
Dr. Maj Mirmirani



Date



Senior Vice President for
Academic Affairs and Provost,
Dr. Lon D. Moeller



Date

ACKNOWLEDGMENTS

I owe my deepest gratitude to my advisor Professor Vladimir Golubev for establishing an environment of initiative and creative thinking. His technical and editorial advice was essential to the completion of this dissertation and has taught me innumerable lessons and insights on the workings of academic research in general. In addition, I would like to thank Professor Tasos Lyrintzis for making it possible to carry out this work in his department, who have been supportive of my career goals and worked actively to provide me with the protected academic time to pursue those goals. I would also like to acknowledge valuable suggestions and help from my committee members: Dr. William Engblom and Dr. Reda Mankbadi. Special thanks go to Dr. William MacKunis for the support, help, and guidance in nonlinear robust controller development. The author would like to acknowledge collaboration and useful discussions with members of FAA SSMT program, Sherry Borener, Alex Suchkov, Anton Provalov and Dmitry Zababurin. Special thanks go to Dr. Nashat Ahmad (NASA) in preparation of this work. I must also thank my colleague Professor Ebenezer Gnanamanickam for useful distractions since without him fewer basketball games would have been played. More importantly, I am thankful to him for giving me the opportunity to work in the wind tunnel lab and for his involvement in my future career. Above ground, I am grateful to my parents and my wife who believed in me, supported me in every possible way and showed great patience throughout these years. This research was supported in part through computational resources provided by Information Technology at Embry-Riddle Aeronautical University, Daytona Beach, Florida. The Rigel and Vega clusters were used for the presented CFD simulations.

TABLE OF CONTENTS

	Page
LIST OF TABLES	vi
LIST OF FIGURES	vii
ABBREVIATIONS	x
ABSTRACT	xii
1 INTRODUCTION	1
2 ADVANCES IN SITAR WVSS LOW FIDELITY MODELING	4
2.1 Safety Assessment Model Implementation	4
2.2 Wake Vortex Generation and Evolution Modeling	5
2.2.1 Deterministic and Probabilistic Approaches	9
2.2.2 Results and Comparison with Other Models	14
2.3 Dynamic Model of Aircraft Entering a Wake Vortex	20
2.4 Wake Vortex Encounter Predictions	22
2.5 Benchmark Case Study Scenario for Wake Induced UAS Reaction and Response	23
3 HIGH FIDELITY MODELING: EFFECTS OF GROUND SURFACE CONDITIONS ON AIRCRAFT WAKE VORTEX EVOLUTION	27
3.1 Numerical Formulation	30
3.1.1 Numerical Method	30
3.1.2 Wake Vortex Pair Initialization	31
3.1.3 List of Simulations	33
3.1.4 Computational Domains and Boundary Conditions	35
3.1.5 Grid Sensitivity Study	36
3.2 Wake Vortex Evolution with Different Ground Surfaces	38
3.2.1 Solid Flat Ground Surface	38
3.2.2 Comparison with Experimental Data	42
3.2.3 Forest Canopy	43
3.2.4 Forest Canopy Parametric Study	45
3.2.5 Water Surface	60
3.2.6 Comparison and Discussion of Results	61
3.3 High-Fidelity Based Reduced Order Model of In-ground Effects for WVSS	64
3.3.1 Reduced-order model approach	65
3.3.2 Comparison with APA 3.8 Fast-Time Model	67
4 ROBUST NONLINEAR TRACKING CONTROL FOR UNMANNED AIRCRAFT WITH VIRTUAL CONTROL SURFACES	79
4.1 Mathematical Model	81
4.2 Nonlinear Robust Control	85

	Page
4.2.1 Control Objective	85
4.2.2 Robust Controller Development	86
4.2.3 Observer Design	89
4.3 Numerical simulation	90
4.3.1 Linear, Parameter-Varying Model	90
4.3.2 H_∞ Linear Controller	91
4.3.3 Simulation	93
4.4 Wake Vortex Modeling	95
4.5 Results	96
4.5.1 Interaction with Wake Vortex. Take-off and Landing Phases	98
4.5.2 Interaction with Wake Vortex. Steady Level Flight Phase	100
4.5.3 The Simulations with Parametric Uncertainty	110
5 CONCLUSION	119
REFERENCES	123

LIST OF TABLES

Table	Page
2.1 RMS, MAE, BIAS for Denver' 03 data set (OGE)	17
2.2 RMS, MAE, BIAS (Memphis' 95 data set)	17
2.3 Success rates (Memphis' 95 data set) (Γ_0 0.9-1.25)	20
2.4 Success rates (Denver' 03 data set) (Γ_0 0.9-1.25)	20
2.5 UAV characteristics parameters used in simulations	23
3.1 Initial vortex parameters	32
3.2 Initial vortex parameters	32
3.3 Simulations and numerical setup parameters	33
3.4 Simulations and numerical setup parameters for the canopy study	34
3.5 Grids employed for grid sensitivity study	37
3.6 Grids employed for grid sensitivity study	38
3.7 Initial vortex parameters.	43
4.1 Average states' RMSE and Maximum Deviations of Deflection Surfaces over 400 Monte Carlo simulations. $\bar{t} = 5$	109
4.2 Average states' RMSE and Maximum Deviations of Deflection Surfaces over 400 Monte Carlo simulations. $\bar{t} = 3.84$	109
4.3 Average states' RMSE and Maximum Deviations of Deflection Surfaces over 400 Monte Carlo simulations. $\bar{t} = 2.14$	110
4.4 Average states' RMSE and Maximum Deviations of Deflection Surfaces over 400 Monte Carlo simulations. Equilibrium point #7. $\bar{t} = 3.84$	111
4.5 Average states' RMSE and Maximum Deviations of Deflection Surfaces over 400 Monte Carlo simulations. Equilibrium point #8. $\bar{t} = 2.14$	111

LIST OF FIGURES

Figure	Page
2.1 Wake vortex rings behind the leader aircraft.	6
2.2 Vertical profiles of EDR and potential temperature gradient.	12
2.3 EDR and potential temperature gradient histograms.	13
2.4 PDFs of generated constant vertical profiles.	14
2.5 Generated constant profiles.	15
2.6 Deterministic wake vortex evolution simulations for case 1167.	16
2.7 Ultra Stick 120. Source: UAV Laboratories, University of Minnesota. . .	17
2.8 Wake vortex evolution 2σ bounds based on 400 M-C simulations.	18
2.9 RMS-based wake vortex evolution bounds.	18
2.10 P2P-based wake vortex evolution bounds.	19
2.11 Wake vortex induced Roll Control Ratio (RCR) contours.	24
2.12 Maximum bank deviations for Osprey , Predator and Global Hawk. . . .	26
3.1 The rough porous surface.	34
3.2 Position comparison with light detection and ranging system (LIDAR) data.	37
3.3 Circulation comparison with LIDAR data.	37
3.4 Grid sensitivity study.	39
3.5 Wake vortex evolution with flat ground. Q isosurfaces.	40
3.6 Position comparison with LIDAR data.	41
3.7 Circulation comparison with LIDAR data.	41
3.8 Comparison with the experimental data.	43
3.9 Position and $\bar{\Gamma}_{5-15}$ over the flat surfaces.	47
3.10 Vorticity fields for $\bar{t} = 1.26$, $\bar{x}^* = 2.04$	48
3.11 Vorticity fields for $\bar{t} = 3.78$, $\bar{x}^* = 2.04$	49
3.12 Position and $\bar{\Gamma}_{5-15}$ over the flat porous surfaces of different height. . . .	51
3.13 Vorticity fields for $\bar{t} = 1.03$, $\bar{x}^* = 2.04$	52
3.14 Vorticity fields for $\bar{t} = 2.86$, $\bar{x}^* = 2.04$	53

Figure	Page
3.15 Position and $\bar{\Gamma}_{5-15}$ over the flat porous surfaces of different height.	54
3.16 $Q = 0.5$ isosurface with vorticity coloring, $\bar{t} = 1.03$	55
3.17 $Q = 0.5$ isosurface with vorticity coloring, $\bar{t} = 2.06$	55
3.18 Vorticity fields for $\bar{t} = 0.69$, $\bar{x}^* = 2.04$	56
3.19 Vorticity fields for $\bar{t} = 1.72$, $\bar{x}^* = 1.72$	57
3.20 Position and $\bar{\Gamma}_{5-15}$ over the flat porous surfaces of different height.	59
3.21 Position and $\bar{\Gamma}_{5-15}$ over the forest clearing.	61
3.22 $Q = 0.1$ isosurfaces with vorticity coloring.	62
3.23 Position for three surfaces.	63
3.24 Circulation for three surfaces.	64
3.25 Circulation evolution for three surfaces.	68
3.26 Circulation evolution for three surfaces.	69
3.27 Wake vortex evolution with flat ground. Q isosurfaces ($ Q = 0.5$).	70
3.28 Wake vortex evolution with flat ground. Q isosurfaces ($ Q = 0.5$).	71
3.29 2D computational grid.	72
3.30 Interpolated, simulated and modeled points.	72
3.31 Position and strength for vertical interpolation points.	73
3.32 Position and strength for horizontal interpolation points.	74
3.33 Position and strength for diagonal and 4-points interpolation.	75
3.34 $\Gamma = 200 \text{ m}^2/\text{s}, b = 30\text{m}$. LES simulation (Red), APA 3.8 (Blue).	76
3.35 $\Gamma = 300 \text{ m}^2/\text{s}, b = 40\text{m}$. LES simulation (Red), APA 3.8 (Blue).	77
3.36 $\Gamma = 400 \text{ m}^2/\text{s}, b = 50\text{m}$. LES simulation (Red), APA 3.8 (Blue).	78
4.1 Seamless aircraft employing SJAs in a blended wing-body design.	80
4.2 Ultra Stick 120. Source: UAV Laboratories, University of Minnesota.	90
4.3 Varying parameter trajectory: set of equilibrium points for LPV model.	91
4.4 Elevator and throttle deflection frequency response to altitude and pitch rate for nominal system (red) and uncertain system (blue).	92
4.5 Control interconnection for linear design.	92

Figure	Page
4.6 (a) Highly turbulent case. $\Gamma_0 = 600m^2/s, t = 132s, h = 54.5m$ (b) Landing case. $\Gamma_0 = 300m^2/s, t = 60s, h = 37m$ (c) Take-off case. $\Gamma_0 = 300m^2/s, t = 42s, h = 13m$	101
4.7 States deviations for nominal trim point, highly turbulent case.	102
4.8 (a) Horizontal velocity and (b) Disturbance, highly turbulent case.	102
4.9 Deflection surfaces deviations	103
4.10 States deviations for nominal trim point, landing case.	104
4.11 (a) Horizontal velocity and (b) Disturbance, landing case.	104
4.12 Deflection surfaces deviations	105
4.13 States deviations for nominal trim point, take-off case.	106
4.14 (a) Horizontal velocity and (b) Disturbance, take-off case.	106
4.15 Deflection surfaces deviations	107
4.16 Wake vortex evolution results based on 400 Monte-Carlo simulations. The simulation is performed for $\bar{t} = 5$ (Blue dashed line).	109
4.17 States deviations (nominal trim point, MC simulations.	110
4.18 Generator aircraft and several positions of the follower aircraft.	111
4.19 Simulink model diagram.	112
4.20 States deviations for nominal point (23 m/s point), 17 m/s gust.	113
4.21 States deviations for 21 m/s point, 17 m/s gust.	114
4.22 Control surface deviations for nominal point (23 m/s point), 17 m/s gust.	115
4.23 Control surface deviations for 21 m/s point, 17 m/s gust.	115
4.24 States deviations for nominal point, 23 m/s gust.	116
4.25 Control surface deviations for nominal point , 23 m/s gust.	117
4.26 Control surface deviations for nominal point, 23 m/s gust, SJA case.	117
4.27 States deviations for nominal point, 23 m/s gust, SJA case.	118

ABBREVIATIONS

SITAR WVSS	safety investigation toolkit for analysis and reporting wake vortex safety system
NAS	national aerospace system
UAS	unmanned aerial systems
UAV	unmanned aerial vehicle
SSMT	system safety management transformation
ISAM	integrated safety assessment model
ESDs	event-sequence diagrams
FT	fault-tree
AVOSS	aircraft vortex spacing system
TASS	terminal area simulation system
APA	AVOSS wake vortex prediction algorithm
TDAWP	TASS driven algorithms for wake prediction
D2P	deterministic two-phase model
P2P	probabilistic two-phase model
DLR	deutsches zentrum fur luft- und raumfahrt (German Aerospace Center)
LIDAR	light detection and ranging
RMS	root mean square
AMD	average maximum deviation
MAE	mean absolute error
EDR	eddy dissipation rate
PDF	probability density function
PISO	pressure-implicit with splitting of operators
SIMPLE	semi-implicit method for pressure-linked equations
LES	large eddy simulation
IDDES	improved delayed detached eddy simulation
IGE	in-ground effect

OGE	out-of-ground-effect
NGE	near-ground-effect
VOF	volume-of-fluid approach
PISO	pressure implicit with splitting of operator
SIMPLE	semi-implicit method for pressure linked equations
SJA	synthetic jet actuators
LPV	linear parameter varying
M-C	Monte-Carlo

ABSTRACT

The purpose of this research is to develop a variable-fidelity approach for addressing the safety of unmanned aerial system (UAS) operations in the national aerospace system (NAS). This task is implemented on the basis of safety investigation toolkit for analysis and reporting wake vortex safety system (SITAR WVSS) code, which is a dynamic low-fidelity model addressing generation, evolution, and interaction of the leader-aircraft wake vortex with the follower-aircraft lifting surfaces.

The first part of the dissertation deals with the generation, evolution, and interaction of the wake vortices produced by an aircraft. In particular, it presents the results of the vortex safety analysis conducted for selected UAS operating alongside commercial aircraft in the terminal zone. The work further investigates and compares decay and transport of the wake vortex in the vicinity of various grounds including a solid surface, a forest canopy, and a water surface, representative of various terminal zone environments. The obtained high-fidelity results form the basis for reduced-order models to be integrated into the fast-analysis code under development for in-situ wake vortex safety predictions. The second part of the dissertation introduces a robust nonlinear control method that is proven to achieve altitude regulation in the presence of unmodeled external disturbances (e.g. wind gust, wake vortex disturbance) and actuator parametric uncertainty. This method is designed as a part of “Interaction” sub-module of the SITAR WVSS model. The results demonstrate the capability of the proposed nonlinear controller to asymptotically reject wind gust/wake-vortex disturbances and the parametric uncertainty. The proposed controller is a great choice for small UAV applications with limited computational resources.

1. INTRODUCTION

The Federal Aviation Administration (FAA) currently addresses a number of challenges presented by the integration of unmanned aircraft systems (UAS) in the National Aerospace System (NAS). Further development and improvements to the Integrated Safety Assessment Model (ISAM) should fully incorporate UAS operations both for current and future risk analyses. In particular, the flight trajectory of unmanned aerial vehicles (UAVs) can be significantly affected by external disturbances such as turbulence, upstream wake vortices or wind gusts. Also, the aircraft operations are subject to various parametric uncertainties due to the stochastic nature of the atmospheric flows as well as aircraft parameters themselves (Holzäpfel, 2014). In this context, the assessment of the wake vortex interference events in the terminal zone relies on the accuracy of the low-fidelity predictive models incorporating various classes of UAS in the comprehensive wake vortex interference studies.

In recent years, a number of parametric wake vortex prediction models have been developed such as AVOSS wake vortex prediction algorithm (APA) (Delisi, Robins, & Pruis, 2016) and TASS driven algorithms for wake prediction (TDAWP, TDP) (Proctor, Hamilton, & Switzer, 2006) models developed by NASA (Ahmad et al., 2016), and deterministic two-phase model/probabilistic two-phase model (D2P/P2P) (Holzäpfel, 2006) models developed by DLR. These models output the wake vortex's circulation strength and position considering its generation, decay and advection processes. For instance, P2P model is capable of providing a

probabilistic distribution of wake vortex circulation strength and vertical/lateral position in real-time. Considering the wake decay and advection processes, P2P model predicts the uncertainty bounds and the upper and lower limits of wake vortex parameters for the cone of uncertainty in the wake evolution. Alternatively, the Monte-Carlo approach is applied in APA and TDAWP models to get the cones of uncertainty in terms of uncertainty bounds (Ahmad et al., 2014).

The primary motivation of the current study is to develop variable-fidelity approach for addressing the safety of UAS operations in the NAS. This is implemented on the basis of SITAR WVSS (Safety Investigation Toolkit for Analysis and Reporting Wake Vortex Safety System) by developing the dynamic low-fidelity model addressing generation, evolution and interaction of wake vortex with the follower aircraft. Specific objectives of the dissertation research include:

- Wake vortex evolution and prediction of the position and strength of wake vortices in the atmosphere (Out-of-Ground zone, Near-Ground-Zone and In-Ground-Zone) using deterministic and probabilistic approaches. In particular, for the for the In-Ground Zone, the high-fidelity LES simulations are conducted to investigate the propagation of wake vortices in the vicinity of three types of ground surfaces: flat ground, forest canopy and water surface. The obtained results are employed in terms of the reduced order models of In-Ground-Effect, incorporated in the fast-time SITAR WVSS code. Overall, the following extensions are implemented to account for various effects in wake evolution: The Near-Ground Effect (NGE), The In-Ground Effect (IGE)

mode, The effect of ambient stratification and turbulence, Probabilistic modeling of the cone of uncertainty in the wake evolution predictions.

- The wake vortex-aircraft interaction and assessing the operational safety risks. In particular, new a criterion of assessing the wake induced UAS reaction, RCR (Luckner, Höhne, & Fuhrmann, 2004), is incorporated in the model as an impact severity criterion.
- A robust nonlinear control method proven to achieve aircraft trajectory regulation in the presence of unmodeled external disturbances (e.g. wake vortices, wind gusts) and actuator parametric uncertainty. Particularly, this part of the work includes:
 - Implementation of the low fidelity wake vortex/aircraft interaction model
 - Derivation of the nonlinear UAV regulation control method
 - Detailed numerical simulation results which demonstrate the performance of the proposed nonlinear control law
 - Simulation of the same control objective using the H_∞ linear control law for comparison
 - Simulation in the presence of parameter variations as well as SJA mathematical model.
 - The performance of the nonlinear robust controller in the presence of the real wake-vortex disturbance in the vicinity of the ground as well as far from the ground surface (the Monte-Carlo simulations).

2. ADVANCES IN SITAR WVSS LOW FIDELITY MODELING

The task of integrating UAS systems (particularly small-size) with the routine air-traffic operations in the terminal zones poses a number of challenges. One likely scenario examined in the current work is the interaction of a follower UAS (considered in a steady-level flight) with the wake vortex induced by a larger leader aircraft. As the UAS approaches the wake, it is affected by a rolling moment induced by the upstream vortex that may lead to a loss of the aircraft control. The subsequent sections first discuss the models implemented within Safety Investigation Toolkit for Analysis and Reporting Wake Vortex Safety System (SITAR WVSS, or SITAR) module employed in the current study to predict the effects of the UAS wake interaction process. The developed dynamic model of an aircraft entering a wake vortex is presented. It allows evaluating changes in the important flight parameters following the wake vortex interaction and assessing the operational safety risks.

2.1 Safety Assessment Model Implementation

The SITAR WVSS system enables modeling of various scenarios to assess the operational safety risks of UAS by utilizing a list of aircrafts with their characteristics and track files containing information regarding the aircraft's spatial movement as inputs. The input track files contain a set of coordinates in space (altitude, latitude, longitude) and time corresponding to each point. If the points contained in the track files are not sufficient, interpolation can be used to fill every points along the time axis every N seconds, where N is the interpolation

time period. Different interpolation time periods can be set up and the flight can be divided into discrete frames corresponding to the interpolated points. The N-seconds flight through or in the wake can be simulated with a specified response model, which are described in the subsequent sections. This capability allows SITAR's simulations to account for up to ten aircrafts and their wake vortex interaction simultaneously in one scenario. As illustrated in Fig. 2.1, the simulations show the aircraft model with the accompanying trailing wake vortices (in the form of rings) on the interface. Each vortex ring is color coded in green, yellow, or red signifying the level of intensities for three categories of aircraft: Light, Medium, and Heavy according to ICAO wake turbulence category. When the follower aircraft encounters the wake vortex, the impact is calculated using the previously mentioned dynamic model. This also enables the prediction of the follower aircraft's flight trajectory while interacting with the wake vortex. Simulation time can be prescribed and parameters such as maximum bank angle, altitude change, and the angular velocity are calculated. There is an opportunity to create an encounter artificially by supplying the horizontal and vertical offsets and the closing angle.

2.2 Wake Vortex Generation and Evolution Modeling

The wake vortex evolution predictions based on WVSS model (Kazarin et al., 2016) take into account effects of atmospheric turbulence, temperature stratification and wind. The initial modeling of the wake vortex employs



Figure 2.1: Wake vortex rings behind the leader aircraft.

Kutta-Joukowski theorem and specifies the initial elliptical distribution of the bound vortex circulation with amplitude,

$$\Gamma_0 = \frac{W}{\rho V b \frac{\pi}{4}}, \quad (2.1)$$

where b is wing span, W is aircraft weight, ρ is density and V is aircraft velocity.

Usually, the initial vortex core radius may vary between 1% and 5% of the wing span. In accordance with the reported flight test measurements, the initial core radius of the wake appears close to 3.5% of the span. Thus, the following constant radius of the vortex core is assumed in the current analysis,

$$r_c = 0.035b \quad (2.2)$$

Tangential velocities induced by the wake are calculated using Burnham-Hallock model (Burnham & Hallock, 1982) with a constant core radius,

$$V_t = \frac{\Gamma_0}{2\pi} \frac{r}{r_c^2 + r^2} \quad (2.3)$$

The two-phase transport and decay model is used to predict the evolution of the vortex strength incorporating the diffusion phase followed by the rapid decay phase. The model calculates the life time of the vortex ring as proposed by Sarpkaya (Sarpkaya, 2000). The “accumulated damage” model is used for taking into account a possibly varying profile of the eddy dissipation rate (EDR). The lifetime of a vortex T_{dem} is a nonlinear function of EDR, nondimensional time $T = \frac{tV_0}{b_0}$, $C_{\eta 1}, C_{\eta 2}$ are model constants for diffusion and rapid decay phases (Baranov & Belotserkovsky, 2013). The equation which describes the circulation evolution is:

$$\frac{d\Gamma}{dt} = -C_{\eta 1, \eta 2} \frac{\Gamma}{T_{dem}} \quad (2.4)$$

To determine the moment of transition from the diffusion phase to the rapid decay phase, the function $f_{dem}(T)$ is introduced. This function characterizes the portion of the vortex lifetime which is reached by the time point t and is calculated according to:

$$f_{dem}(T) = \int_0^t \frac{dT}{T_{dem} \exp(-0.185N^* T_{dem})} \quad (2.5)$$

where N^* is the nondimensional Brunt-Vaisala frequency. Thus, the effect of stratification on wake vortex decay is taken into account. The rapid decay starts when $f_{dem}(T)$ becomes equal to 1.

Modeling the wake vortices near the ground (as the aircraft takes off or descends for landing) is obtained through the classical inviscid theory (Baranov & Belotserkovsky, 2013). As the vortices approach the “in-ground” vicinity (where the distance to the ground is less than or equal to $2b_0$), a thin vortex sheet (a boundary layer) is generated due to the zero normal velocity at the ground (impermeability condition). With the ground assumed to be flat, the velocity field at any position above the ground is easily obtained by using the image vortices below the ground plane instead of the vortex sheet. Cross-wind influence and vortex decay due to the ambient turbulence are also taken into account in the model.

The ambient stratification effect is also included in the model and is based on the improved analysis (Greene, 1986). It considers the accumulation of the stratification effect in the dynamics of vortices in the atmosphere, and modeled by,

$$\left(\frac{d^2h}{dt^2}\right)_{strat} = - \int_{h_0}^h N^2(h)dh \quad (2.6)$$

where h and h_0 are the current and initial heights of the vortex cores, respectively. Deceleration of the vortex propagation due to the stratification effect is caused by decrease in the vortex circulation and the vortex speed of descent. The effect of

stratification is to reduce the lifespan of vortices and the maximum height attained by them. The stratification-induced deceleration is described by,

$$\frac{dv_{strat}}{dt} = \beta_{str} \alpha_{str}^2 \left(\frac{d^2 h}{dt^2} \right)_{strat} \quad (2.7)$$

with the corresponding circulation reduction defined by,

$$\frac{d\Gamma}{dt} = -(1 - \beta_{str}) \alpha_{str}^2 (2\pi b_0) \left(\frac{d^2 h}{dt^2} \right)_{strat}, \quad (2.8)$$

where all the model coefficients $(\beta_{str}, \alpha_{str})$ are defined (Baranov & Belotserkovsky, 2013).

2.2.1 Deterministic and Probabilistic Approaches

Deterministic simulations are based on the direct application of the model equations described above. However, due to the stochastic nature of the turbulence and significant variations in the vortex position and strength, the deterministic approach to predict wake vortex evaluation is not accurate. Moreover, the state of the atmospheric boundary layer as well as aircraft parameters (Holzäpfel, 2014) cannot be predicted deterministically. The LIDAR measurements from different airports show significant scattering of experimental data and requires implementation of a probabilistic approach that can provide bounds of the expected behavior of wake vortex. The width of the uncertainty bounds depends on variations of parameters the model including parameters and those depending on them (e.g. Γ_0 and b_0).

The "success rate" in probabilistic predictions is defined as the number of experimental points that appear within the bounding curves divided by the total number of experimental points. The additional characteristic introduced for circulation is the fraction of points lying under the upper bound of the circulation curve. Indeed, in most applications, only the maximum value of circulation is important.

In order to quantify the effectiveness of the deterministic and probabilistic approaches, the success rates, root mean square (RMS) deviation, mean absolute error (MAE) and statistical bias values were obtained and compared against results from other existing models.

P2P-based and RMS-based Approaches

This approach is based on DLR's probabilistic two-phase model (Holzäpfel, 2006). P2P is a parametric transport and decay model designed to predict the probabilistic behavior of the wake vortex in real time. The output of the model consists of upper and lower bounds for vortex strength and position. The bounds are obtained from two runs with a combination of decay parameters as well as uncertainty allowances added/subtracted to the curves of wake evolution and propagation.

In the current model, the deterministic curves for the wake evolution are first obtained from the original WVSS model, but the uncertainty bounds are calculated using the P2P approach. Thus, the onset of rapid decay is shifted by $\pm 0.2T_{dem}$, and the vortex strength evolution curve is spread by $\pm 0.2\Gamma_0$. The upper and lower

curves for vertical vortex position are obtained by adding/subtracting of one initial vortex spacing. Also, the influence of ambient turbulence is taken into account. The expression for upper/lower bounds can be written as (Holzäpfel, 2006),

$$z_{u(l)}^* = z^* \pm (1 + \int q^* dt^*) \quad (2.9)$$

where z^* is the vertical coordinate nondimensionalized by b_0 , and RMS value of ambient turbulence (q^*) plays the role of the superimposed propagation velocity.

A very simple approach developed in this work is based on RMS deviations calculated from Denver'03 and Memphis'95 data sets. The normalized values of RMS deviations for the strength and vertical position of wake vortices are first calculated using WVSS model. Next, such values are considered as constant uncertainty allowances. The values of $0.3\Gamma_0$ and $0.5b_0$ are obtained and used in the simulation. The uncertainty allowances are subtracted/added to form lower/upper bound curves of circulation evolution and propagation. The simulation results will be discussed in the next section.

Monte-Carlo Approach

The Monte-Carlo (M-C) approach was evaluated using Memphis'95 and Denver'03 wake vortex data sets. In this section, case 1167 from Memphis' 95 data set was used as an example to illustrate the employed methodology. Note that the validity of the approach using the same data sets in NASA's APA and TDP wake vortex models was also demonstrated (Gloude-mans et al., 2016).

The Monte-Carlo approach is based on perturbing the initial wake vortex conditions (b_0, V_0, z_0) in the deterministic model and generating profiles of the ambient parameters (such as the EDR and potential temperature profiles) using the probability density functions (PDFs). The PDFs are obtained by applying the maximum likelihood estimation method to density histograms corresponding to a particular data set. The vertical profiles are truncated at the heights of the vortex generation and the mean values are calculated from the zero height to that value. 400 perturbations for vertical profiles were generated using PDFs and used as input parameters along with other parametric perturbations. The mean curve and standard deviations were then calculated to obtain the confidence bounds. Figures 2.2 and 2.3 illustrate EDR and potential temperature gradient profiles from Memphis'95 data set, along with density histograms and distributions.

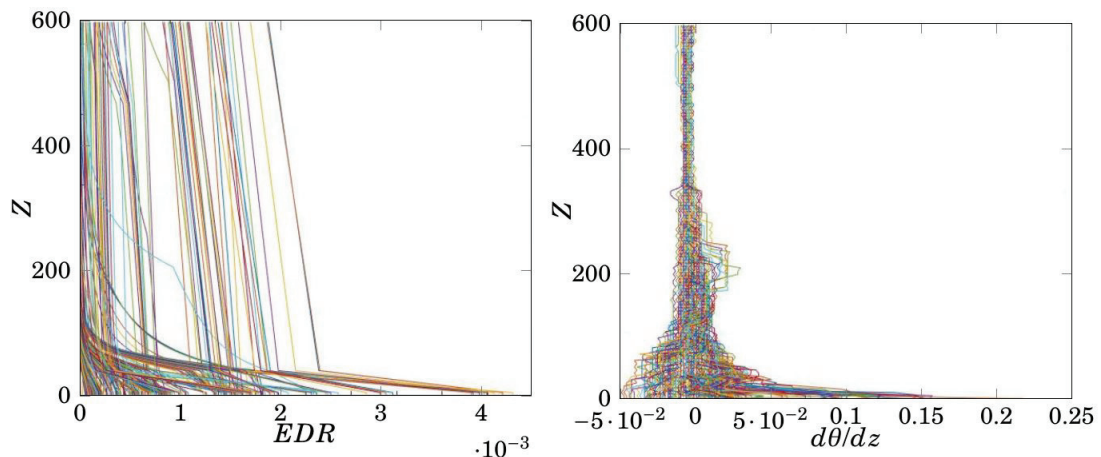


Figure 2.2: Vertical profiles of EDR and potential temperature gradient.

The initial conditions for the stratification profile are provided in terms of the potential temperature distribution. The PDFs are generated for the potential

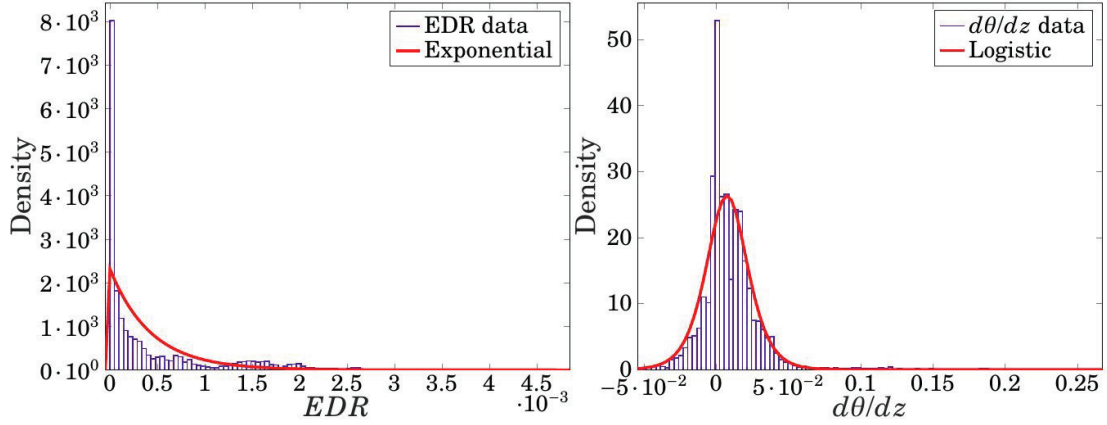


Figure 2.3: EDR and potential temperature gradient histograms.

temperature gradient since this gradient defines the Brunt-Vaisala frequency (2.10) that directly affects the wake decay,

$$N = \sqrt{\frac{d\theta}{dz} \frac{g}{\theta}} \quad (2.10)$$

The perturbations of initial conditions for Γ_0, b_0, z_0, V_0 were calculated according to (Holzäpfel, 2014). For instance, z_0 values with the mean equal to initial z_0 and standard deviation of $7m$ were calculated using normal distribution. For Γ_0 , the variation between $0.9\Gamma_0$ and $1.25\Gamma_0$ was used. V_0 was found from Γ_0 and b_0 . Moreover, a uniform distribution in the range of $0.95b_0$ to b_0 was used to prescribe the initial vortex separation b_0 .

The generated constant profiles of EDR and potential temperature along with other generated initial conditions were used to run 400 Monte-Carlo simulations. The PDFs and generated constant vertical profiles are demonstrated in (Kazarin

& Golubev, 2017a) The potential temperatures were calculated based on $d\theta/dz$, as follows:

$$\theta = \theta_0 + \frac{d\theta}{dz}z \quad (2.11)$$

where θ_0 is the base potential temperature.

The upper and lower bounds are obtained by adding and subtracting the standard deviation to evolution/propagation curve for each time moment. The results for the case 1167 are shown in the next section for all the approaches considered.

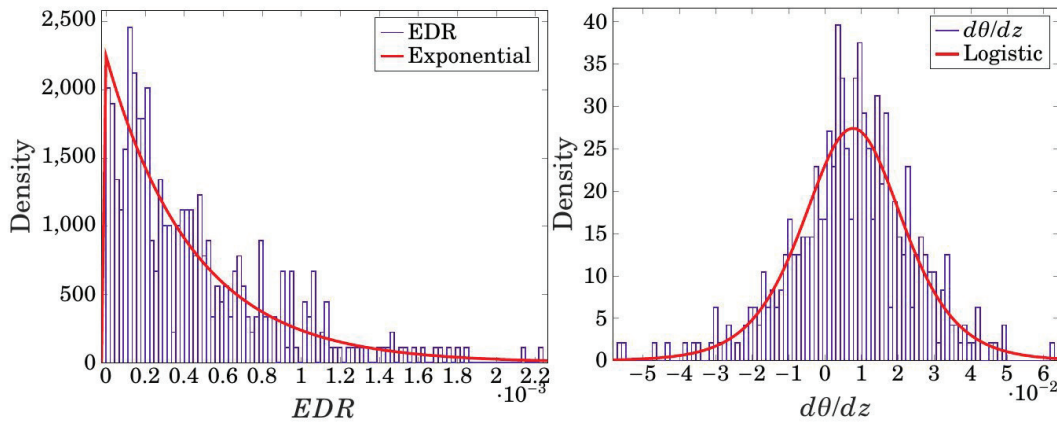


Figure 2.4: PDFs of generated constant vertical profiles.

2.2.2 Results and Comparison with Other Models

In this section, the evaluation of the employed deterministic and probabilistic approaches and their comparison with other models is conducted using Memphis'95 and Denver'03 data sets. A comprehensive field experiment to measure wake vortices and the associated ambient meteorological conditions was conducted at the Memphis International Airport in Tennessee from August 6 through

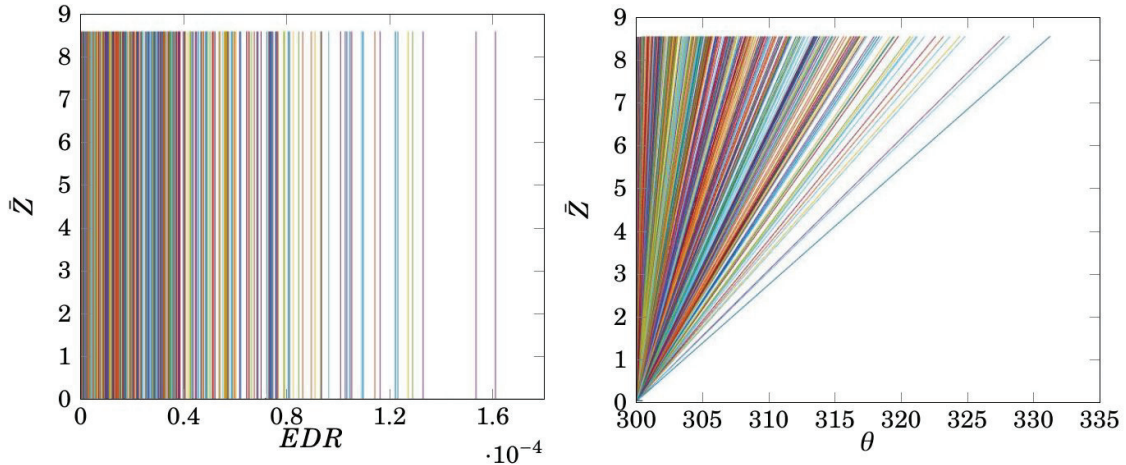


Figure 2.5: Generated constant profiles.

August 29, 1995 (Zak, 1996). The wake data was collected using LIDAR. Also, the meteorological sensors included radiosondes, sodars, a wind profiler, one 150ft high meteorological tower, a Radio Acoustic Sounding System (RASS), and NASA Langley OV-10 research aircraft. The radiosondes were used to measure winds and temperature measurements. The data processed for fast-time wake models included EDR, stratification profiles, and headwind/crosswind data. Also, the aircraft data included the initial position (offset) of the vortex pair with respect to the runway centerline (y_0), the initial height of the vortices (z_0), the initial vortex descent rate (V_0), and the initial vortex separation distance (b_0).

Denver'03 data set was obtained during the experiment conducted by NASA during late August and September of 2003. All the necessary data for the fast-time wake modeling was also provided. Further details about both data sets can be found in NASA report (Ahmad & Pruis, 2015).

Deterministic Approach

The vortex evolution characteristics based on WVSS simulations are demonstrated in Fig. 2.6 for case 1167 from Memphis'95 data set. The LIDAR measurements are also shown (in square symbols) in these plots.

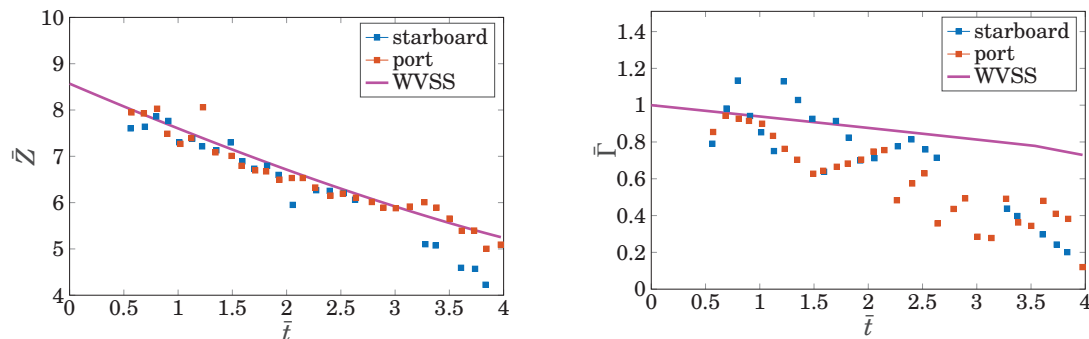


Figure 2.6: Deterministic wake vortex evolution simulations for case 1167.

Clearly, the experimental data scatter for the vortex circulation (Figure 2.6) is very significant, and thus the deterministic predictions appear not adequate. On the other hand, the experimental data is better predicted for the vortex descent (Figure 2.6). However, the deviations for some points are still significant and further increase with the distance.

The accuracy of deterministic approach was estimated in terms of RMS deviation, MAE and statistical bias. The corresponding comparison with results from APA 3.8 and TDP 2.1 models (Delisi et al., 2016) (Proctor et al., 2006) is shown in Tables 2.1 for Denver'03 data.

Probabilistic Approach

Figure 2.8 shows results of the Monte-Carlo simulations for the case 1167 (Memphis'95 data set) with the initial conditions described in section (2.2.1).

Table 2.1: RMS, MAE, BIAS for Denver' 03 data set (OGE)

Parameter (norm by Γ_0, b_0)	WVSS	APA3.8	TDP2.1
RMS_Γ	0.23	0.24	0.3
MAE_Γ	0.19	0.22	0.29
$BIAS_\Gamma$	-0.13	0.2	0.24
RMS_Z	0.66	0.66	0.66
MAE_Z	0.46	0.56	0.55
$BIAS_Z$	0.14	0.074	-0.054

Table 2.2: RMS, MAE, BIAS (Memphis' 95 data set)

Parameter (norm by Γ_0, b_0)	WVSS	APA3.8	TDP2.1
RMS_Γ	0.36	0.29	0.29
MAE_Γ	0.23	0.25	0.24
$BIAS_\Gamma$	-0.08	-0.09	0
RMS_Z	0.5	0.34	0.34
MAE_Z	0.38	0.39	0.29
$BIAS_Z$	-0.12	-0.015	0.09

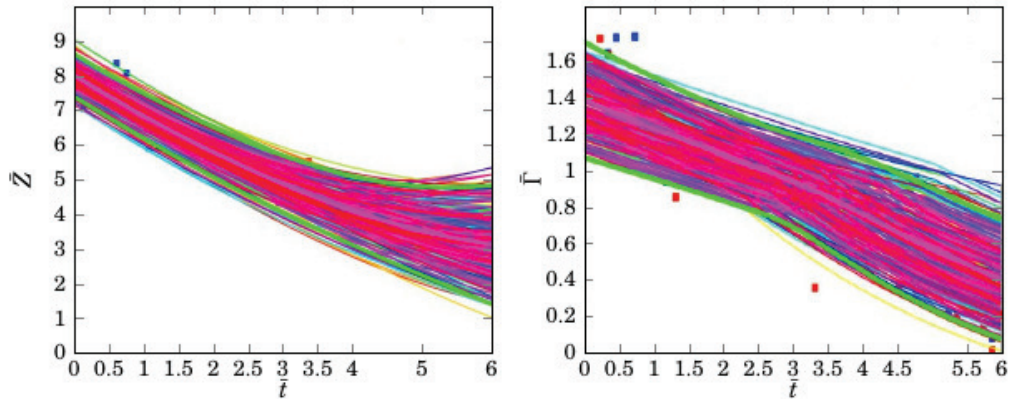


Figure 2.7: Ultra Stick 120. Source: UAV Laboratories, University of Minnesota.

The corresponding RMS-based wake vortex evolution uncertainty bounds are shown in Fig. 2.9 and demonstrate a good success rate in covering experimental data within the predicted cone of uncertainty. Alternatively, the P2P-based results are shown in in Fig. 2.10. In the latter approach, the time of demise also varied, which resulted in a faster divergence of the predicted uncertainty bounds.

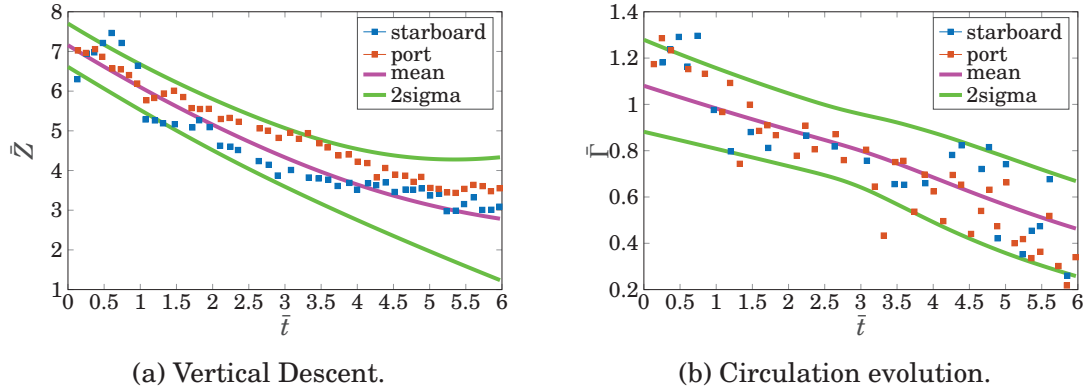


Figure 2.8: Wake vortex evolution 2σ bounds based on 400 M-C simulations.

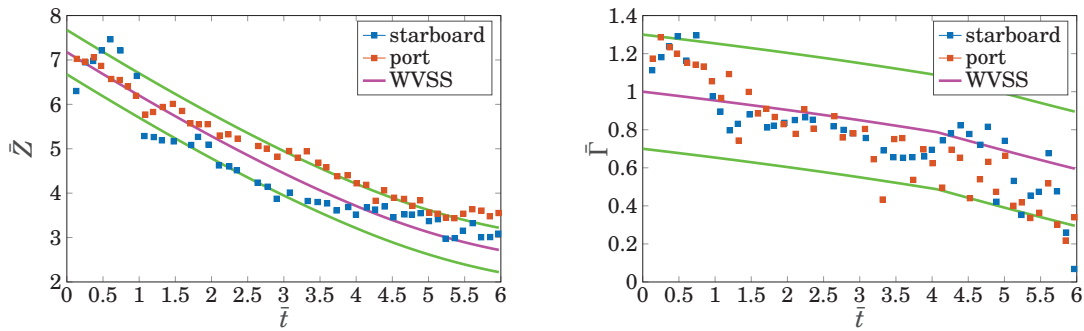


Figure 2.9: RMS-based wake vortex evolution bounds.

From Figures 2.8, 2.9 and 2.10 one may conclude that the uncertainty bounds in P2P-based approach are wide enough to capture nearly all experimental points except the circulation strength during the initial period. Similar behavior appears typical in most case analyses. Also notable is that Monte-Carlo approach appears more accurate in terms of vertical position bounds than RMS-based approach, which is also demonstrated in the success rate statistics discussed below.

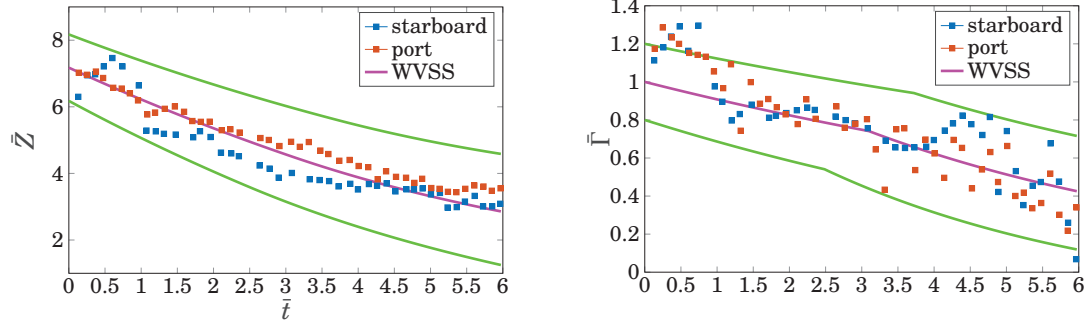


Figure 2.10: P2P-based wake vortex evolution bounds.

The success rates based on all case studies for Memphis'95 and Denver'03 data sets are summarized. The results for Denver'03 is shown in tables 2.4, 2.3 (Full results can be found in (Kazarin & Golubev, 2017a)). In these simulations, the value of Γ_0 was varied from $0.9\Gamma_0$ to $1.25\Gamma_0$, as suggested by (Holzäpfel, 2014) to account for uncertainty, e.g., in aircraft weight. The Monte-Carlo approach implemented in WVSS code demonstrates good results for the vertical position and $\Gamma_{under\ max}$ metrics of the wake vortex evolution and compares favorably against results from APA and TDP models (Ahmad et al., 2014). The overall success rate for circulation based on the current Monte-Carlo simulations appears close to the APA-TDP multimodel result (for Memphis' 95 data set) and multi-model (APA, TDP and D2P) result (for Denver' 03 data set).

At the same time, P2P and RMS based approaches demonstrate a significantly better performance in terms of the success rates. This is attributed to the wider uncertainty bounds obtained in those simulations. Furthermore, such approaches can be easily applied in any fast-time prediction model, require minimum input data and are numerically more efficient compared to Monte-Carlo approach.

Finally, one should note that all the reported probabilistic simulations were conducted only for OGE zone analysis (currently implemented in WVSS code), with the future work extending the studies to IGE zone predictions.

Table 2.3: Success rates (Memphis' 95 data set) (Γ_0 0.9-1.25)

Parameter	$WVSS_{MC,OGE}$	$APA3.8_{MC}$	TDP_{MC}	$APATDP_{MC}$	$WVSS_{P2P}$	$WVSS_{RMS}$
$Z_{within\ bounds}$	0.77	0.68	0.63	0.72	0.96	0.6
$\Gamma_{within\ bounds}$	0.61	0.51	0.25	0.65	0.75	0.78
$\Gamma_{under\ max}$	0.84	0.7	0.59	0.81	0.82	0.91

Table 2.4: Success rates (Denver' 03 data set) (Γ_0 0.9-1.25)

Parameter	$WVSS_{MC}$	$APA3.4_{MC}$	TDP_{MC}	$MultiModel_{MC}$	$WVSS_{P2P}$	$WVSS_{RMS}$
$Z_{within\ bounds}$	0.69	0.68	0.74	0.74	0.88	0.55
$\Gamma_{within\ bounds}$	0.5	0.48	0.35	0.58	0.71	0.84
$\Gamma_{under\ max}$	0.97	0.95	0.94	0.98	0.97	0.98

2.3 Dynamic Model of Aircraft Entering a Wake Vortex

The developed approach incorporates a simplified aircraft dynamic model to evaluate the effects of the wake vortex interaction. In this model, only the banking moment perturbation is considered while the side forces resulting from the wake interaction are not taken into consideration (note that the magnitude of the induced rolling moment may thus be slightly overestimated since accounting for the lateral motion would reduce the wake interaction period). In addition, pitching and yaw moments are also neglected. Additional parameters include sideslip, which is assumed to be zero, thrust force, which counteracts the drag, and G-force equal to

1 for a steady horizontal flight. Based on the described assumptions, the dynamics of the aircraft can be described by (McCormick, 1995):

$$\frac{dV}{dt} = -\sin(\Theta) \quad (2.12)$$

$$\frac{d\Theta}{dt} = \frac{g}{V}(\cos\gamma(1 + \Delta p) - \cos(\Theta)) \quad (2.13)$$

$$\frac{d\Psi}{dt} = \frac{g}{V\cos\Theta}(\sin\gamma(1 + \Delta p)) \quad (2.14)$$

Correspondingly, the dynamics of the aircraft position in spatial coordinates is governed by,

$$\frac{dh}{dt} = V\sin(\Theta) \quad (2.15)$$

$$\frac{dx}{dt} = V\cos(\Theta)\cos(\Psi) \quad (2.16)$$

$$\frac{dz}{dt} = -V\cos(\Theta)\sin(\Psi) \quad (2.17)$$

Furthermore, the induced rolling moment, ΔM_x , and the control input, M_{ux} , are introduced in the following linearized equations governing the roll angular velocity ω_x and the bank angle γ ,

$$\frac{d\omega_x}{dt} = \frac{\frac{\rho V S l^2}{2} m_x^{\omega_x} + \Delta M_x - M_{ux}}{I_{xx}} \quad (2.18)$$

It is worth noting that the induced rolling moment and the control input are introduced in the linearized equations governing the roll angular velocity and the bank angle. The aerodynamic forces, moments, and the magnitude of induced rolling moment depend on such factors as the wake intensity and the aircraft geometry and can be obtained using the strip model described, e.g., in (McCormick, 1995), where the induced rolling moment is the resultant of the sum of moments created by particular "strip" of wing and fins.

2.4 Wake Vortex Encounter Predictions

The parametric study with several variable-size UAS systems interacting with the wake generated by a leader Boeing 737 aircraft for two different cases is considered within the deterministic approach. Also, the probabilistic approach is developed. The obtained probabilistic predictions based on the improved (SITAR) WVSS model (Kazarin et al., 2016) are validated against Memphis'95 and Denver'03 airport LIDAR data (Gloude-mans et al., 2016). Three probabilistic approaches are applied (including P2P-based approach, Monte-Carlo simulations and RMS-based approach) to compare the resulting boundaries of the cones

of uncertainty for the wake vortex strength position. The performance of all approaches is estimated in terms of the "success rates" in comparison with scattered experimental data. Finally, a comparison of current predictions against results based on APA 3.8 and TDP 2.1 models is conducted.

2.5 Benchmark Case Study Scenario for Wake Induced UAS Reaction and Response

The first case corresponds to an encounter at an altitude of 860 m and $V_L = 86$ m/s. In the second case, the encounter occurs after the take-off of a Boeing 737. The UAS selected as follower aircraft are the Osprey small UAV (sUAV), MQ-1 Predator UAV, and Northrop Grumman's RQ-4 Global Hawk UAV. Their key characteristics are presented in Table 2.5.

Table 2.5: UAV characteristics parameters used in simulations

UAV	Weight (kg)	J_{xx} (kg * m ²)	Wing span (m)	Wing area (m ²)
Osprey	29.48	5.17	3.35	1.87
MQ-1 Predator	1020	3547	14.8	11.5
RQ-4 Global Hawk	12133	241660	35.42	50.1

To assess the wake induced UAS reaction, a roll control ratio is used as the impact severity criteria (Schwarz et al, 2010),

$$RCR = |C_{l,WV}/C_l(\delta_{a,max})| \quad (2.19)$$

The values of RCR behind the B-737 for the three UAS are illustrated in Fig. 3. Zones with $RCR > 1$ are considered hazardous due to the induced rolling disturbance exceeding the aircraft's maximum roll control power, thus resulting in a loss of control. Results for the Osprey sUAV reveals the impact with a wake from B-737 to be hazardous at the horizontal offset of 15 m from the leaders' flightpath. These regions are spaced approximately 30 meters from one another and show an area in between inducing zero rolling disturbance on the sUAV. Therefore, a stable flight is possible for an Osprey operating behind a B-737 due to its small size and short wingspan, however it would have to operate in the areas with $RCR = 0$. Results for the Global Hawk and Predator UAVs (Fig. 2.11) reveal the zones of the wake vortex impact to be much greater. Such differences are primarily a result of the larger aircraft dimension and wingspan.

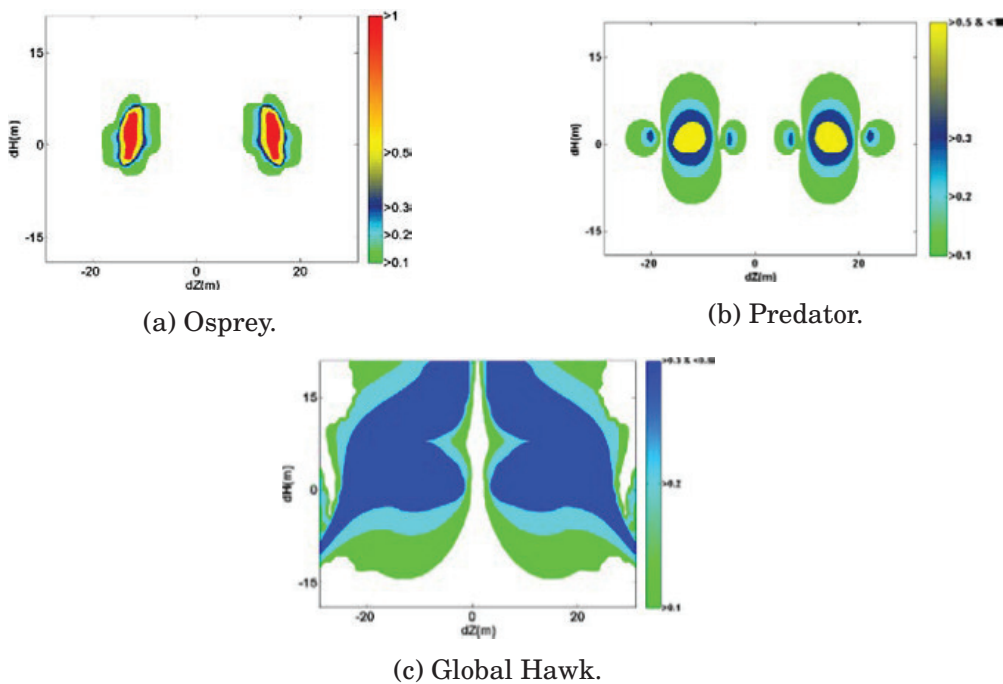


Figure 2.11: Wake vortex induced Roll Control Ratio (RCR) contours.

The aircraft response model incorporated in the SITAR code assumes an immediate reaction of the aircraft to the wake-induced disturbance in the form of the maximum aileron deflection to compensate for the exerted rolling moment. The control input is used to simulate the autopilot response using one of three models:

- The first model realizes the maximum aileron deflection at time $T_1 = 0.5$ s after the entry. The moment of entry is $T = 0$
- In the second model, the ailerons are fully deflected (30 deg) after the delay of $T_2 = 0.1$ s if the bank angle exceeds the maximum of 10 deg or if the bank angular velocity exceeds the limit of 15 deg/s
- In the third model, there is no response input

Fig. 2.12 compares the bank deviations with the corresponding response models when entering a wake vortex for different UAS where blue curve shows the case without reaction, green one - full deflection after T_1 , red one - full deflection after T_2 . The altitude change of the follower UAV for both benchmark cases was also analyzed. The data for RCR and bank angle was obtained based on deterministic SITAR WVSS model. However, it can be adapted for the probabilistic realization of WVSS model.

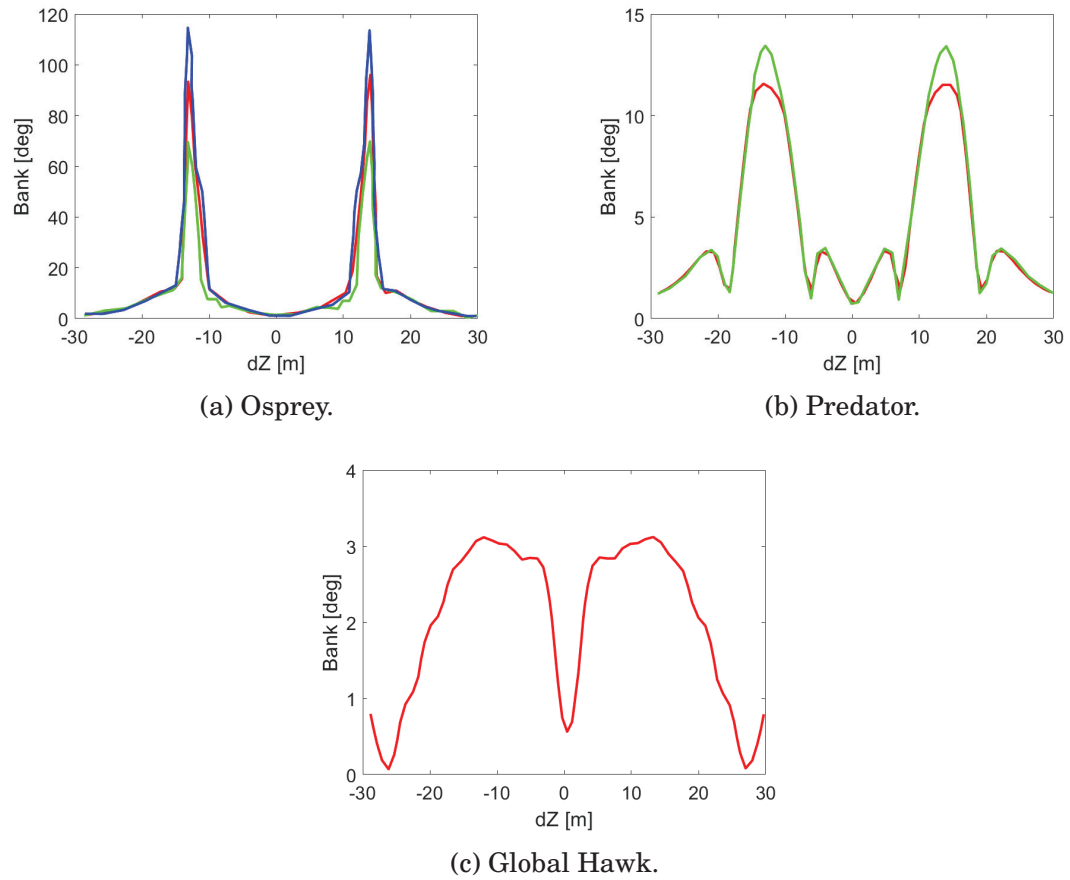


Figure 2.12: Maximum bank deviations for Osprey , Predator and Global Hawk.

3. HIGH FIDELITY MODELING: EFFECTS OF GROUND SURFACE CONDITIONS ON AIRCRAFT WAKE VORTEX EVOLUTION

The chapter investigates and compares decay and transport of an aircraft wake vortex in the vicinity of a solid surface, a forest canopy, and a water surface, representative of various terminal-zone environments. The analysis elucidates some critical features and differences in near-ground wake dynamics which could be important for aircraft operations during takeoff and landing. Particularly, the results of the study may provide insights for ensuring wake safety in future integration of various classes of unmanned aircraft systems (UAS) in airport operations. The reported results are based on Large Eddy Simulations (LES) conducted using an open-source OpenFOAM solver. The obtained high-fidelity findings will form the basis for reduced-order models to be integrated in the fast-analysis code under development for in-situ wake vortex evolution predictions.

It is well known that wake vortices emitted by the leader aircraft persist for a long period of time and pose a potentially significant risk to the follower aircraft by inducing severe unsteady aerodynamic loads, particularly critical at takeoff and landing in close proximity to the ground. A number of aircraft accidents were reported in the past involving, e.g., small general aircraft affected by a mispredicted dynamics of a wake emitted by a large leader aircraft (Schwarz & Fischenberg, 2014). On the other hand, the near-ground wake-vortex evolution and decay vary significantly depending on various types of surface conditions present at the

terminal zones. Hence, this subject must be addressed through a high-fidelity modeling such as proposed in the current work.

The probability of wake encounters increases significantly during final approach in ground proximity. Moreover, close to the ground the wake can suddenly change its dynamics due to rebounding and other complex nonlinear features associated with production of secondary vorticity (in-ground effects). The mechanisms of wake vortex propagation near the ground (including both out-of-ground effects (OGE) and in-ground effects (IGE)) have been studied extensively in the past (Proctor, Hamilton, & Han, 2000; Robins & Delisi, 1993; Barker & Crow, 1977; Holzapfel & Steen, 2007). A number of LES studies as well as experimental data were used to investigate various phenomena associate with behavior of wake-vortex pair near the ground surface. For instance, (Wang et al., 2016) studied the effect of solid obstacle on wake vortex decay and propagation. Much less research examined the effect of different types of ground surfaces on the wake propagation. The LES TASS code was employed (Proctor & Han, 1999) to consider the effect of surface roughness. The influence of surface roughness and its patterns on wake vortex propagation was studied (Zheng & Wei, 2013). Vortex ring interaction with water surface was studied experimentally (Weigand & Gharib, 1995). (Sarpkaya, 1996) extensively researched the vortex-ring/free-surface interaction experimentally and pointed out to the need of more thorough numerical investigations. The vorticity interaction with free surface to give a thorough interpretation of the associated physical phenomen was studied (Rood, 1995, 1994).

Additional insights are to be gained from experimental studies of the near-surface flow dynamics over air-water and air-solid interfaces conducted (Shaikh & Siddiqui, 2010). Furthermore, in (Lim & Adhikari, 2015) a thorough review on the interaction of vortex ring with porous surfaces. A numerical study of a vortex ring impact with a permeable wall was conducted (Cheng, Lou, & Lim, 2014).

The canopy characterization including its interaction with atmospheric boundary layer was examined in a number of previous studies. For instance, the wind interaction with the forest canopy, the resulting drag effects, as well as the experimental studies of the aerodynamic properties of trees and plants were conducted (Bitog et al., 2012; Raupach, Finnigan, & Brunet, 1996; Mueller, Mell, & Simeoni, 2014; Aumond et al., 2013). The properties of the atmospheric boundary layer over the forest canopy and a complex terrain were also thoroughly investigated (Belcher, Finnigan, & Harman, 2008; Schindler, 2004; Crasto, 2007; Gavrilov et al., 2011). The flow interactions with various canopies, their induced turbulence properties (Ghisalberti & Nepf, 2009; Suga & Kuwata, 2014), and the characteristics of the wind flow above and within the forest (Marshall, 1998; Shaw & Schumann, 1992) were addressed. Finally, the properties and distribution of different types of forests, along with the evaluation of the forest crown profiles, were studied (Dubrasich, Hann, & Tappeiner I, 1997; Fayad et al., 2016).

3.1 Numerical Formulation

3.1.1 Numerical Method

All current simulations were performed using OpenFOAM CFD software, with Swak4FOAM library employed for initialization of the wake vortex flowfield. The OpenFOAM solver employs a finite-volume approach with second-order discretization in time and space. An implicit-backward time marching scheme with central-difference spatial discretization were selected. The transient solver for incompressible, turbulent flow based on PIMPLE (merged PISO-SIMPLE) algorithm was used. In addition, for multiphase simulations, a solver based on volume-of-fluid (VOF) phase-fraction, interface-capturing algorithm was utilized. Such method is shown to be more flexible and efficient than other methods for treating complex boundary conditions with free-surface interfaces (Hirt & Nichols, 1981).

Porous medium features are modeled by adding a source term and a porosity coefficient in the time derivative (Hafsteinsson, 2009) of Navier-Stokes equations,

$$\frac{\partial}{\partial t}(\gamma \rho u_i) + u_j \frac{\partial}{\partial x_j}(\rho u_i) = -\frac{\partial p}{\partial x_j} + \mu \frac{\partial \tau_{ij}}{\partial x_j} + S_i, \quad (3.1)$$

where γ is between 0 and 1 (1 corresponds to complete porosity), and S_i is a source term consisting of two parts: the inertial term (proportional to the velocity squared) and the viscous loss term (proportional to the velocity) contributing to the pressure

drop with the generally nonlinear dependence on the fluid velocity. The employed Darcy-Forchheimer source equation is defined as follows,

$$S_i = -(\mu D_{ij} + \frac{1}{2}\rho|u_{jj}|F_{ij})u_i, \quad (3.2)$$

where in the case of a simple homogeneous porous medium, the tensors D_{ij} and F_{ij} are replaced with scalars D and F representing viscous and inertial resistance coefficients.

LES simulations were conducted using implicit LES (ILES) approach. Parallel computations were implemented using the "scotch" domain decomposition method minimizing the number of subdomain boundaries and requiring no geometric input from a user.

3.1.2 Wake Vortex Pair Initialization

Burnham-Hallock's model was chosen for initialization of a fully rolled-up pair of wake vortices, with the vortex core radius of $r_c = 3m$ (Burnham & Hallock, 1982). The initial position above a ground surface was set at $b_0/2$. The wake parameters were selected in accordance with the experimental data ("Meteorological and Wake Vortex Data Set, Dallas-Fort Worth International Airport", 1998) and shown in Table 3.2. Simulations were performed with Reynolds number $Re_\Gamma = \Gamma_0/\nu = 23000$ (conventionally much smaller compared to more realistic $Re_\Gamma \sim 10^7$). The molecular viscosity and density values of $\nu = 1.7 \cdot 10^{-2}m^2/s$ and $\rho = 1.2kg/m^3$ for air, and $\nu = 1.13 \cdot 10^{-3}m^2/s$ and $\rho = 1000kg/m^3$ for water were selected, respectively. The

wall-resolved LES required a stretched mesh in the wall-normal direction, with $y+$ value not exceeding 1. For the following discussion, the non-dimensional time is defined as $\bar{t} = t/t_0$ where $t_0 = \Gamma_0/2\pi b_0^2 = 22$ s.

Table 3.1: Initial vortex parameters

Parameter	Value
b_0	37 [m]
Γ_0	390 [m^2/s]
Initial height	16 [m]

For the canopy study, general initial parameters were chosen. The initial position above a ground surface as well as separation was set at b_0 . The wake parameters correspond to those for a generic heavy aircraft (Gerz, Holzäpfel, & Darracq, 2002). Simulations were performed with Reynolds number $Re_\Gamma = \Gamma_0/\nu = 23100$ (conventionally much smaller compared to more realistic $Re_\Gamma \sim 10^7$). The molecular viscosity and density values of $\nu = 2.29 \cdot 10^{-2} m^2/s$. The wall-resolved LES required a stretched mesh in the wall-normal direction, with maximum $y+$ value not exceeding 0.3. For the following discussion, the non-dimensional time is defined as $\bar{t} = t/t_0$ where $t_0 = \Gamma_0/2\pi b_0^2 = 26.2$ s. The initial vortex parameters are presented in Table 3.2.

Table 3.2: Initial vortex parameters

Parameter	Value
b_0	47.1 [m]
Γ_0	530 [m^2/s]
Initial height	47.1 [m]

3.1.3 List of Simulations

Simulations were conducted for three types of ground surfaces: solid (hard) surface, forest canopy (modeled as porous medium), and water surface. In the case of the forest canopy and the water surface, the employed computational domains were extended by attaching extra regions at the bottom boundaries. The list of simulations and the parameters of the numerical setup are summarized in Table 3.4.

Table 3.3: Simulations and numerical setup parameters

Case	Domain size	Type of the Ground Surface	Attached region height [m]
1	$2.2b_0 \times 8.1b_0 \times 2.2b_0$	flat ground	—
2	$2.2b_0 \times 8.1b_0 \times 2.47b_0$	porous surface	10
3	$2.2b_0 \times 8.1b_0 \times 2.47b_0$	water surface	10

The evolution of the wake vortex pair near different configurations of a forest canopy is also considered. The change in the canopy height, the type of the forest canopy, canopy roughness, as well as the effect of the forest clearing on the wake vortex is investigated. The separate set of simulations describing the wake evolution near the forest configurations described above is presented.

Several configurations of the ground surface are considered in the study: the flat ground (hard surface), the flat tomato canopy, the deciduous forest canopy (hardwoods), rough tomato canopy, and flat tomato canopy with clearing. In all the cases considered except the hard surface case, the computational domain was extended by attaching an extra region at the bottom boundary. The list

of simulations and the parameters of the numerical setup are summarized in Table 3.4.

The difference between the flat and the rough cases is in the values of D and F coefficients and will be further discussed. The difference between the rough and the flat tomato canopy cases is the shape of the attached porous domain. In the former case, the porous domain consists of the $(6 \times 6m)$ columns which models the stems and crowns of the hardwoods (Dubrasich et al., 1997). The heights of such 'trees' are distributed normally with the prescribed standard deviation($\sigma = 3$) to demonstrate the effect of the rough canopy surface (Figure 3.1).

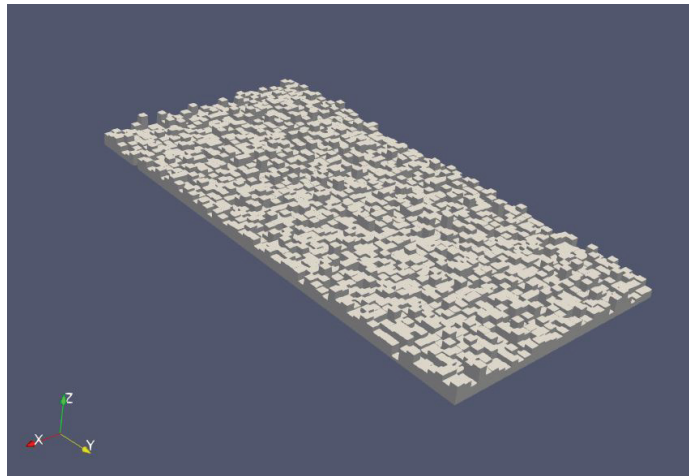


Figure 3.1: The rough porous surface.

Case	Domain size	Type of the Ground Surface	Attached region size
1	$4b_0 \times 8b_0 \times 3b_0$	ground surface	—
2	$4b_0 \times 8b_0 \times 3.3b_0$	tomato canopy	10m
3	$4b_0 \times 8b_0 \times 3.15b_0$	flat hardwoods(deciduous)	5m
4	$4b_0 \times 8b_0 \times 3.3b_0$	rough hardwoods(deciduous)	10m
5	$4b_0 \times 8b_0 \times 3.3b_0$	tomato canopy with clearing	10m

3.1.4 Computational Domains and Boundary Conditions

Two computational domains were considered in the current analysis (Table 3.4). The initial $(2.2b_0 \times 8.1b_0 \times 2.2b_0)$ domain selected for solid ground surface simulations was extended to $(2.2b_0 \times 8.1b_0 \times 2.47b_0)$ domain for modeling the forest canopy and water surface effects. With the initial vortex separation distance of $b_0 = 37 \text{ m}$, the resulting dimensions of the selected domains were $(L_x, L_y, L_z = 82 \text{ m}, 300 \text{ m}, 82 \text{ m})$ and $(L_x, L_y, L_z = 82 \text{ m}, 300 \text{ m}, 92 \text{ m})$, respectively. Based on the grid sensitivity studies, an adequate grid resolution was achieved with $N_x, N_y, N_z = 150, 545, 192$ cells and $N_x, N_y, N_z = 150, 545, 232$ cells, correspondingly. The mesh was stretched in the wall-normal direction up to b_0 and remained uniform up to the domain top boundaries.

Due to the computational constraints, a short domain extension in the vortex core direction was employed. Note that such domain may not fully resolve the three-dimensional linking instabilities. On the other hand, the evolution of the wake vortex in short ($2.2b_0$ in x direction) and long ($12.2b_0$ in x direction) domains were compared (Proctor et al., 2000), with the circulation and lateral position time histories revealing only slight differences.

Periodic boundary conditions were imposed in the lateral and axial directions. The no-slip wall and slip wall boundary conditions were set on the lower and upper bounds for the hard surface case. In the cases of the forest canopy and water surfaces, porous and water regions of 10 m height were attached to the lower

bound of the domain with the wall boundary condition applied at the bottoms of the regions. The porous zone initialization is further discussed in Section 3.2 and 3.2.3.

Also, three computational domains are considered in the canopy analysis (Table 3.4). The initial $(3b_0 \times 8b_0 \times 3b_0)$ domain selected for solid ground surface simulations is extended to $(3b_0 \times 8b_0 \times 3.15b_0)$ and $(3b_0 \times 8b_0 \times 3.3b_0)$ domain for modeling the forest canopy. With the initial vortex separation distance of $b_0 = 47.1 \text{ m}$, the resulting dimensions of the selected domains are $(L_x, L_y, L_z = 192 \text{ m}, 384 \text{ m}, 144 \text{ m})$, $(L_x, L_y, L_z = 192 \text{ m}, 384 \text{ m}, 149 \text{ m})$ and $(L_x, L_y, L_z = 192 \text{ m}, 384 \text{ m}, 154 \text{ m})$ respectively. Based on the grid sensitivity studies, the adequate grid resolution was achieved with $N_x, N_y, N_z = 256, 512, 256$ cells and $N_x, N_y, N_z = 256, 512, 296$ cells, correspondingly. The mesh was stretched in the wall-normal direction up to b_0 and remained uniform up to the domain top boundaries.

Periodic boundary conditions were imposed in the lateral and axial directions. The no-slip wall and the slip wall boundary conditions were set on the lower and upper bounds for the hard surface case. In the cases of the forest canopy, the porous regions of 5 m and 10 m height were attached to the lower bound of the domain with the wall boundary condition applied at the bottoms of the regions.

3.1.5 Grid Sensitivity Study

The grid sensitivity study is conducted for the hard surface case for three grid resolutions. The list of the grids is presented in Table 3.6. The results for the vertical and horizontal evolution of the wake vortex as well as for circulation decay

Table 3.5: Grids employed for grid sensitivity study

Case	Domain resolution [cells]	Total number of cells
coarse	$120 \times 492 \times 159$	9,387,360
medium	$150 \times 545 \times 192$	15,696,000
fine	$167 \times 612 \times 230$	23,506,920

history do not differ significantly (Figures 3.4 and 3.4c). The medium grid with $150 \times 545 \times 192$ cells is used in subsequent analysis.

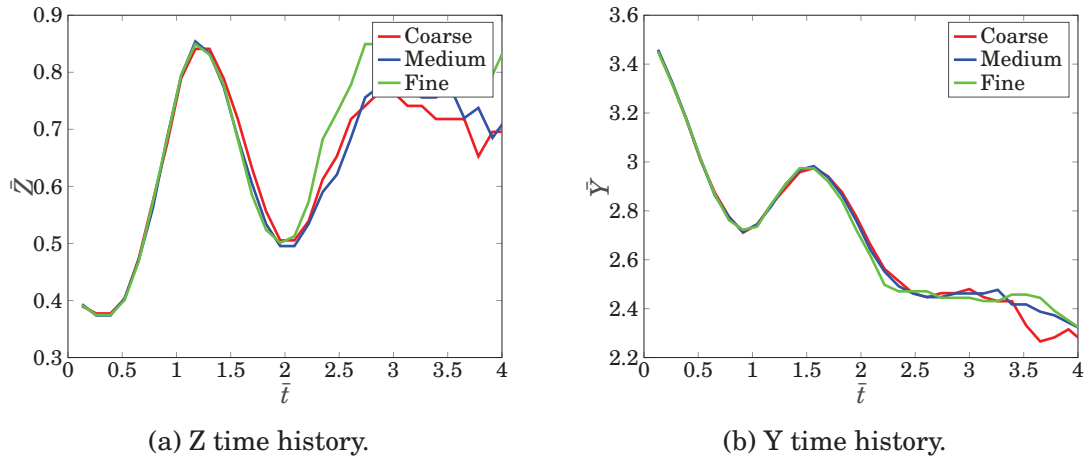


Figure 3.2: Position comparison with light detection and ranging system (LIDAR) data.

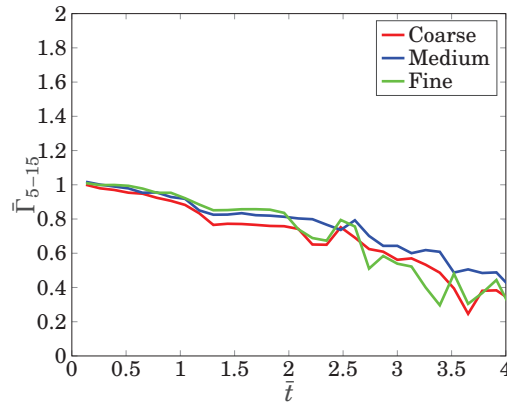


Figure 3.3: Circulation comparison with LIDAR data.

The grid sensitivity for canopy study is also performed and is conducted for the hard surface case for three grid resolutions. The list of the grids is presented in Table 3.6.

Table 3.6: Grids employed for grid sensitivity study

Case	Domain resolution [cells]	Total number of cells
coarse	$213 \times 426 \times 213$	19,327,194
medium	$256 \times 512 \times 256$	33,554,432
fine	$282 \times 563 \times 282$	44,772,012

The results for the vertical and horizontal evolution of the wake vortex as well as for circulation decay history do not differ significantly (Figure 3.4). The medium grid with $256 \times 512 \times 256$ cells is used in subsequent analysis.

3.2 Wake Vortex Evolution with Different Ground Surfaces

The current simulations are conducted for a quiescent medium (i.e., without any ambient turbulence, cross wind or wind shear, or temperature stratification). The obtained results will be used as benchmarks for subsequent studies accounting for various non-quiescent medium effects.

3.2.1 Solid Flat Ground Surface

The Q-isosurfaces describing the evolution of the vortex pair in time are demonstrated in Figure 3.5. The dynamics of the ground approach and rebound is clearly observed along with the induced near-ground vorticity layer as the pair approaches the wall. The vortex roll-up is accompanied by the formation of the secondary vortices that detach from the ground and start circulating around the primary vortices interacting with the latter and eventually distorting those by

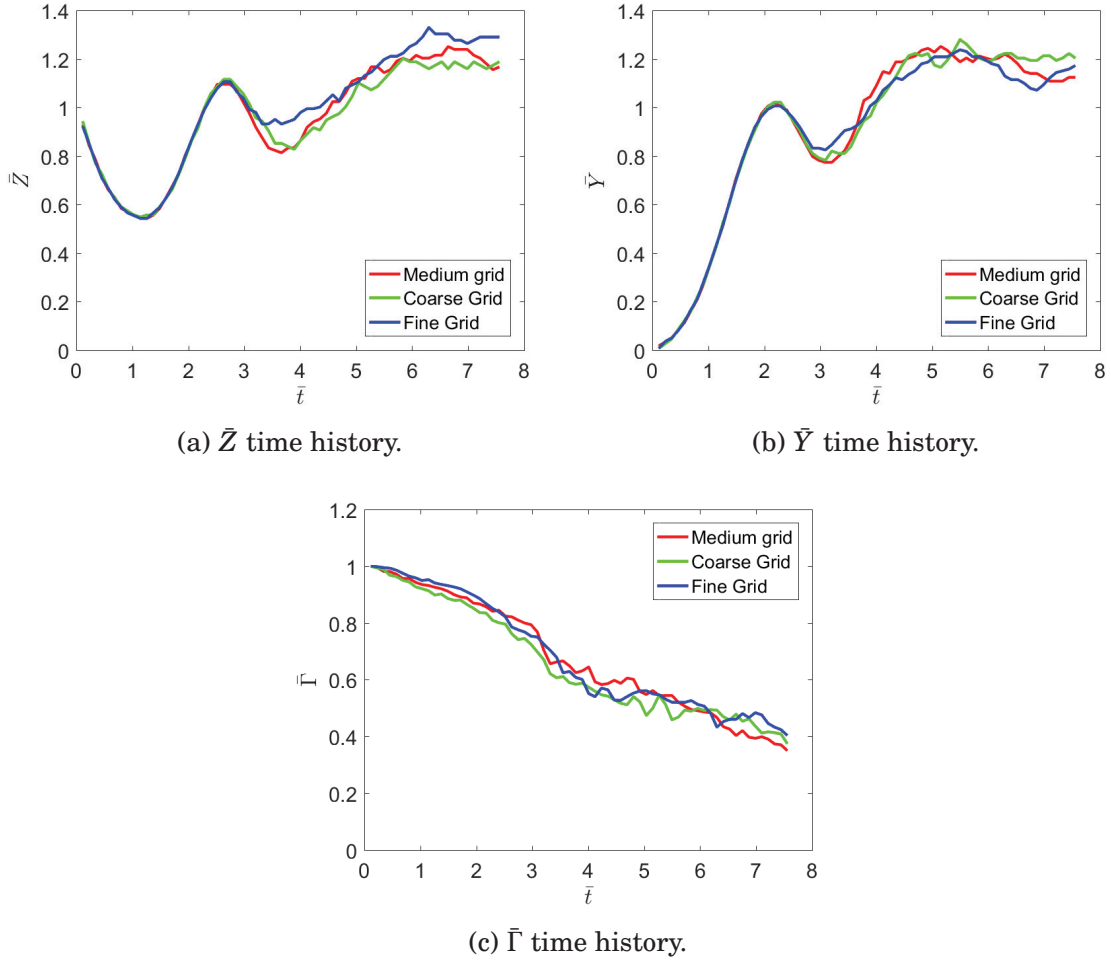


Figure 3.4: Grid sensitivity study.

inducing short-wave instabilities in the appearing complex system of vortical structures (Harris & Williamson, 2012).

The vortex strength is defined using a common measure, $\Gamma_{5-15} = \frac{b}{6} \int_{b/12}^{b/4} \Gamma(r) dr$, where $\Gamma(r)$ is the circulation calculated over a circle of radius r centered at the vortex core, and b is the wing span of the generator airplane. The center of the vortex core was tracked by locating the point with the minimum pressure value.

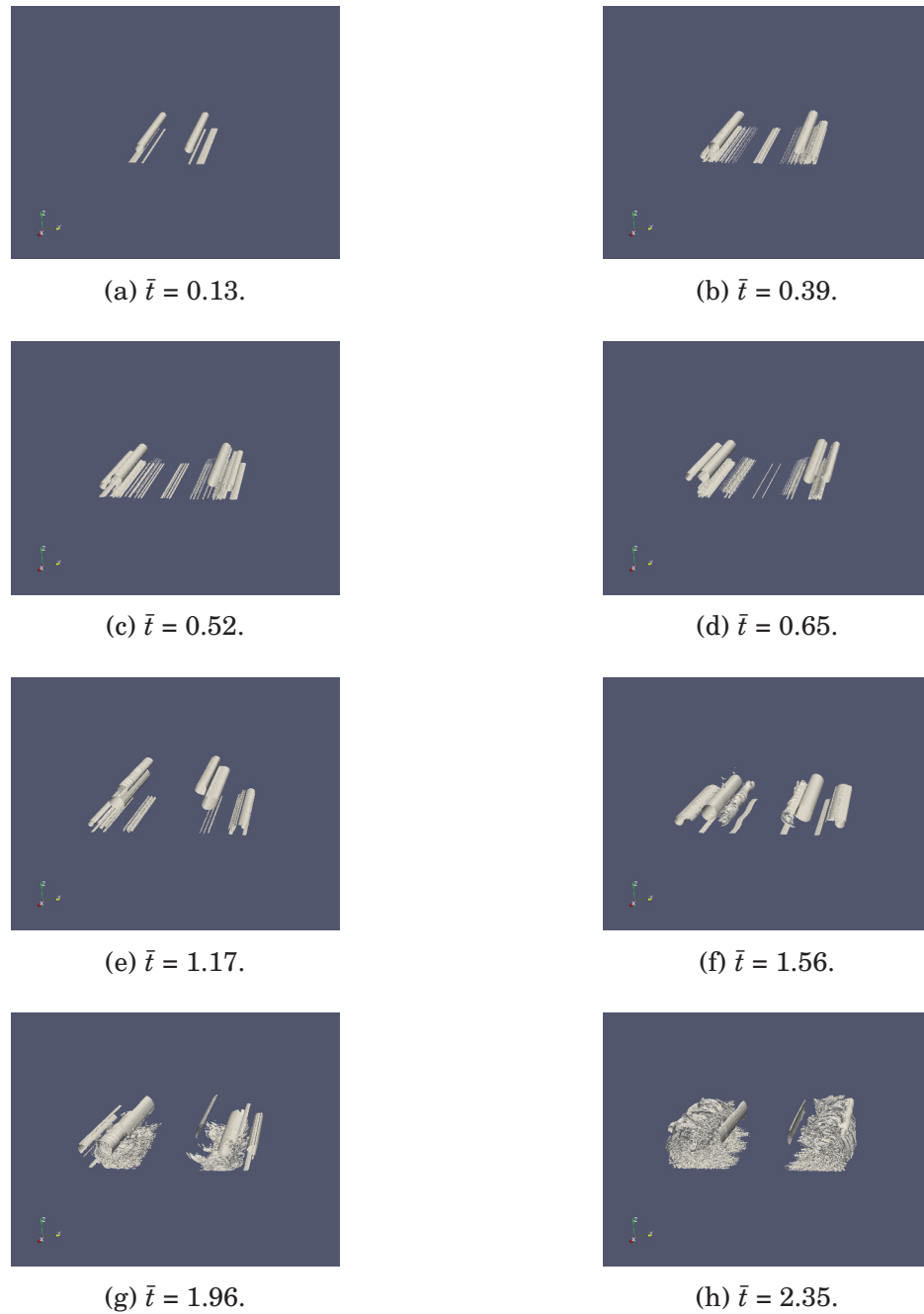


Figure 3.5: Wake vortex evolution with flat ground. Q isosurfaces.

For the test study, LES simulation of the vortex pair dynamics is performed for the landing L-1011 aircraft, with results compared against LIDAR data (“Meteorological and Wake Vortex Data Set, Dallas-Fort Worth International

Airport”, 1998) and LES simulation of (Proctor et al., 2000). Note that several 3D computations were performed in the latter study for different levels turbulence intensity defined in terms of the eddy dissipation rate (EDR). Since no turbulence is included in current simulations, only one case with $EDR = 3.317 \cdot 10^{-8}$ is selected for the current comparison. The LIDAR measurements along with the position and circulation history are shown in (Kazarin & Golubev, 2017b)

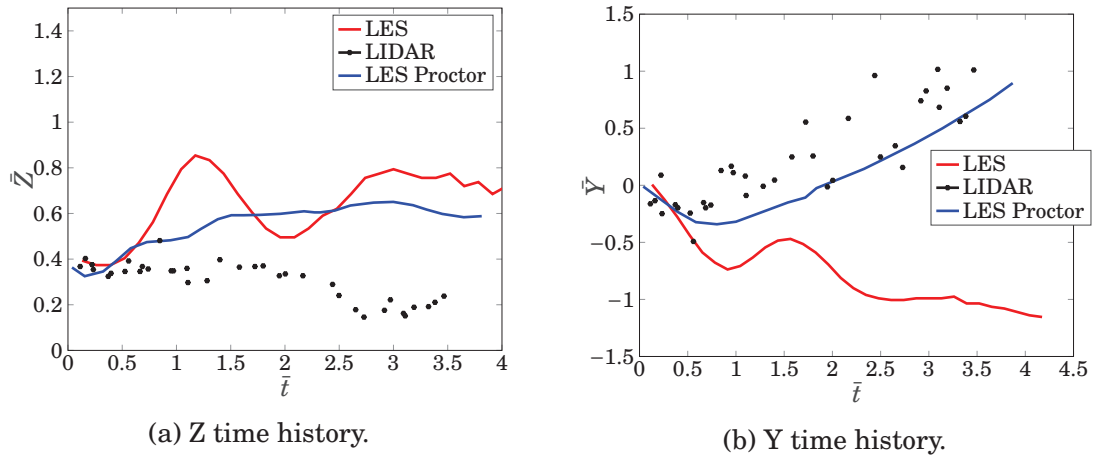


Figure 3.6: Position comparison with LIDAR data.

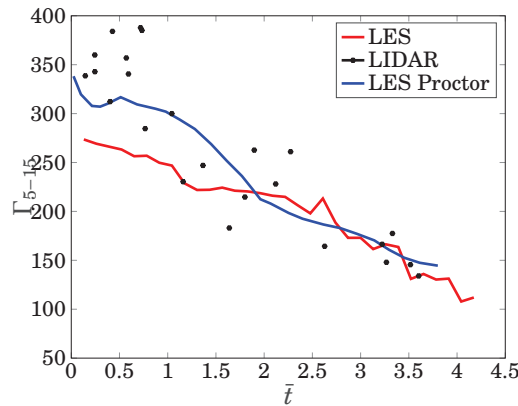


Figure 3.7: Circulation comparison with LIDAR data.

The time history of the vortex vertical position is shown in Figure 3.6a. One may notice that after $\tilde{t} = 0.5$, a strong rebound occurs. Since no ambient turbulence

is introduced in the computations, the vortex pair remains stable (undeformed) for a long period of time, which allows the secondary vortex to rotate around the primary one without significant dissipation and forces the primary vortex to ascend. The resulting strong rebound followed by return to descent causes the oscillatory trajectory pattern observed in Figure 3.6a and may explain deviation from the expected behavior. Further discrepancies between both simulations and measurements may be attributed to several possible causes as mentioned in (Proctor et al., 2000).

The predicted port-vortex lateral position is shown in Figure 3.6b, with the difference between the current simulation and experiment attributed to the unaccounted ambient wind. On the other hand, the predicted vortex strength measure (Figure 3.7) is generally close to results from LIDAR measurements and results (Proctor et al., 2000). The observed difference in the initial circulation values is attributed to the different applied vortex initializations.

3.2.2 Comparison with Experimental Data

In this section, the validation of the solver setup using the experimental data (Stephan et al., 2014) is performed. The simulation domain size, initial and boundary conditions are similar to those used in (Wang et al., 2017). The initial parameters used for vortex pair initialization replicate the ones from the experiment (Table 3.7). For comparison, the LES simulations are performed for two grid sizes: 18.6 million cells and 32 million cells. Figure 3.8 demonstrates the circulation and vertical position time histories of the wake vortex. From

Figure 3.8a, one can see that the initial rebound height based on LES simulation is higher than the experimental one. As mentioned in (Wang et al., 2017), the effect could be due to the lack of the background turbulence and/or the difference in the initial conditions in the simulation and the experimental setup. The circulation values (Figure 3.8b) from the LES simulation are very close to the experimental values and DLR LES simulation.

Table 3.7: Initial vortex parameters.

Parameter	Value
b_0	0.153 [m]
Γ_0	0.052 [m^2/s]
Initial height	0.0765 [m]
V_0	0.043 [m/s]
$r_{c,0}$	0.009 [m]
Re_Γ	52000

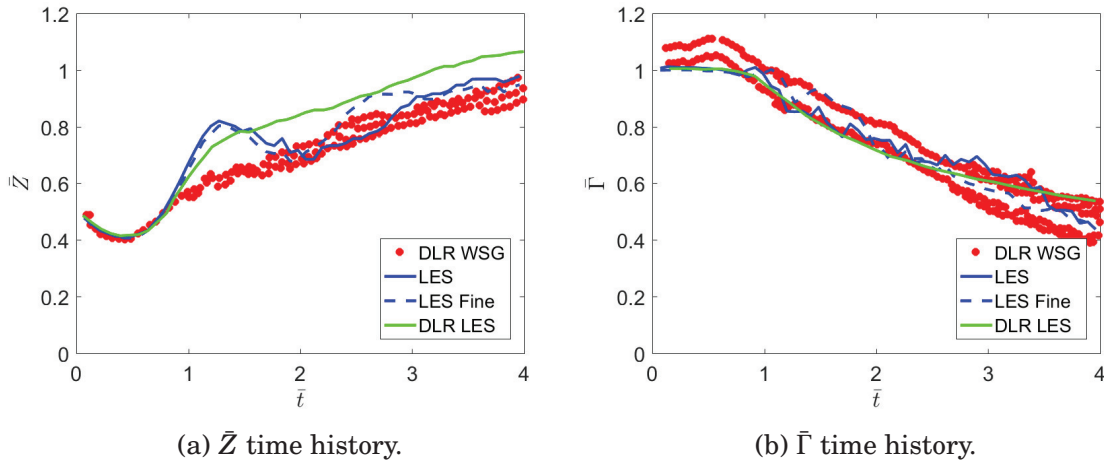


Figure 3.8: Comparison with the experimental data.

3.2.3 Forest Canopy

The forest canopy is modeled as a zone with porous medium defined as a solid matrix with interconnected pores. An isotropic porous medium with uniform

distributions of porosity properties in all directions is specified for simplicity. The following values of the coefficients D and F in Equation 3.2 are calculated using Ergun's equation (Ergun, 1952):

$$F = \frac{3.5}{d_p} \frac{1-\phi}{\phi^3} \quad (3.3)$$

$$D = \frac{150}{d_p^2} \frac{(1-\phi)^2}{\phi^3}$$

where ϕ is porosity, d_p is the mean particle diameter.

These parameters are calculated for two types of the forest canopies: the tomato canopy ($\phi = 0.9$) and deciduous forest which has relatively low porosity level ($\phi = 0.77$). The wind tunnel measurements of aerodynamic properties of a tomato canopy (Sase et al., 2012) are used to obtain F and D values. The porosity parameters for the canopy are found by measuring the pressure loss through the canopy for five velocity values. Thus, the permeability of the porous medium K is determined experimentally. Note that \sqrt{K} corresponds to the characteristic dimension of the porous medium (e.g. dimension of the average pore). \sqrt{K} is determined experimentally to be 0.13 m. Then, using Kozeny's equation (*Momentum Equations for Porous Media*, n.d.),

$$K = \frac{d_p^2 \phi^3}{180(1-\phi)^2} \quad (3.4)$$

the mean particle diameter is calculated. As a result, the values of 0.9 and 0.18385 are used for ϕ and d_p in the current simulations. Based on the study conducted to determine the drag coefficient and relationship between the permeability and the momentum loss coefficients of a tomato canopy for the various leaf area densities, the resulting values of $F = 2.6$ and $D = 60.876$ are selected. For the hardwoods, the permeability ($K = 0.005$) is found from (Crasto, 2007) and (Wallbank, 2008). Crasto performed the numerical simulations of the atmospheric boundary layer using WindSim software and their validations with the wind tunnel experiments. The various parameters for several types of the forests were derived. Based on this analysis, the values for $D = 172.5$ and $F = 5.46$ are established for the hardwoods and employed in the current study.

3.2.4 Forest Canopy Parametric Study

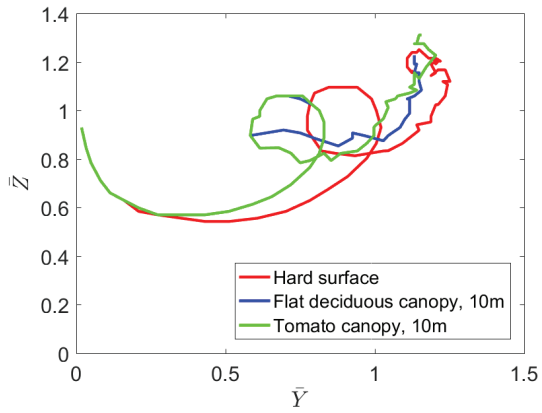
Flat Canopies

In Figure 3.9, the time histories of the vertical (\bar{Z}) and horizontal position (\bar{Y}) as well as the vortex strength ($\bar{\Gamma}_{5-15}$) are compared against those for the hard surface. The slope of the vertical time history curves for the porous and hard surfaces coincides until $\bar{t} = 1$. At $\bar{t} = 1$, the rebound occurs. However, the rebound peaks appear different. It is worth noting that the 'rebounding hump' is presented for the hard and both porous surfaces. Such a behavior can be explained by the dynamics of secondary vortices. The development of the secondary vortex tends to arrest the primary's vortex horizontal motion. In the canopy case, the secondary vortex detaches earlier than in hard surface case rotating around the

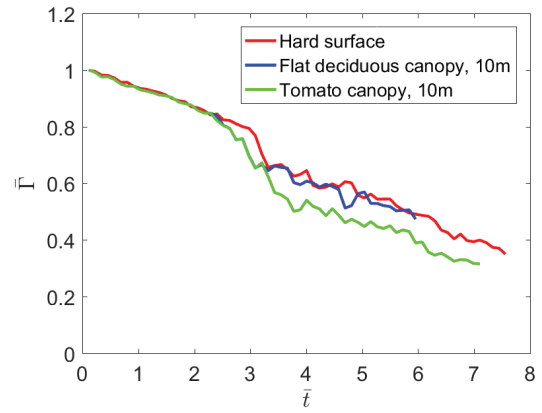
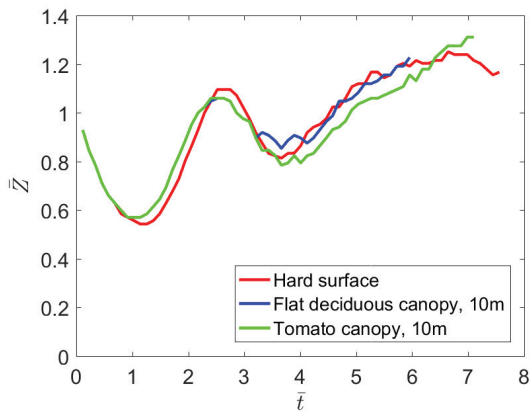
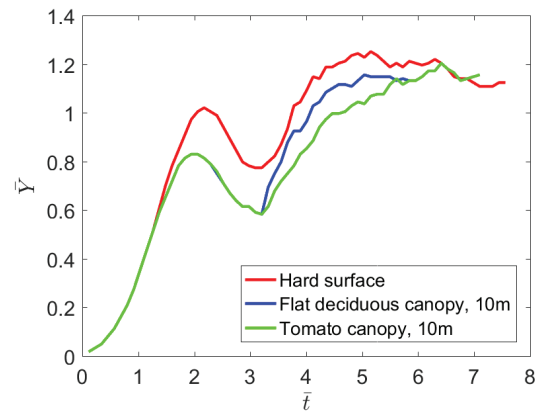
primary vortex faster thus limiting the horizontal deviation. At $\bar{t} = 3.8$, the second rebound is initiated. It is clear that the vortex dynamics for the deciduous canopy is different from the tomato canopy surface case. Figure 3.9a demonstrates the wake vortex behavior in space more clear. The rebound in both porous cases occurs earlier.

The circulation evolution results in Figure 3.9b indicate a similar decay rate starting from $\bar{t} = 4$ for the canopy and hard surface cases. As discussed before, the dynamics of the primary vortices and the loss of the momentum due to penetration of the flow in the porous surface are the possible reasons for the faster decay of the wake vortex in case of the canopy surface. The properties of the deciduous surface are closer to the hard surface case, which results in slower decay of the vortex strength in comparison with the tomato surface case.

Figures 3.10 and 3.11 demonstrate the vorticity fields for two moments of time. At the early stage (Figure 3.10), the difference in the formation of the secondary vortices can be noted. Also, the dynamics of the secondary vortices for deciduous canopy case is closer to the hard surface case than for the tomato case because of the larger difference in porosity and permeability. The same can be noticed in Figure 3.11 for $\bar{t} = 3.78$. The numerous coherent structures observed in the canopy cases point to the higher circulation decay rates, which is also clear from Figure 3.9b.

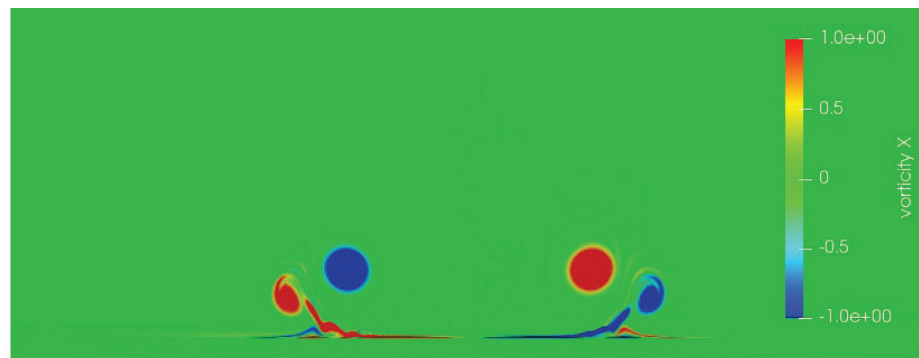


(a) Position.

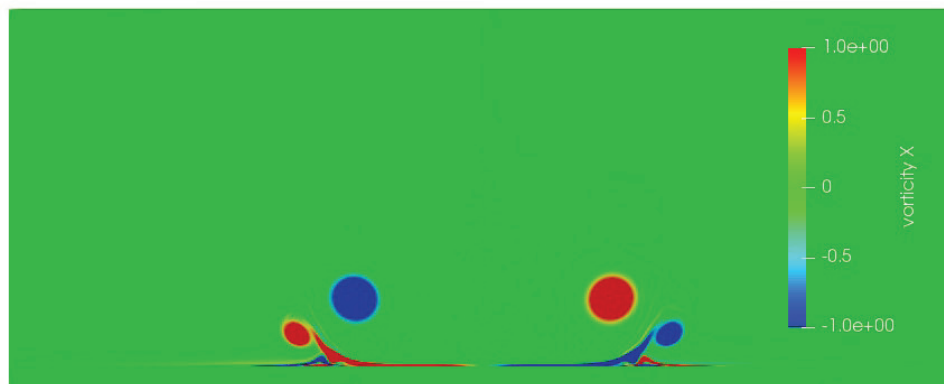
(b) \bar{I} time history.(c) \bar{Z} time history.(d) \bar{Y} time history.Figure 3.9: Position and \bar{I}_{5-15} over the flat surfaces.



(a) Hard Surface.

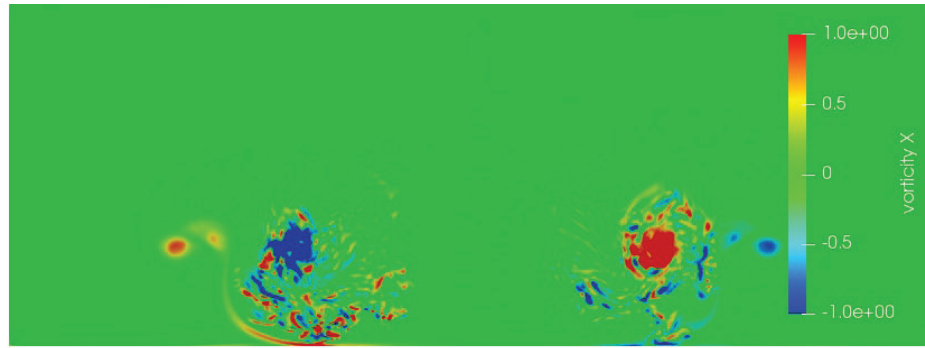


(b) Tomato canopy, 10m.

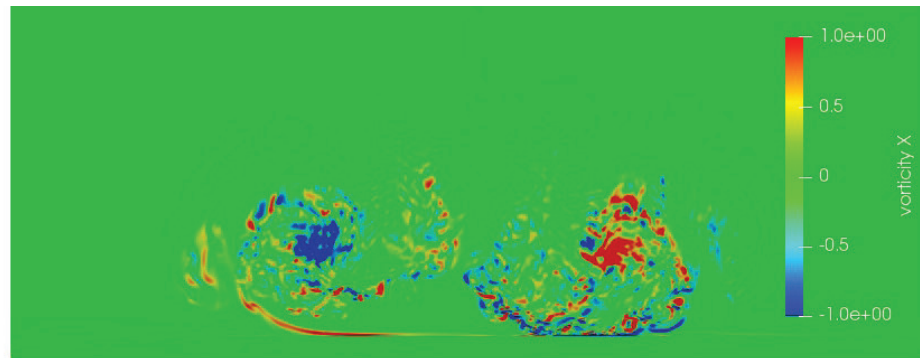


(c) Deciduous canopy, 10m.

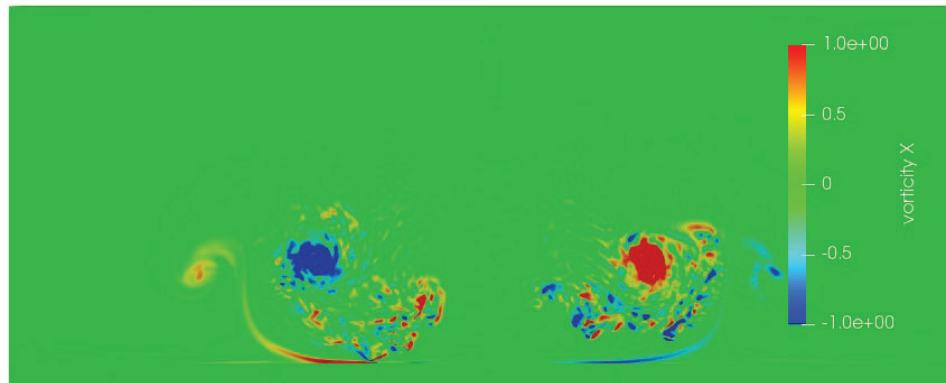
Figure 3.10: Vorticity fields for $\bar{t} = 1.26$, $\bar{x}^* = 2.04$.



(a) Hard Surface.



(b) Tomato canopy, 10m.



(c) Deciduous canopy, 10m.

Figure 3.11: Vorticity fields for $\bar{t} = 3.78$, $\bar{x}^* = 2.04$.

Canopies of Different Heights

The flow over the hardwoods of $5m$ and $10m$ height is analyzed in this subsection. As expected, the vortex pair dynamics in the case of the lower canopy is close to the hard surface case. Indeed, the circulation time history and position in space (Figure 3.12) clearly indicate this. However, the distinction in vortex pair's position between $5m$ and $10m$ canopy cases is obvious. The difference in the horizontal position offset for $\bar{t} = 2$ (Figures 3.12a and 3.12d) between hard surface case and tomato canopy case is about $0.2b_0$. A closer look at Figures 3.13 and 3.14 reveals an apparent difference in the formation of the secondary vortices.

Rough Canopy

The effect of the canopy roughness is investigated in this section using the cases of the flat tomato canopy of $10m$ height and the rough surface. First, tomato canopy Roughness with “tree” cross section of $3m \times 3m$ is considered. As shown below, the ground surface roughness effect on the vortex pair's circulation is similar to the effect of an obstacle (Wang et al., 2017; Stephan et al., 2014). However, in comparison to the obstacle effect (Wang et al., 2017), the circulation level drops slightly slower. In Figure 3.16, the effect of roughness is pronounced in terms of the secondary vortex structures wrapping around the primary vortices and starting to accelerate the wake vortex decay. Already at $\bar{t} = 0.69$, (Figure 3.18), the secondary vortex structures are different from those above the flat surfaces. In Figure 3.19, one can observe the absence of the pronounced secondary vortices above the rough surface as opposed to flat surfaces. From Figure 3.16, it is clear

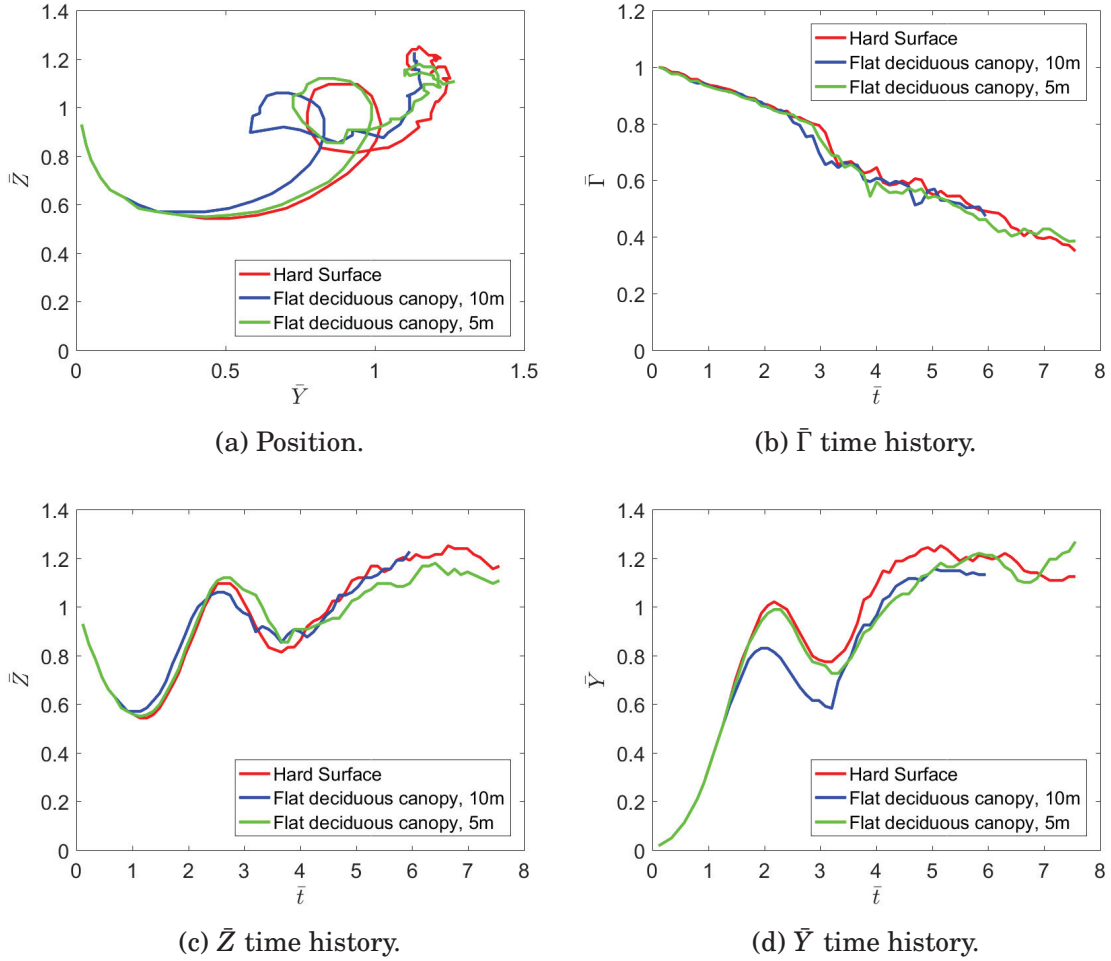


Figure 3.12: Position and $\bar{\Gamma}_{5-15}$ over the flat porous surfaces of different height.

that roughness produces strong secondary vortex structures in comparison to the flat tomato canopy. Moreover, above the rough surface, a tremendous reduction of circulation strengths between $\bar{t} = 1$ and $\bar{t} = 2$ compared with the hard surface and flat canopy cases is observed. The reduction is around 40% – 50%. The circulation plots (Figure 3.15b) show significant dissipation for the rough case at $\bar{t} = 3$. The intensity of the wake vortex ($\bar{\Gamma} = 0.4$) possibly may have a very little effect on the follower aircraft.



(a) Hard surface.

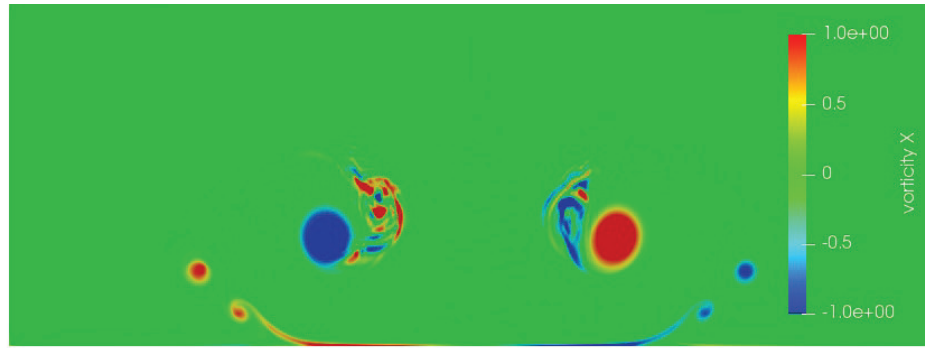


(b) Deciduous canopy, 10m.

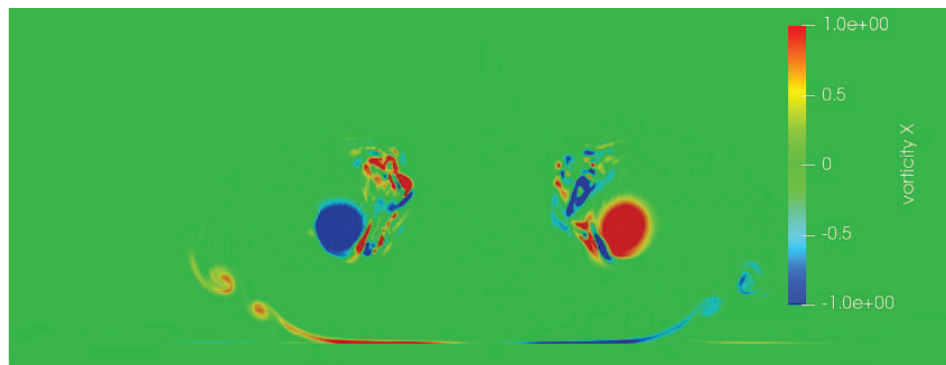


(c) Deciduous canopy, 5m.

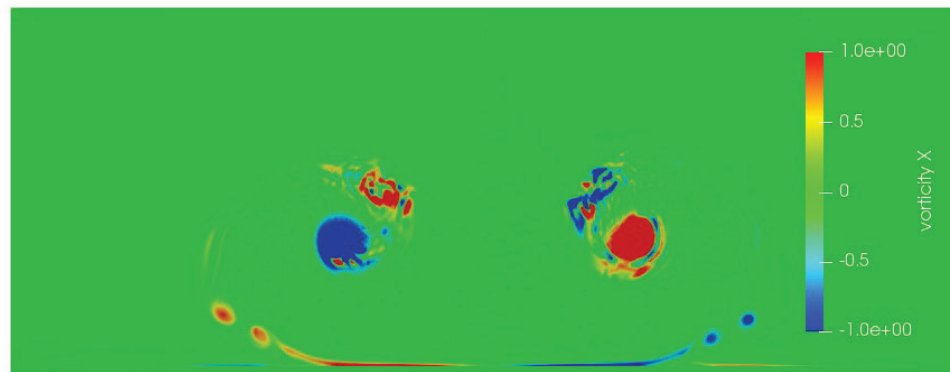
Figure 3.13: Vorticity fields for $\bar{t} = 1.03$, $\bar{x}^* = 2.04$.



(a) Hard surface.



(b) Deciduous canopy, 10m.



(c) Deciduous canopy, 5m.

Figure 3.14: Vorticity fields for $\bar{t} = 2.86$, $\bar{x}^* = 2.04$.

Figures 3.15a and 3.15c demonstrate the impact of a rough surface on the wake vortex rebound height. The first dip (at $\bar{t} = 1$) of the vortex pair is higher for the rough case (Figure 3.15c). After rebound, the vortex pair rises with approximately similar rate for all cases. It is worth noting that the wake vortex does not descend after it reaches the first peak (in comparison with two other cases) and continues to rise reaching the maximum of $\bar{Z} = 1.3$. The horizontal motion also differs in the rough case. As opposed to vertical ascend and rebound distance, the horizontal deviation is lower for the rough case.

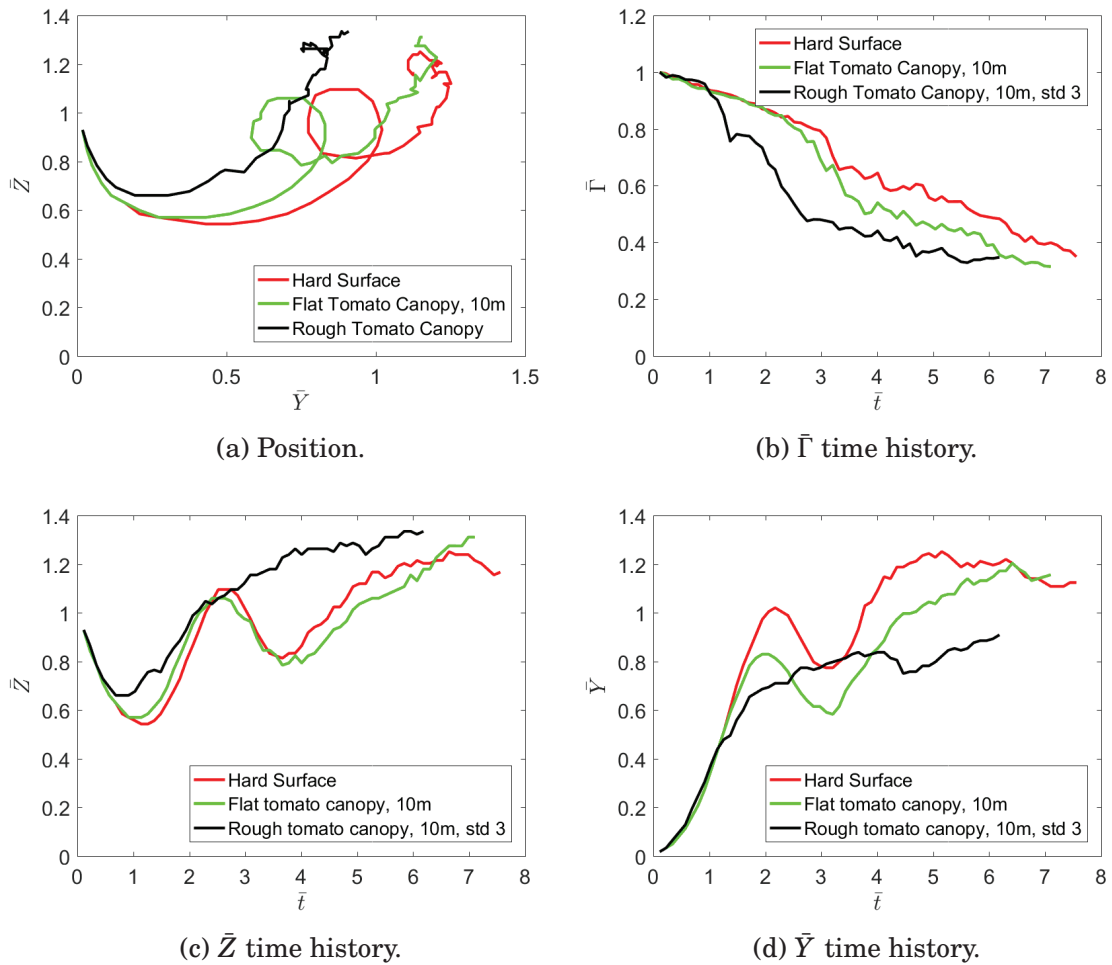
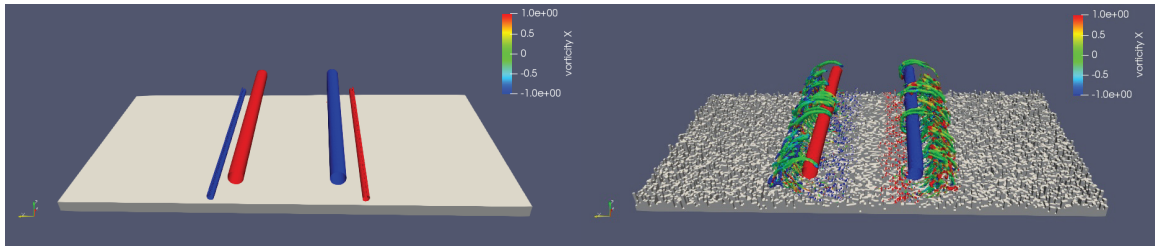
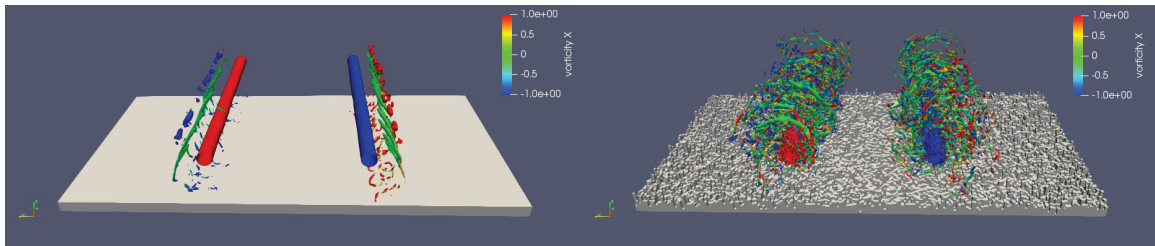


Figure 3.15: Position and $\bar{\Gamma}_{5-15}$ over the flat porous surfaces of different height.



(a) Tomato canopy.

(b) Rough tomato canopy.

Figure 3.16: $Q = 0.5$ isosurface with vorticity coloring, $\bar{t} = 1.03$.

(a) Tomato canopy.

(b) Rough tomato canopy.

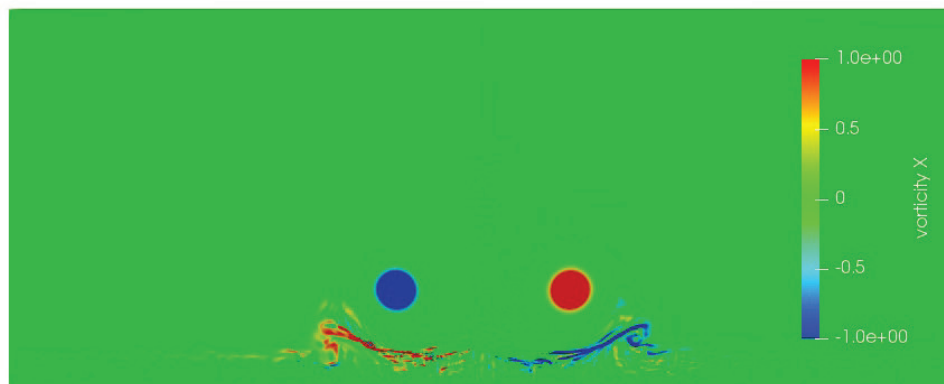
Figure 3.17: $Q = 0.5$ isosurface with vorticity coloring, $\bar{t} = 2.06$.



(a) Hard surface.

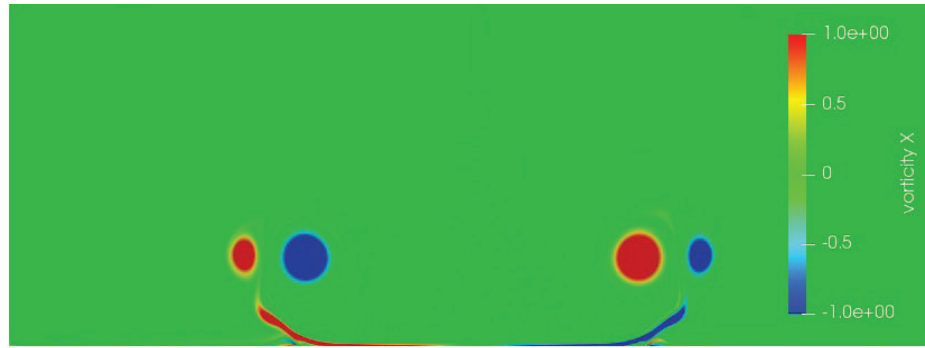


(b) Tomato canopy, 10 m.

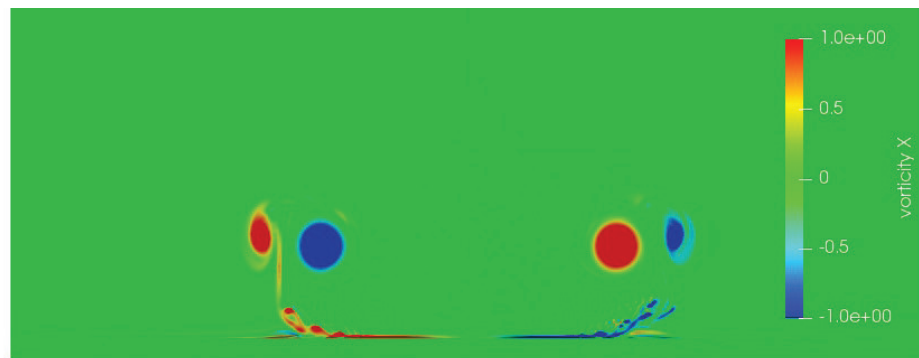


(c) Rough tomato canopy, 10 m with std 3 m.

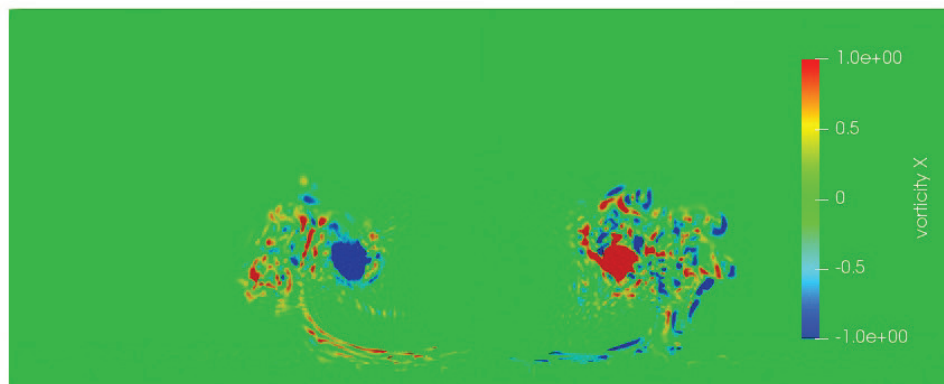
Figure 3.18: Vorticity fields for $\bar{t} = 0.69$, $\bar{x}^* = 2.04$.



(a) Hard surface.



(b) Tomato canopy, 10 m.



(c) Rough tomato canopy, 10 m with std 3 m.

Figure 3.19: Vorticity fields for $\bar{t} = 1.72$, $\bar{x}^* = 1.72$.

Next, the deciduous canopy roughness with 'tree' cross section of $6m \times 6m$ is presented. In case of the rough hardwoods (deciduous canopy), the vortex strength drops with the same rate as it does in case of the tomato canopy (Figure 3.20b). The rebound height over the rough deciduous canopy case exceeds the one in the case of the rough tomato canopy (Figure 3.20c). On the contrary, the horizontal offset from the initial position is the smallest for the deciduous canopy. Thus, one can conclude that roughness contributes the most in the vortex decay. Also, the change of the "roughness" or "tree" size by the factor of 2 does not change the decay rate significantly.

Canopy Clearing

Finally, we discuss the preliminary study of the vortex pair evolution over a canopy clearing. The canopy clearing is the porous zone of the reduced size which occupies only the half of the attached region (Figure 3.22). The vortex pair's parameters are obtained for the slice over the forest surface ($x^* = 1.02$, forest part) and the slice over the forest clearing surface itself ($x^* = 2.04$, clearing part). In addition, Q -isosurfaces ($Q=0.1$) with vorticity coloring are shown for four moments of time (Figure 3.22). All the parameters are compared with those in the hard surface and tomato canopy surface cases.

The wake vortices are disturbed near the boundaries, which is due to the application of the periodic boundary condition (Figure 3.22). The same phenomena is described by (Misaka et al., 2011), where the airplane was moved through the domain. As a result, the wake development during the flight violated the

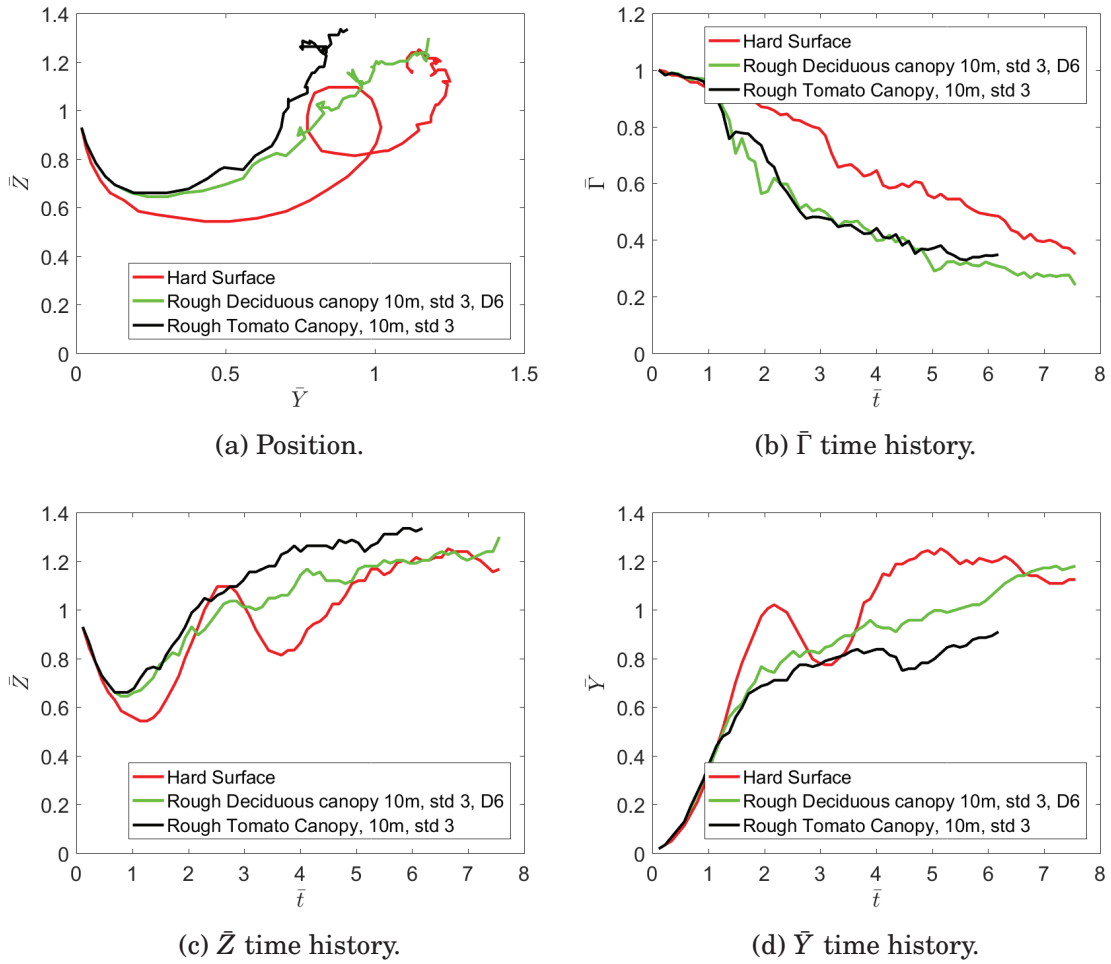


Figure 3.20: Position and $\bar{\Gamma}_{5-15}$ over the flat porous surfaces of different height.

flow periodicity. In our case, the periodicity of the flow is also violated due to the presence of the porous region near one of the boundaries. Nevertheless, the periodic boundary condition is imposed in this work to insure the stability of the numerical solution.

Considering the circulation time history (Figure 3.21b), one can observe a significant drop from $\bar{t} = 2$ to $\bar{t} = 3$ for both clearing and forest parts. Note, that the observed decay rate is quite different from both the tomato canopy and the

hard surface cases. This may be explained as follows. One of the possible reasons is the periodic boundary conditions in the x-direction discussed above. Second, the deformation of the left and right vortices towards each other may trigger the formation of the secondary vortex structures. As can be seen from the Figure 3.22, the vortex disturbances rapidly propagate through the vortex structures. Finally, the size of the domain in the x-direction may be too small and is shown to be an important parameter in the studies with obstacle (Stephan et al., 2014).

The time history of the position of the vortex core is shown in the Figures 3.21a, 3.21c and 3.21d. Approximately at $\bar{t} = 1.5$, the vortex over the forest part stops following the trajectory of the one over the tomato canopy case and stays almost in the same position. As for the clearing part, the vortex pair almost stops rising after $\bar{t} = 2$ and as a result resides lower than in other three cases.

3.2.5 Water Surface

The obtained results indicate that the flow over the free surface is quite different from the flow over the hard surface or porous medium. Indeed, while the flux of vorticity over a solid boundary is proportional to the surface pressure gradient, such flux for the free surface is proportional to the fluid acceleration at the free surface interface (Rood, 1994). Furthermore, the vortex interaction can cause deformation of the surface, and the vortex interaction with the free surface boundary does not depend on the dynamics of the fluid on the other side of the boundary (Rood, 1994).

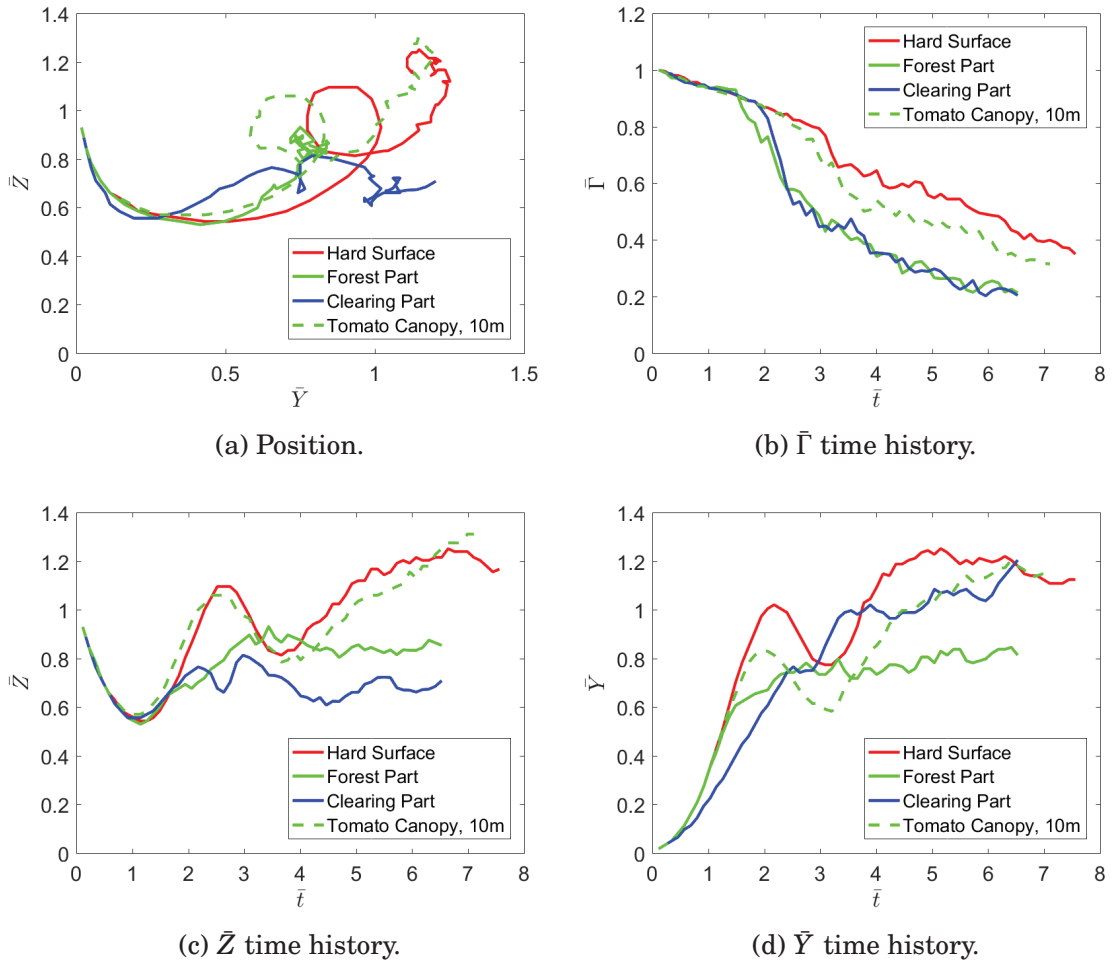


Figure 3.21: Position and $\bar{\Gamma}_{5-15}$ over the forest clearing.

3.2.6 Comparison and Discussion of Results

Vertical and horizontal time history as well as the vortex strength evolution are shown in the Figures 3.23 and 3.24. Figure 3.26 demonstrates the circulation time history for three cases. The cross plane at $x = 41$ m is shown.

The slope of the vertical time history curves for the porous and hard surfaces agrees well. However, the rebound peaks appear different. As discussed in Section 3.2 and 3.2.1, such differences are caused by different dynamics of secondary

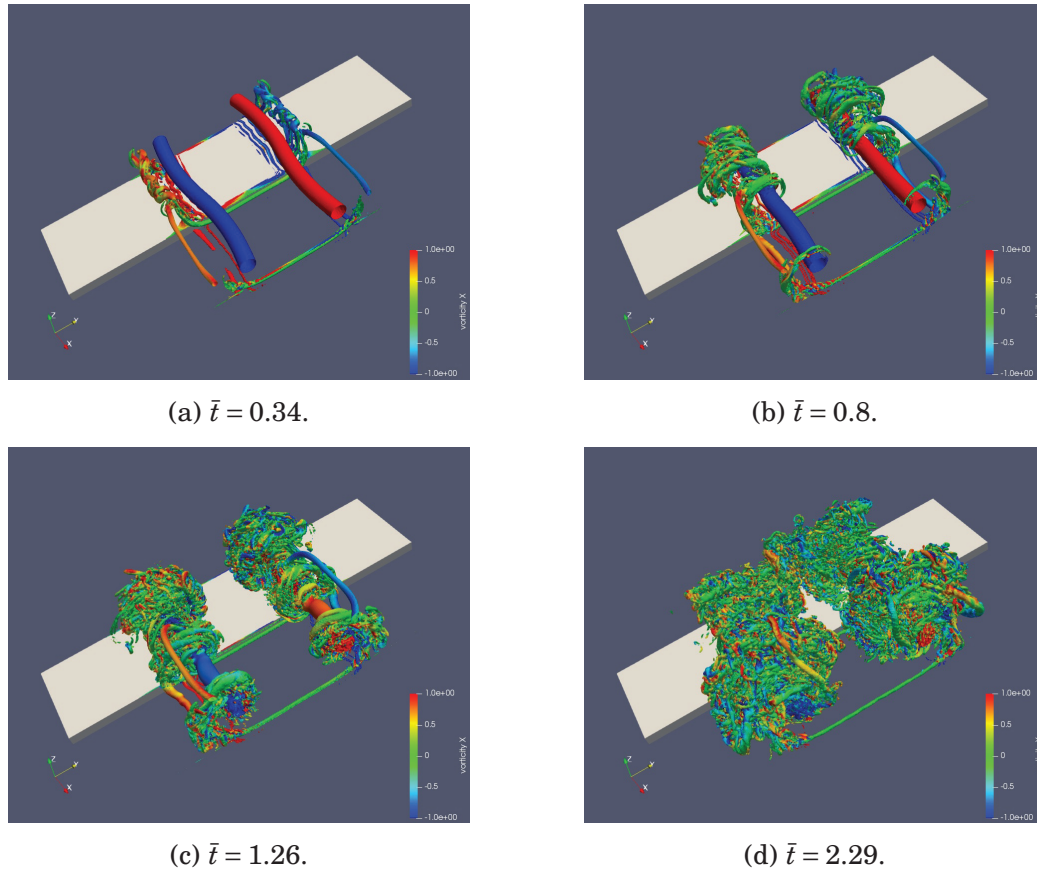


Figure 3.22: $Q = 0.1$ isosurfaces with vorticity coloring.

vortices. It is worth noting that the 'rebounding hump' is present for both hard and porous surfaces but disappears for the water surface case.

The circulation evolution results in Figure 3.24 indicate a faster decay from $\bar{t}=0$ to 1 in the water surface case. Numerous coherent structures start deforming the primary vortex at $\bar{t} = 0.95$ (Figure 3.25b). The same can be noticed in Figure 3.27b. After $\bar{t} = 1$, the slope of the circulation curve for water case remains almost the same. However, for hard surface and especially for porous surface case, it becomes more steep after $\bar{t} = 2$. Indeed, Figures 3.25, 3.28 also demonstrate that after $\bar{t} = 2$ the coherent structures start to greatly affect the primary vortices in

both hard and porous medium cases. The vortex sheet on the water surface exhibits a stronger dynamics of vortical structures (Figures 3.27 and 3.28) compared to the hard and porous surface cases.

According to the experimental results of (Shaikh & Siddiqui, 2010), the magnitude of the normalized Reynolds stress in the near surface region is higher over the water surface in comparison to the solid wall. Thus, the viscous dissipation for the water surface case is more intensive, which agrees with the current results. Moreover, the TKE production over the water surface was found to be the highest in comparison with smooth wall case and enhanced in the presence of waves which is likely due to enhancement of the Reynolds stress (Shaikh & Siddiqui, 2010). The highest magnitudes of TKE dissipation rate are also observed in the water surface case.

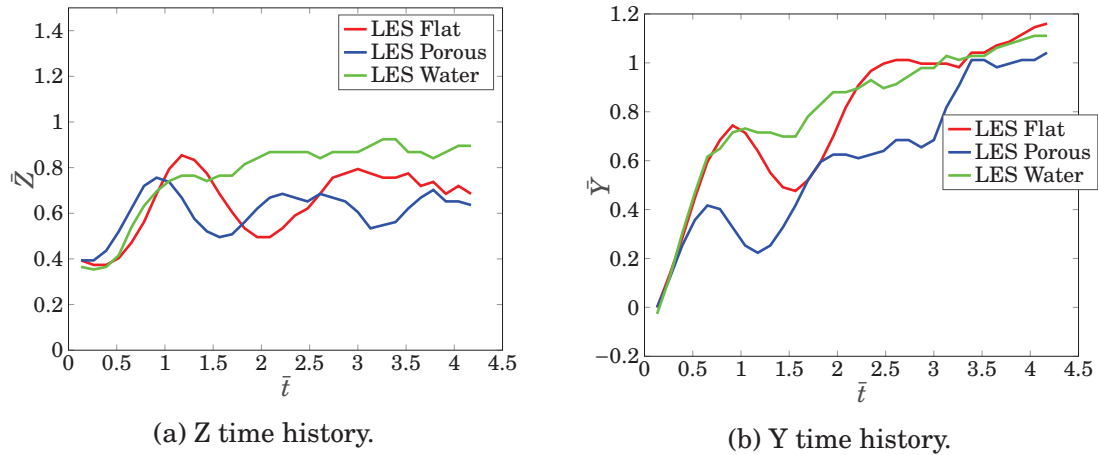


Figure 3.23: Position for three surfaces.

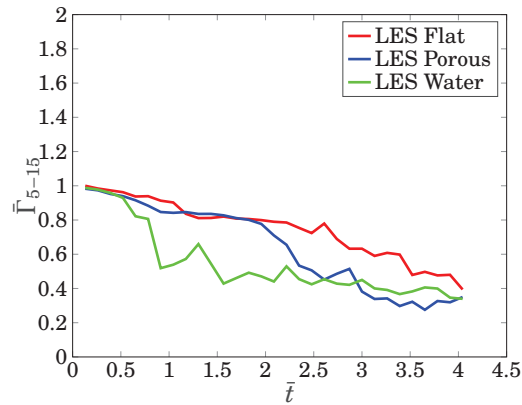


Figure 3.24: Circulation for three surfaces.

3.3 High-Fidelity Based Reduced Order Model of In-ground Effects for WVSS

The vortex pair is considered to be In-Ground-Effect when the separation from the ground is less than b . It is very important to predict the wake vortex behavior in the vicinity of the ground especially in terminal zones. The effect of the ground on wake-vortex evolution has been widely studied by (Proctor et al., 2000; Harvey & Perry, 1971; Holzapfel & Steen, 2007; Burnham, Hallock, Tombach, Brashears, & Barber, 1978). It is known that the vortex decay is enhanced near the ground and it is a complex phenomenon. In order to predict the behavior of the vortex pair in the in-ground zone, one need to take into account the interaction of the vortex pair (primary vortices) with the surface boundary layer. Several fast-time models exist which can predict the in-ground evolution of the wake vortex (e.g. APA, TDP etc). In this section, a reduced order model of in-ground effect is developed based on high-fidelity simulation for incorporation in the WVSS fast-time prediction code.

3.3.1 Reduced-order model approach

The reduced order model approach is based on high-fidelity LES simulations described in the previous section. The wake vortex initial separation and distance (b), initial height over the ground h_0 and initial circulation Γ_0 are considered to be the main parameters which affect the dynamics of the wake vortex near the ground. The in-ground model should cover the wide range of b, h_0 and Γ_0 parameters in order to be able to predict the behavior of the vortex pair generated by different aircraft's which can belong to different categories. For that reason, the "2-D computational grid" which consists of possible combinations of Γ_0 and b is considered.

The "nodes" in the grid correspond to transient LES simulations of the wake vortex evolution near the ground with the parameters chosen and $h_0 = b$. The "2-D computational grid" can be used in WVSS to model the behavior of the vortex pair in the vicinity of the ground. The values at the points between the nodes can be found by interpolation between the LES -"calculated" nodes. The choice of interpolation points is also discussed and the results are validated against the existing fast-time model with in-ground effect (APA 3.8).

The "2-D computational grid" is shown in Figure 3.29. This is an example of the grid which can be used in the real simulations and it covers the $200 \text{ m}^2/\text{s} - 400 \text{ m}^2/\text{s}$ circulation range and $30 \text{ m} - 50 \text{ m}$ spacing range. It can be expanded to cover the bigger range of circulation and spacing sizes of the airplanes. The blue

dots are the points which were calculated from LES simulation only, the green ones are calculated and modeled using the interpolation from adjacent points.

Four different types of interpolation are considered:

- vertical point interpolation (points with the same spacing but with different circulations are used)
- horizontal point interpolation (points with the same circulation but with different spacing are used)
- diagonal point interpolation
- four-points interpolation

The results are shown in Figures 3.31, 3.32 and 3.33. The interpolation with the use of vertical (Figure 3.31) and horizontal (Figure 3.32) points can potentially work well for the circulation prediction and the horizontal position. However, the vertical coordinate of the vortex pair can be approximated by such interpolation only during the first 20 seconds of the descent. Figure 3.33 demonstrates the interpolation process where diagonal points, as well as all four points, are used. These two methods give better results than the first two considered. The black dashed line shows the result obtained from LES simulation and which is have to be modeled using interpolation. The cyan and green dots are the result of diagonal and four points interpolation. The diagonal interpolation seems to give better results which can be explained by the similarity of the flow with bigger spacing and bigger circulation values. Indeed, the intensity of interaction between two vortices is

stronger when they are closer and more strong and vice versa. Thus, there is no need to perform simulations for all the points in the grid. Instead of this one can use the diagonal points interpolation to find the values for a vertical and horizontal position as well as the circulation in the points of interest. It is possible to make the grid more dense depending on the computational power available. Moreover, the time histories for the position and vortex strength obtained in the nodes of the “2-D computational grid” can be used as uncertainty boundaries in simulations.

3.3.2 Comparison with APA 3.8 Fast-Time Model

The comparison of reduced-order model results with the existing APA 3.8 model is performed for three nodes: $\Gamma_0 = 200 \text{ m}^2/\text{s}, b = 30 \text{ m}; \Gamma_0 = 300 \text{ m}^2/\text{s}, b = 40 \text{ m}; \Gamma_0 = 400 \text{ m}^2/\text{s}, b = 50 \text{ m}$ and are shown in Figures 3.34, 3.35, 3.36. The vertical and horizontal position of LES and fast-time modeled solution (APA 3.8) as well as the vortex strengths are close to each other.

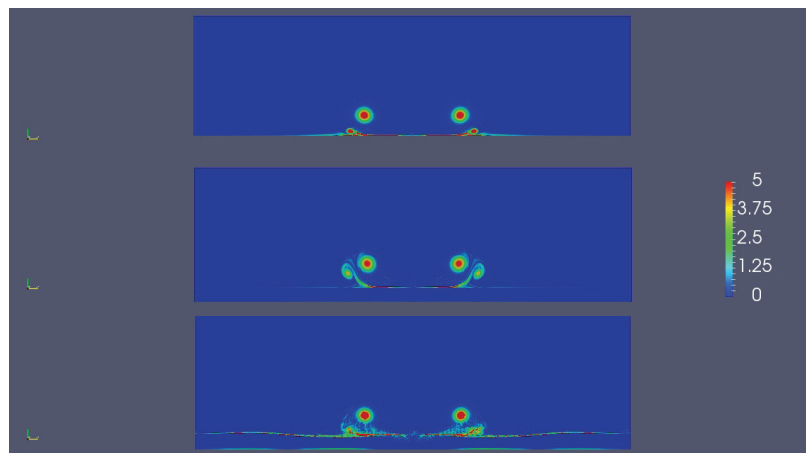
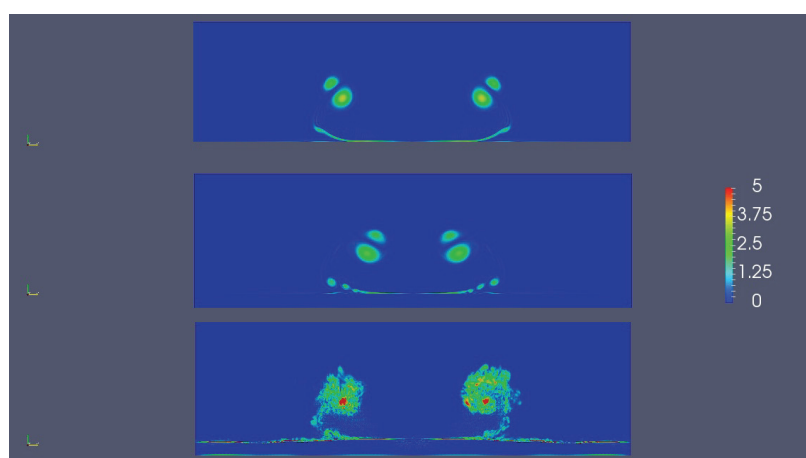
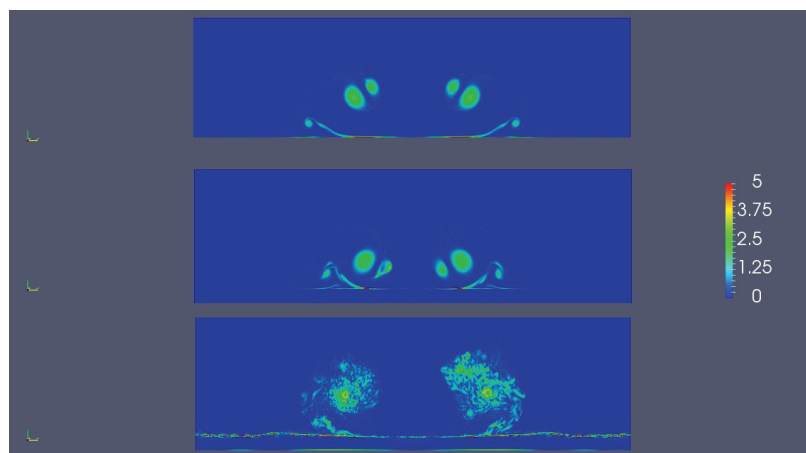
(a) $\bar{t} = 0.27$.(b) $\bar{t} = 0.95$.(c) $\bar{t} = 1.36$.

Figure 3.25: Circulation evolution for three surfaces.

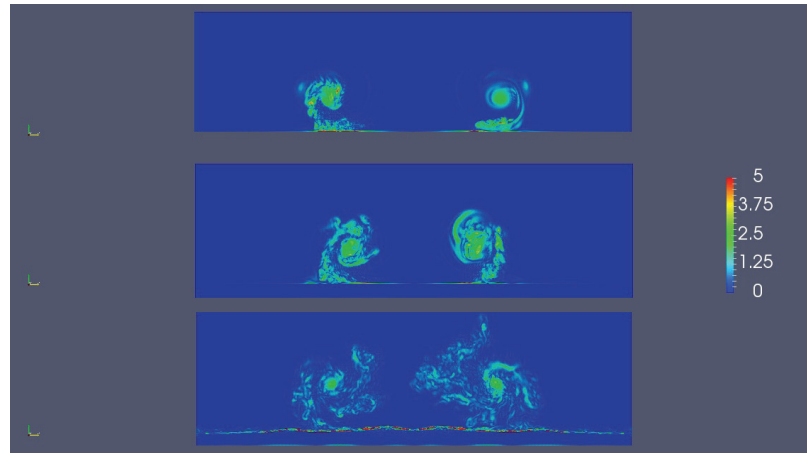
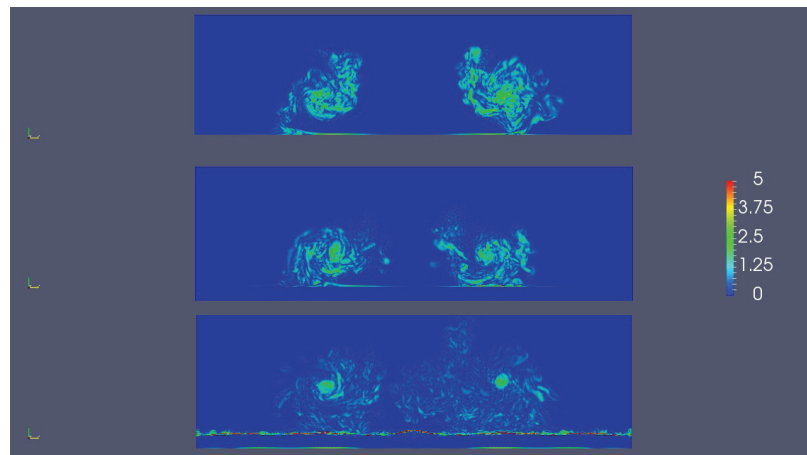
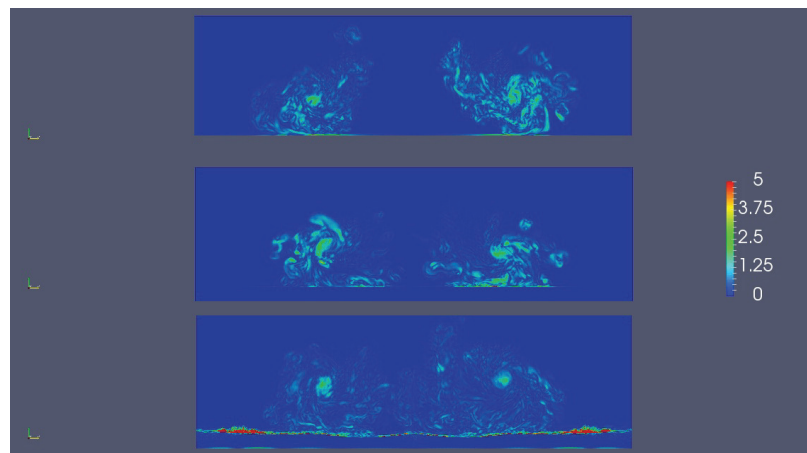
(a) $\bar{t} = 2.32$.(b) $\bar{t} = 3.4$.(c) $\bar{t} = 4$.

Figure 3.26: Circulation evolution for three surfaces.

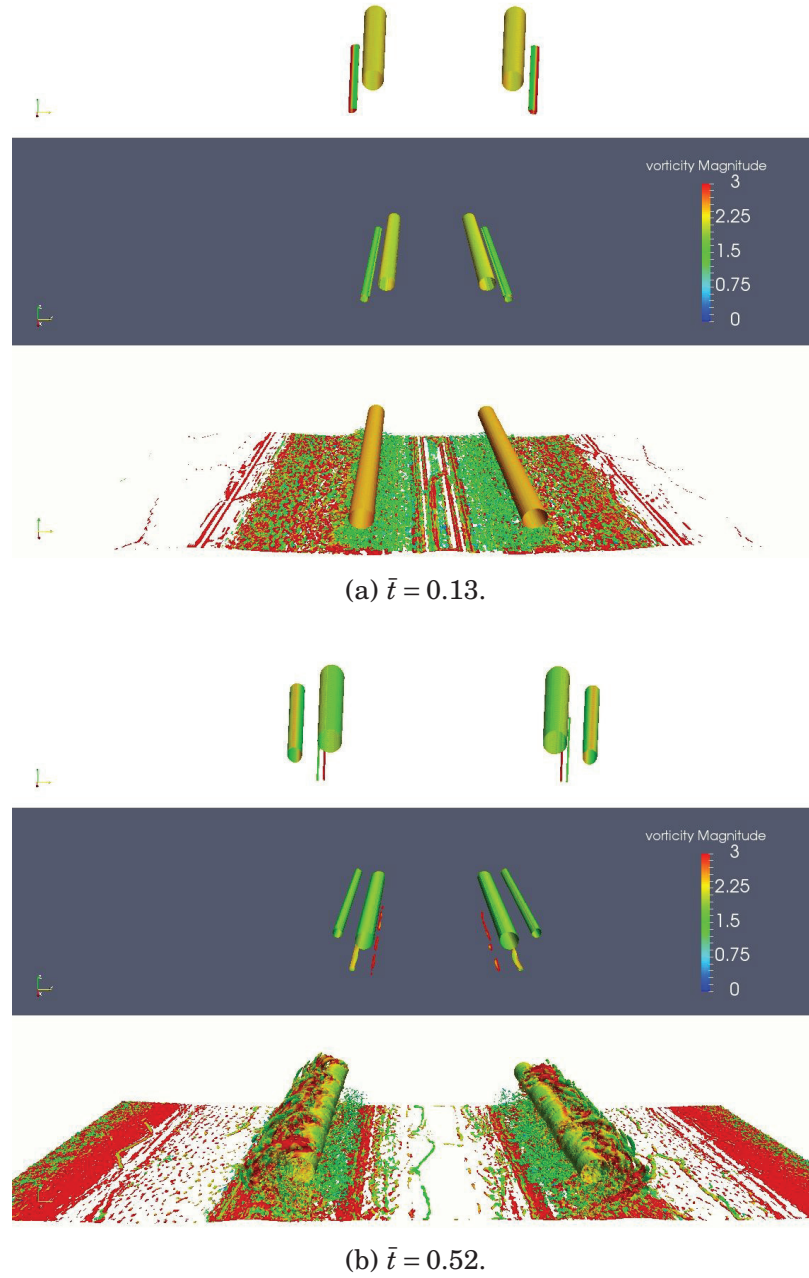


Figure 3.27: Wake vortex evolution with flat ground. Q isosurfaces ($|Q| = 0.5$).

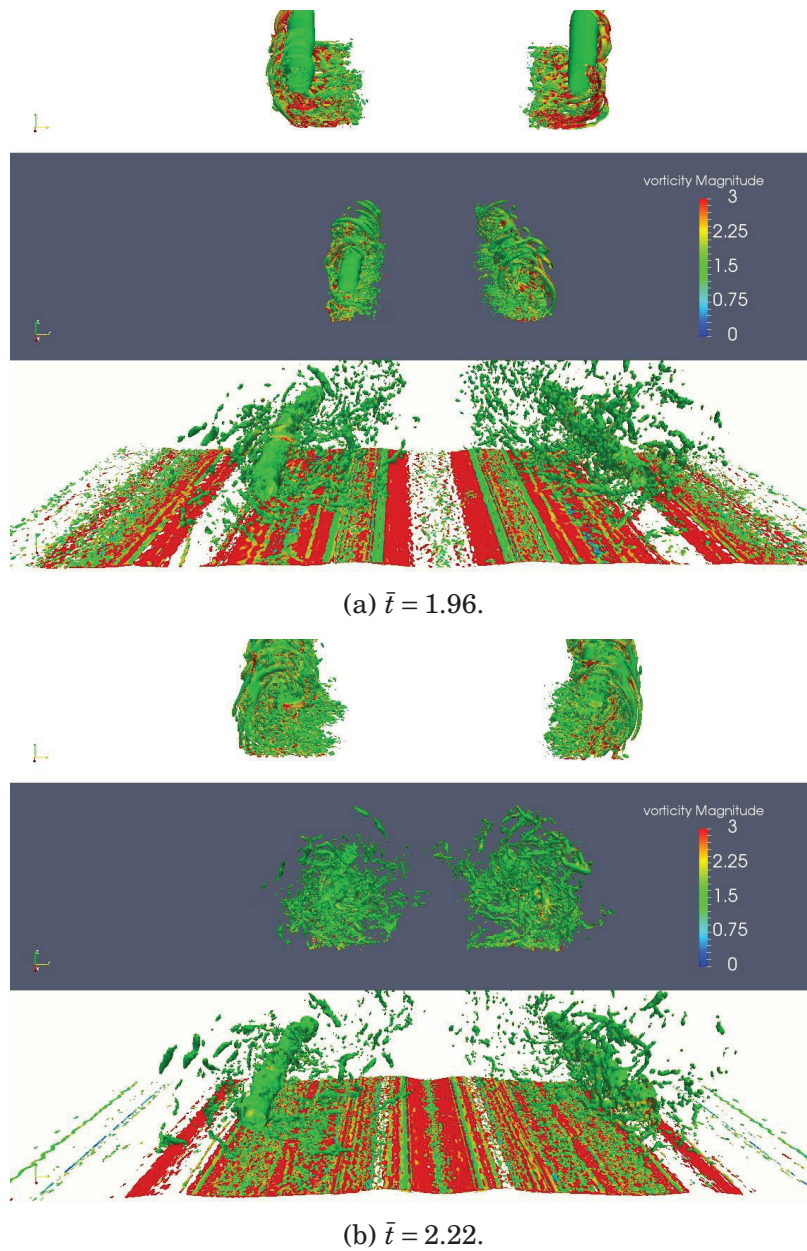


Figure 3.28: Wake vortex evolution with flat ground. Q isosurfaces ($|Q| = 0.5$).

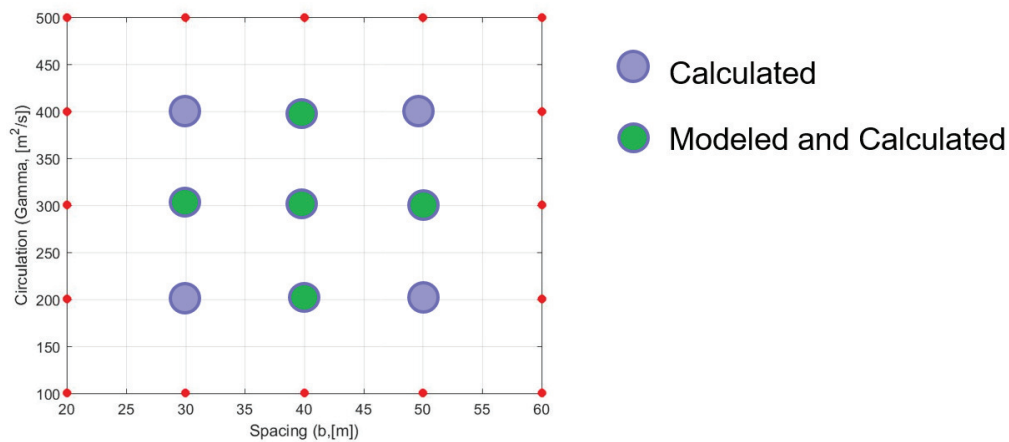


Figure 3.29: 2D computational grid.

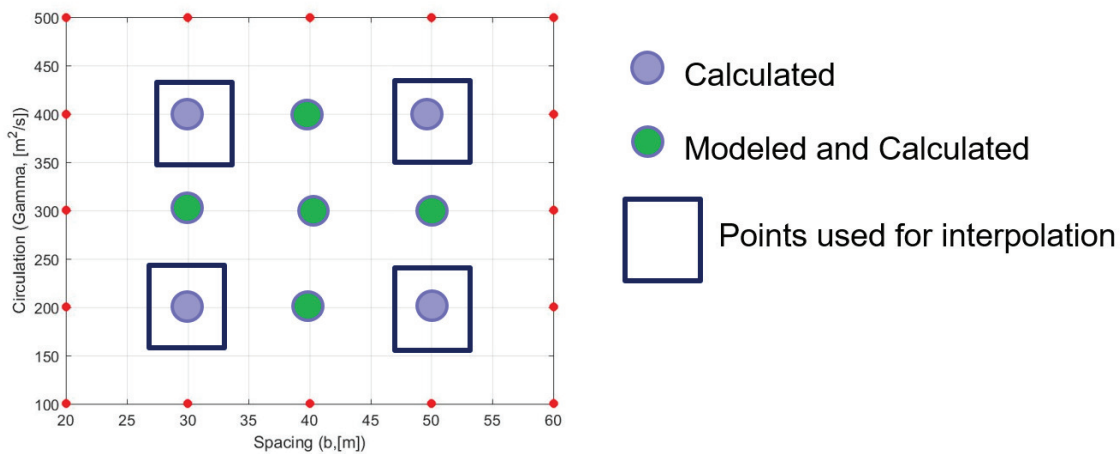
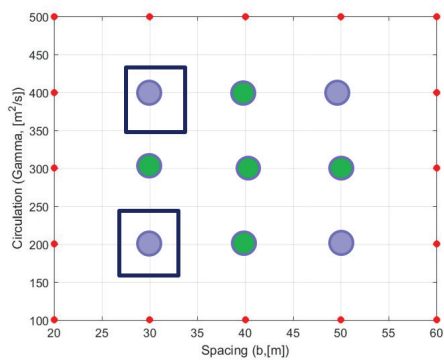
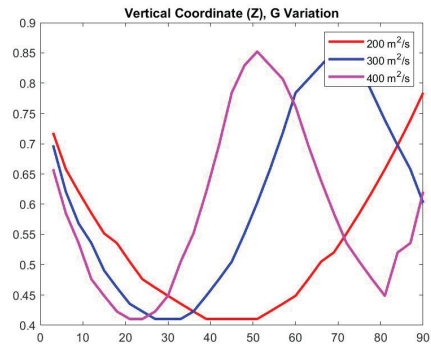


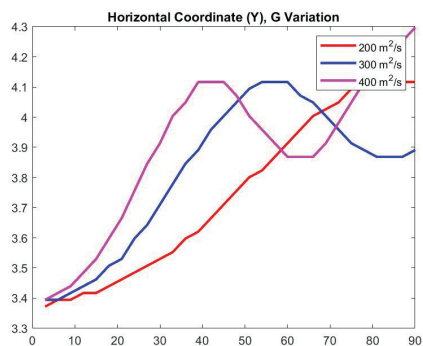
Figure 3.30: Interpolated, simulated and modeled points.



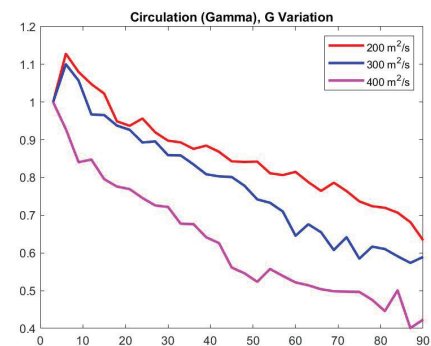
(a) Points used for interpolation.



(b) Vertical descent.

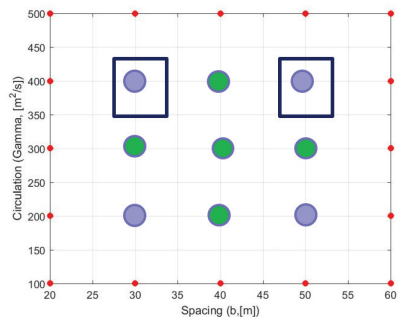


(c) Horizontal position.

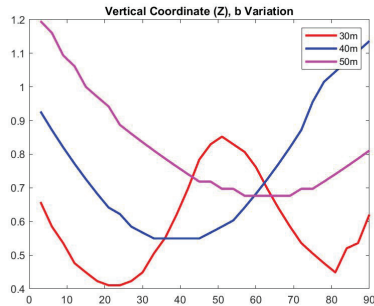


(d) Circulation evolution.

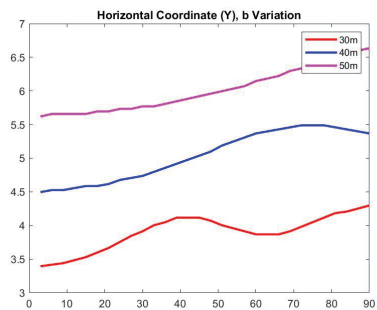
Figure 3.31: Position and strength for vertical interpolation points.



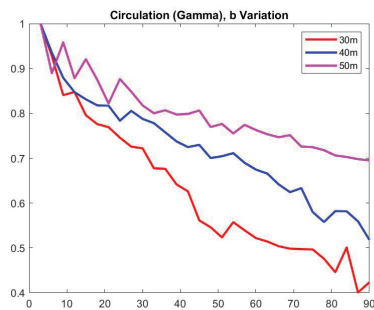
(a) Points used for interpolation.



(b) Vertical descent.

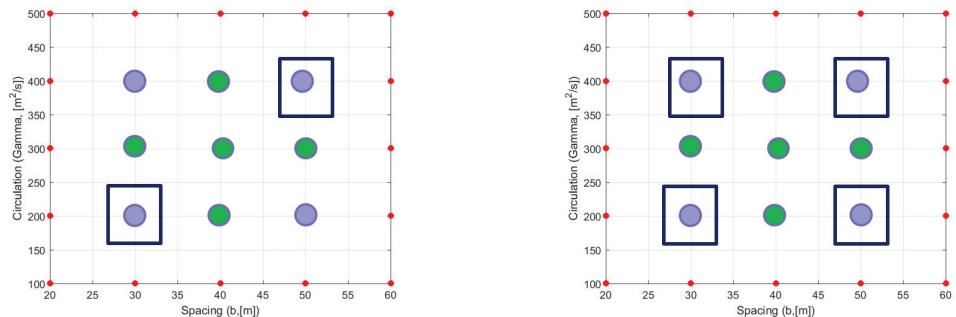


(c) Horizontal position.

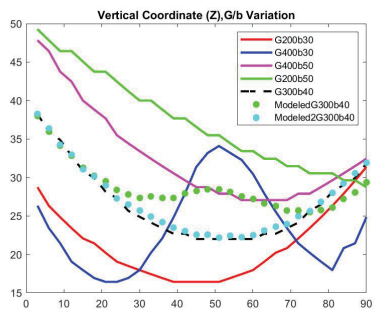


(d) Circulation evolution.

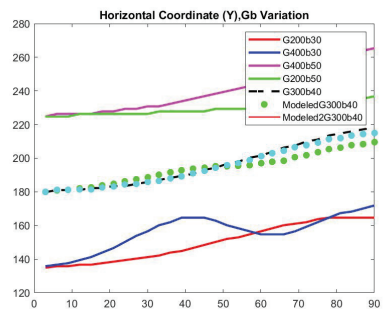
Figure 3.32: Position and strength for horizontal interpolation points.



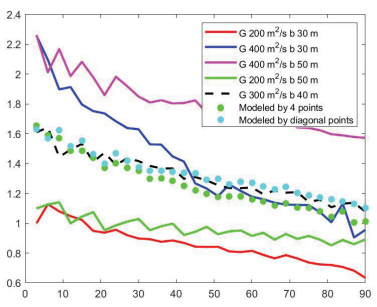
(a) Points used for diagonal interpolation. (b) Points used for 4-points interpolation.



(c) Vertical descent.

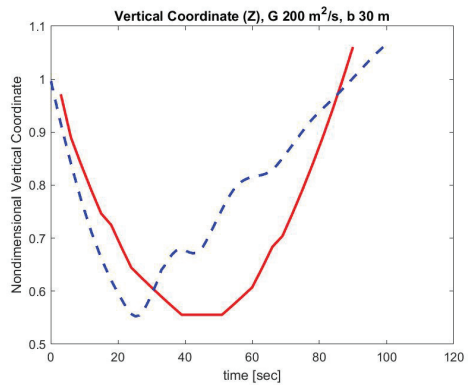


(d) Horizontal position.

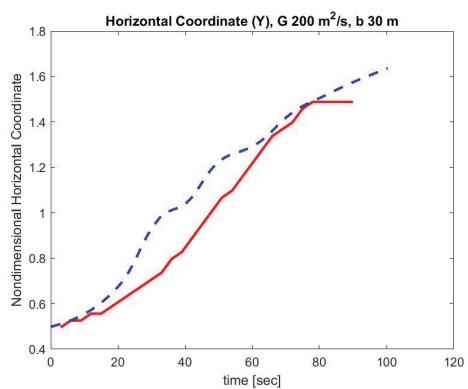


(e) Circulation evolution.

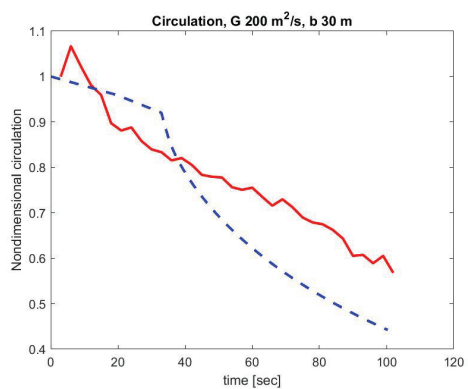
Figure 3.33: Position and strength for diagonal and 4-points interpolation.



(a) Vertical Descent.

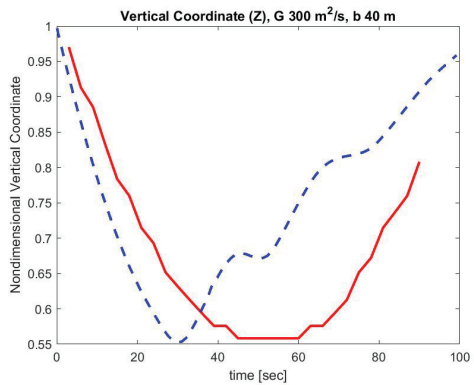


(b) Circulation Evolution.

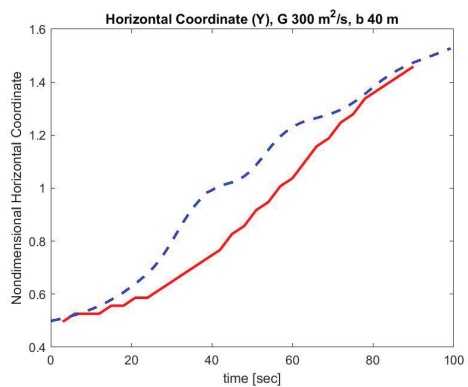


(c) Circulation Evolution.

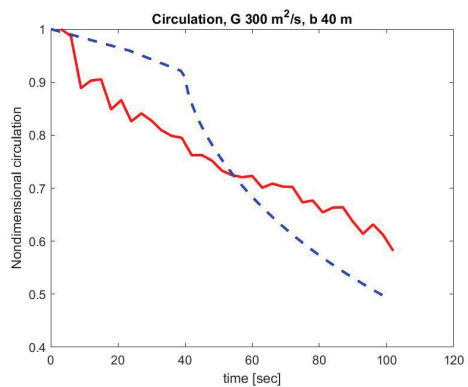
Figure 3.34: $\Gamma = 200 \text{ m}^2/\text{s}, b = 30\text{m}$. LES simulation (Red), APA 3.8 (Blue).



(a) Vertical Descent.

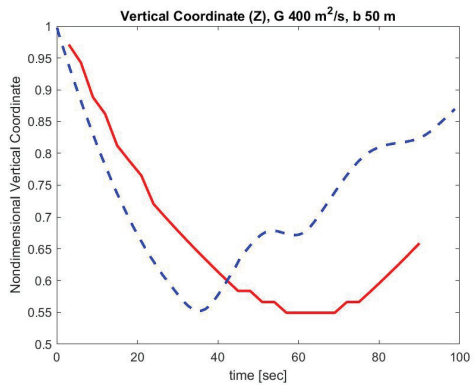


(b) Circulation Evolution.

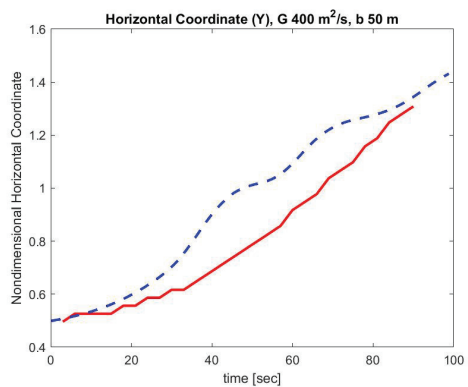


(c) Circulation Evolution.

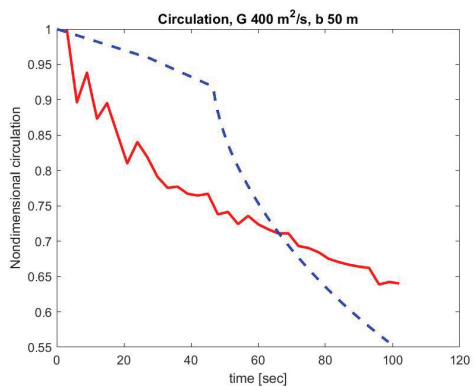
Figure 3.35: $\Gamma = 300 \text{ m}^2/\text{s}$, $b = 40 \text{ m}$. LES simulation (Red), APA 3.8 (Blue).



(a) Vertical Descent.



(b) Circulation Evolution.



(c) Circulation Evolution.

Figure 3.36: $\Gamma = 400 \text{ m}^2/\text{s}, b = 50 \text{ m}$. LES simulation (Red), APA 3.8 (Blue).

4. ROBUST NONLINEAR TRACKING CONTROL FOR UNMANNED AIRCRAFT WITH VIRTUAL CONTROL SURFACES

The Federal Aviation Administration (FAA) is currently faced with myriad operational safety challenges that exist in integrating UAS in the NAS. Specifically, the Integrated Safety Assessment Model (ISAM) requires further development and improvements in order to fully address UAS operations for current and future risk analyses. Motivated by the desire to improve the safety of UAS operating in the NAS, the development of novel UAV flight control technologies is of critical importance.

Specifically, there is a need for control system technologies that are capable of quickly recovering from unpredictable and potentially hazardous operating conditions resulting from phenomena such as airflow disturbances due to upstream wake vortex, wind gusts, or turbulence. Based on these considerations, the focus of the current chapter is on the development of a nonlinear control method, which demonstrates reliable and accurate UAV trajectory regulation in the presence of unmodeled and time-varying operating conditions in addition to uncertainty in the governing UAS dynamic model. Particularly, a robust nonlinear flight control strategy in the presence of the wind gust, as well as the wake vortex disturbance, is presented. The analysis of the robust nonlinear controller in comparison to a linear H_∞ controller for several cases is demonstrated.

Moreover, a robust nonlinear flight control strategy is presented, which utilizes arrays of SJAs embedded in a seamless UAV blended wing-body design (see

Figure 4.1). SJAs can provide enhanced maneuverability for small fixed-wing UAV applications, where the use of heavy, mechanical deflection surfaces is impractical or detrimental. The proposed control design is particularly advantageous in maintaining flight stability in the presence of a high degree of uncertainty and nonlinearity in the UAV operating conditions (e.g., flight conditions inherent in tight urban environments and terminal zones). In addition, the proposed control method is capable of compensating for the parametric uncertainty and nonlinearity inherent in the dynamics of SJA.

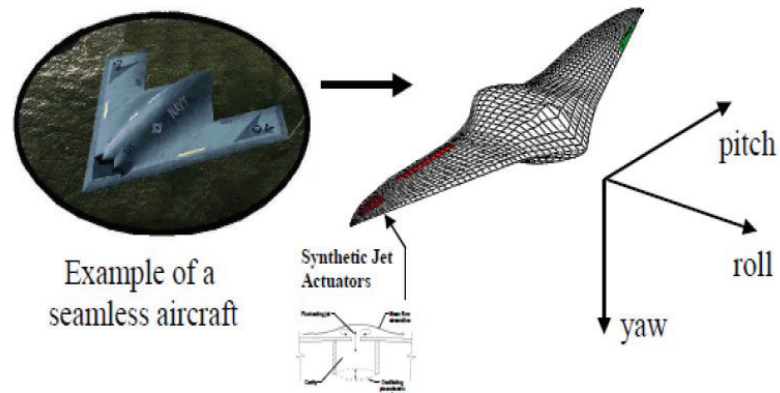


Figure 4.1: Seamless aircraft employing SJAs in a blended wing-body design.

The developed methodology and the conducted studies pave the way to further optimization, testing and validation of the wake/gust interference models including appropriate estimation of uncertainties in aircraft and weather inputs, developing inputs to fault tree analyses within ISAM structure, and eventually employing the developed models for adjusting procedures for UAS operations in the terminal zone within SITAR WVSS module. standard linear control method.

In this chapter, the UAV-wake-vortex interaction, as well as UAV-gust interaction, is considered. Particularly, a robust nonlinear flight control strategy capable of the wake vortex disturbance rejection in different phases of evolution including in-ground and out-of-ground phases is presented. The disturbance is both modeled by applying the low fidelity model of wake vortex pair (Yu, Qu, & Zhang, 2018) for the steady level flight and Monte-Carlo simulations scenario as well as using high fidelity simulations (Large Eddy Simulation (LES)) for the take-off and landing when the wake vortex is in in-ground effect phase. The proposed control design is particularly advantageous in maintaining flight stability in the presence of a high degree of uncertainty and nonlinearity in the UAV operating conditions (e.g., flight conditions inherent in tight urban environments and terminal zones).

4.1 Mathematical Model

This section describes the mathematical model utilized to develop our nonlinear control method. The subsequently provided numerical simulation results are obtained using the mathematical models presented in this section for the UAV, SJA actuator dynamics, and wind gusts. The UAV dynamic model under consideration in this chapter is assumed to contain parametric model uncertainty in addition to unmodeled, time-varying nonlinearities. The aircraft dynamics is

modeled via a quasi-linear state space system as (Tchieu et al., 2008; Nelson, 1998; Deb et al., 2005, 2007, 2008; Mondschein et al., 2011; Singhal et al., 2009):

$$\begin{aligned} \dot{x} &= A(\rho)x + B(\rho)u + f(x, t) \\ y &= C(\rho)x + D(\rho)u \end{aligned} \tag{4.1}$$

where ρ is a measurable exogenous parameter vector, called the scheduling parameter, $x \in \mathbb{R}^n$ are the deviation states, $u \in \mathbb{R}^m$ are the deviation inputs, $y \in \mathbb{R}^p$ are the deviation outputs, and $f(x, t)$ is an unknown nonlinear disturbance. Here, $A(\rho) \in \mathbb{R}^{n \times n}$ represents the system matrix, $B(\rho) \in \mathbb{R}^{n \times m}$ the input matrix, $C(\rho) \in \mathbb{R}^{p \times n}$ the output matrix, and $D(\rho) \in \mathbb{R}^{p \times m}$ the feedthrough matrix. The system is then arranged such that:

$$A(\rho) = A_0 + \sum_{i=1}^k \delta_i A_i \tag{4.2}$$

$$B(\rho) = B_0 + \sum_{i=1}^k \delta_i B_i \tag{4.3}$$

$$C(\rho) = C_0 + \sum_{i=1}^k \delta_i C_i \tag{4.4}$$

$$D(\rho) = D_0 + \sum_{i=1}^k \delta_i D_i \tag{4.5}$$

where $A_0, B_0, C_0,$ and D_0 are the nominal state space matrices. The parametric uncertainty is reflected by $\delta_i \in [-1, 1]$, and the structural knowledge about the uncertainty is contained in the matrices $A_i, B_i, C_i,$ and D_i (Zhou, Doyle, & Glover, 1995). This chapter will focused on the longitudinal control of a small UAV.

The longitudinal dynamics of an aircraft is described by the state vector $x = [u, w, q, \theta, Z_e]^T$, input vector $u = [\delta_e, \delta_\tau]^T$, and output vector $y = [V, \alpha, q, \theta, h, a_x, a_z]^T$. Here, u is the axial velocity, w is the vertical velocity, q is the pitch rate, θ is the pitch angle, and Z_e is the vertical position of the aircraft with respect to the horizon. In addition, δ_e is the elevator deflection, δ_τ is the throttle input, V is the true airspeed, α is the angle of attack, h is the altitude, a_x is the axial acceleration, a_z is the vertical acceleration. The scheduling parameter ρ can be altitude and Mach number and the unknown disturbance $f(x, t)$ could be wind gusts or nonlinearities not captured in the linear model.

The state vector for lateral dynamics is $x = [v, p, r, \phi, \psi]^T$ with input vector $u = [\delta_a, \delta_r]^T$. Where v, p, r, ϕ, ψ is lateral velocity, roll and yaw rates and angles. The input parameters are aileron and rudder deflections. As mentioned above, the control application of this chapter is on small UAVs with synthetic jet actuators (SJA). The action of these actuators can be related to a virtual elevator deflection δ_e such that:

$$\dot{x} = Ax + Bu + f(x, t) \quad (4.6)$$

where $A \in \mathbb{R}^{n \times n}$ represents a constant, uncertain state matrix; and $B \in \mathbb{R}^{n \times m}$ denotes an uncertain input gain matrix. In Equation 4.6, the state vector $x(t) \stackrel{\text{def}}{=} [v(t) \ w(t) \ q(t) \ \theta(t) \ h(t)]$, where the state elements include vertical and horizontal components of velocity $v(t)$ and $w(t)$, pitch rate $q(t)$, pitch angle $\theta(t)$, and altitude $h(t)$ (Natesan, Gu, & Postlethwaite, 2007; Kumar & Jain, 2014). In

4.6, $f(x, t)$ denotes a general, unknown nonlinear disturbance. For example, $f(x, t)$ could represent exogenous disturbances (e.g., due to wind gusts) or nonlinearities not captured in the linearized dynamic model, for example. Also in 4.6, the control input term $u(t) \stackrel{\text{def}}{=} [\delta_e(t) \quad \delta_t(t)]^T \in \mathbb{R}^m$, where $\delta_e(t) \in \mathbb{R}^{m-1}$ denotes the elevator control deflection angle; and $\delta_t(t) \in \mathbb{R}$ is the throttle input. In our SJA-based UAV control application, the (virtual) elevator deflection angle input $\delta_e(t)$ is generated by an array consisting of $m - 1$ SJAs. Thus, the virtual elevator deflection angle input can be expressed as:

$$\delta_e(t) \stackrel{\text{def}}{=} [u_1(t) \quad u_2(t) \quad \dots \quad u_{m-1}(t)]^T \quad (4.7)$$

where $u_i(t) \in \mathbb{R}, i = 1, 2, \dots, m - 1$ represents the virtual surface deflection due to the i^{th} array of SJAs. Based on empirical studies, the SJA dynamics can be modeled as (Deb et al., 2005, 2007, 2008, 2006)

$$u_i(t) = \theta_{2i}^* - \frac{\theta_{1i}^*}{V_i(t)}, \quad i = 1, 2, \dots, m - 1 \quad (4.8)$$

where $V_i(t) = A_{ppi}^2(t) \in \mathbb{R}$ denotes the peak-to-peak voltage acting on the i^{th} SJA array; and $\theta_{1i}^*, \theta_{2i}^* \in \mathbb{R}$ are uncertain constant physical parameters. One of the control design challenges is that the control terms in $u_i(t)$ depend nonlinearly on the voltage signal $V_i(t)$ and contain parametric uncertainty due to θ_{1i}^* and θ_{2i}^* . This challenge will be mitigated using a robust nonlinear control technique.

4.2 Nonlinear Robust Control

4.2.1 Control Objective

The control objective is divided into two parts: one for the longitudinal dynamics and one for the lateral dynamics. The goal is to force the UAV altitude and pitch rate (i.e., $h(t)$ and $q(t)$) to track a given desired constant value (longitudinal) as well as roll and yaw rates (i.e., r and p) (lateral) in spite of model uncertainty and external disturbances.

To quantify the control objective, the trajectory regulation error $e(t) \in \mathbb{R}$ and auxiliary regulation error $r(t) \stackrel{\text{def}}{=} \begin{bmatrix} r_q(t) & r_h(t) \end{bmatrix}^T \in \mathbb{R}^2$ are defined as:

$$e(t) = \begin{bmatrix} h(t) \\ \theta(t) \end{bmatrix} \quad (4.9)$$

$$r(t) = \begin{bmatrix} r_h(t) \\ r_q(t) \end{bmatrix} = \begin{bmatrix} \dot{h}(t) + \alpha_1 h(t) \\ q(t) + \alpha_2 \theta(t) \end{bmatrix} \quad (4.10)$$

In case of lateral motion, the auxiliary regulation error $r(t) \stackrel{\text{def}}{=} \begin{bmatrix} r_p(t) & r_r(t) \end{bmatrix}^T \in \mathbb{R}^2$ and roll/yaw regulation error are as follows:

$$e(t) = \begin{bmatrix} \phi(t) \\ \psi(t) \end{bmatrix} \quad (4.11)$$

$$r(t) = \begin{bmatrix} r_p(t) \\ r_r(t) \end{bmatrix} = \begin{bmatrix} \dot{\phi}(t) + \alpha_1 \phi(t) \\ \dot{\psi}(t) + \alpha_2 \psi(t) \end{bmatrix} \quad (4.12)$$

In equations (4.10,4.12) $\alpha_1, \alpha_2 \in \mathbb{R}$ denote positive, constant control gains.

Thus, the trajectory regulation control objective can be stated mathematically as $\|e(t)\| \rightarrow 0$, where $\|\cdot\|$ denotes the standard Euclidean norm of the vector argument. Note that, based on the auxiliary regulation error definitions in equations (4.10 and 4.12), $\|r(t)\| \rightarrow 0 \Rightarrow \|e(t)\| \rightarrow 0$.

Remark 1: The regulation error and auxiliary errors defined in Equations (4.9,4.11) and (4.10,4.12) are a key aspect of the contribution presented here. The definitions of the auxiliary regulation errors enable us to recast the dynamic model in Equation (4.1) in a form that is amenable to altitude/pitch angle and roll/yaw angle regulation control. Indeed, it can be seen that differentiation of $r(t)$ produces a set of equations that render the altitude and pitch angle states ($h(t)$ and $\theta(t)$) and roll/yaw angles (ϕ, ψ) fully controllable through the elevator deflection and throttle inputs $\delta_e(t), \delta_t(t)$ and $\delta_a(t), \delta_r(t)$. Thus, the auxiliary error terms $r_h(t), r_q(t), r_r(t), r_p(t)$ can be viewed as sliding surfaces, which enables us to prove our altitude and pitch angle regulation results.

4.2.2 Robust Controller Development

A contribution of the control method presented in this chapter is the capability of the proposed control strategy to asymptotically compensate for the control input nonlinearity and parametric uncertainty in the SJA dynamic model. To achieve

this, a robust inverse structure for $V_i(t)$, $i = 1, \dots, m - 1$ will be utilized, which contains constant feedforward best-guess estimates of the uncertain parameters θ_{1i}^* and θ_{2i}^* . The robust inverse that compensates for the uncertain jet array nonlinearities are expressed as (MacKunis et al., 2013):

$$V_i(t) = \frac{\hat{\theta}_{1i}}{\hat{\theta}_{2i} - u_{di}(t)}, \quad i = 1, \dots, m - 1 \quad (4.13)$$

where $\hat{\theta}_{1i}^*, \hat{\theta}_{2i}^* \in \mathbb{R}^+$ are constant feedforward estimates of θ_{1i}^* and θ_{2i}^* , respectively; and $u_{di} \in \mathbb{R}$, $i = 1, \dots, m - 1$ are subsequently defined auxiliary control signals. Note that the robust-inverse structure in (4.13) is only required for the virtual elevator deflection angle control inputs in $\delta_e(t)$. The schematic block diagram of the simulink model is presented in the Figure 4.19.

Remark 2: The controller design presented in this chapter is valid for systems in the form of Equations 4.1, where the total number of control inputs (i.e., the throttle and the SJA arrays) is greater than or equal to the number of states to be controlled (i.e., the $m \geq n$ case). For the case where $m > n$, the following control design can easily be modified using the matrix pseudoinverse definition, for example. The underactuated case where $m < n$ would require a specialized design methodology and is not addressed in the current result. The following control design and subsequent simulation results are based on the case where $m = n = 2$, without loss of generality. In order to achieve asymptotic convergence of θ , h and ϕ , ψ to zero with a given convergence rate in the presence of a bounded disturbance

(i.e. wake vortex or wind gust), we have to drive the auxiliary regulation error r to zero in finite time.

Taking into account the original dynamic model, and the auxiliary regulation error r , the auxiliary control term u is designed as:

$$\begin{bmatrix} u \end{bmatrix} = \begin{bmatrix} \hat{\Omega}^{-1} \end{bmatrix} \begin{bmatrix} k_1 r_{h,r} \\ k_2 r_{q,p} \end{bmatrix} + \begin{bmatrix} \beta_1 \tanh(r_{h,r}) \\ \beta_2 \tanh(r_{q,p}) \end{bmatrix} \quad (4.14)$$

where $\hat{\Omega}$ denotes a constant auxiliary matrix, and $[\]^{-1}$ denotes the inverse of a matrix. The feedback control gains (i.e., amplifiers) $k_1, k_2, \beta_1, \beta_2$ can be tuned to adjust the closed loop regulation response to achieve the desired system performance (e.g., to achieve a faster response time).

Note that the continuous $\tanh()$ switching term in Equation 4.14 is used in the subsequent simulation implementation, but the discontinuous $\text{signum}()$ function is required to prove asymptotic disturbance rejection as shown in (Kazarin et al., 2017). The feedback control gains (i.e., amplifiers) $\alpha_1, \alpha_2, \beta_1, \beta_2, k_1, k_2$ can be tuned to adjust the closed loop trajectory regulation response to achieve the desired system performance (e.g., to achieve a faster response time).

4.2.3 Observer Design

In 4.1 the explicitly defined output y can be denoted as sufficiently differentiable vector function $h(x)$. To facilitate the subsequent observer design and analysis, a vector $H(x) \in \mathbb{R}^n$ of output derivatives is defined as:

$$H(x) = [h_1(x), h_2(x), \dots, h_n(x)]^T = [h(x)L_f h(x) \dots L_f^{n-1} h(x)]^T \quad (4.15)$$

where $L_f^i h(x)$ denotes the i -th Lie derivative of the output function $h(x)$ along the direction of the vector field Ax .

An observer that estimates the full state $x(t)$ of the system in 4.1 using only measurements of $y(t)$ can be designed as (Drakunov, 1992):

$$\dot{\hat{x}} = A\hat{x} + M \operatorname{sgn}[V(t) - H(\hat{x})] + Bu \quad (4.16)$$

In 4.16, $V(t) = [v_1(t), \dots, v_n(t)]^T$ is defined via the recursive form $v_1(t) = y(t)$, $v_{i+1}(t) = \hat{m}_i \operatorname{sgn}[v_i(t) - h_i(\hat{x}(t))]$ for $i = 1, \dots, n-1$.

Also in 4.16, $M(\hat{x}) \in \mathbb{R}^{n \times n}$ denotes a diagonal matrix with positive elements defined as:

$$M(\hat{x}) = \operatorname{diag}[m_1(\hat{x}), \dots, m_n(\hat{x})] \quad (4.17)$$

where $m_i(\hat{x}) \in \mathbb{R}$, $\hat{x} \in \mathbb{R}$ $i = 1, \dots, n$.

Similar to the design in (Caraballo et al., 2007), it can be shown that the observer design in 4.16 achieves finite-time estimation of the state $x(t)$. Specifically,

it can be shown that, through judicious selection of the diagonal matrix $M(\hat{x}), \hat{x}(t) = x(t)$ for any $t \geq t_1$. By including the additional term in the observer design, it follows that, for $t \geq t_1$, the system converges to the sliding manifold $\sigma = V(t) - H(\hat{x})$, and the observer equation 4.16 exactly estimates the state $x(t)$ of the flow dynamic system in 4.1.

4.3 Numerical simulation

4.3.1 Linear, Parameter-Varying Model

For further comparison of linear vs nonlinear control designs, here will be used a linear, parameter-varying (LPV) model based on a small fixed-wing UAV. The UAV selected for numerical simulations is the Ultrastick 120 for which the aerodynamics and flight dynamics has been widely studied (Freeman, 2014; Dorobantu et al., 2011). Figure 4.2 shows a picture of the UAV airframe. The LPV model is created by linearizing the nonlinear equations of motion about a set of equilibrium points. Here, the LPV model of the Ultrastick 120 holds a constant altitude and varying airspeed.



Figure 4.2: Ultra Stick 120. Source: UAV Laboratories, University of Minnesota.

The Ultrastick 120 LPV model is then generated by obtaining a set of equilibrium points holding a constant altitude of 100 m and varying airspeed between 15-29 m/s. These equilibrium points are shown in Figure 4.3 where airspeed $V = 23$ m/s is chosen as the nominal flight condition. Figure 4.4 shows the change of system dynamics in the presence of parametric uncertainty in comparison to the nominal flight condition. Robust nonlinear and linear controllers for such UAV designed, with performance analysis presented below.

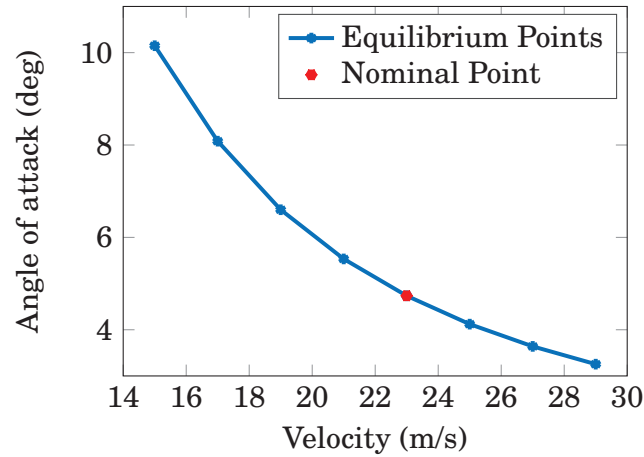


Figure 4.3: Varying parameter trajectory: set of equilibrium points for LPV model.

4.3.2 H_∞ Linear Controller

The interconnection used to synthesize the linear controllers is depicted in Fig. 4.5. Here, e represents the control objective outputs, i.e. altitude h and pitch angle θ . The controller K_∞ takes the pitch rate q , pitch angle θ , altitude h , and vertical acceleration a_z as feedback measurements. The controller minimizes the robust performance level from actuation disturbances, d , and wind gusts

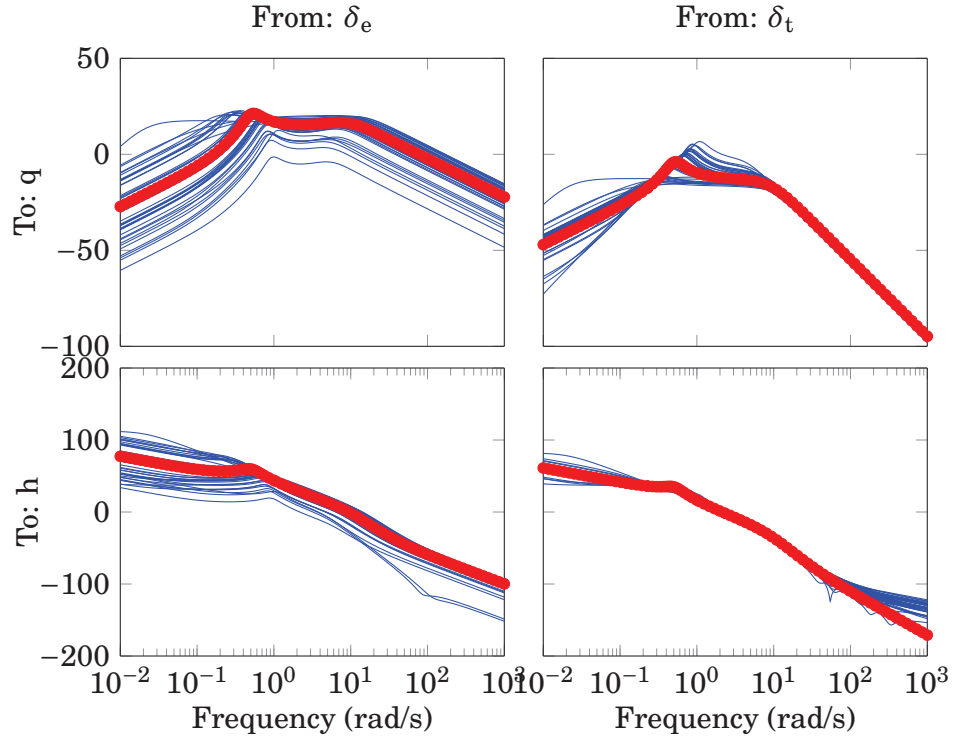


Figure 4.4: Elevator and throttle deflection frequency response to altitude and pitch rate for nominal system (red) and uncertain system (blue).

disturbances w to the control objectives, e , while maximizing the robustness to model uncertain.

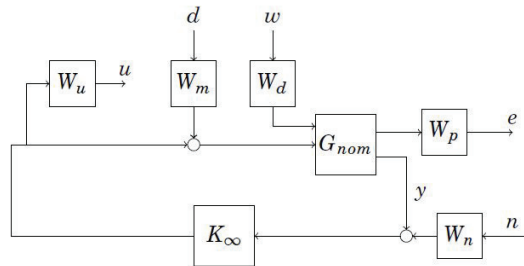


Figure 4.5: Control interconnection for linear design.

Constant weights, W_m , are used to model the disturbances to each control input. This weight is selected as $W_m = 0.4$ for all control inputs. In addition, a multiplicative input weight is included to avoid destabilizing unmodeled frequency

modes outside the control bandwidth. The uncertainty model weight is described by $W_u = 1.22(s + 0.48)/(s + 0.224)$.

On the other hand, the disturbance rejection of critical variables is enforced by a constant performance weight W_p . A constant gain attenuation of $W_p = 1$ is assigned to each control objective in order to ensure damping. Similarly, wind gust disturbances are attenuated with a constant weight $W_d = 1$ and noise is accounted with the constant weight $W_n = 0.05$ for each measurement. Once all the weights are defined, the next step is to design H_∞ controllers such that the system gain from $[d, w]^T$ to $[e, u]^T$ is less than 1. The Robust Control Toolbox from MATLAB is used to design the H_∞ controller with a system gain of $\gamma = 0.99$. Hence, the controller designed achieves the control objectives specified in the control interconnection.

4.3.3 Simulation

Wind Gust Model

The performance of the nonlinear robust controller is tested using the Matlab/Simulink software. The simulation is based on state space systems describing each particular equilibrium point of LPV model described above.

Similar to (Golubev et al., 2016) the aircraft longitudinal performance is evaluated for a nonlinear disturbance in the form of a vertical wind gust described as (Part, 2002),

$$f(x, t) = w_g \frac{1}{V_0} \left\{ \frac{U_{ds}}{2} \left[1 - \cos\left(\frac{\pi s}{H}\right) \right] \right\} \quad (4.18)$$

where H denotes the distance (between 35 feet and 350 feet) along the aircraft flight path for the gust to reach its peak velocity, V_0 is the forward velocity of the aircraft when it enters the gust, $s \in [0, 2H]$ represents the distance penetrated into the gust (i.e., $s = \int_{t_1}^{t_2} V(t)dt$, where $V(t)$ is the forward velocity element of the state vector x), and U_{ds} is the design gust velocity (Part, 2002). The vector $w_g \in \mathbb{R}^5$ represents the relative impact of the gust on each state of the system. This FAR formulation is intended to be used to evaluate both vertical and lateral gust loads, so a similar representation can be developed for the lateral dynamics. This simulation uses the parameters $H = 15.24m$, and V_0 equal to the speed in the current trim state, (cruise velocity). Since the state vector in this case is defined as $x(t) \stackrel{\text{def}}{=} [v(t) \quad w(t) \quad q(t) \quad \theta(t) \quad h(t)]$, the constant gain parameters of the simulated model were modified slightly from (4.18). The remainder of the additive disturbances in $f(x, t)$ represents nonlinearities not captured in the linearized state space model (e.g., due to small angle assumptions).

The SJA actuator dynamic model uses the following well-accepted, empirically determined values for the constant parameters (Deb et al., 2005, 2007, 2008) θ_{1i}^* and θ_{2i}^* :

$$\theta_{1i}^* = 33.33, \quad \theta_{2i}^* = 15 \quad (4.19)$$

Remark 3: The values used in the simulation for the parameters θ_1^* and θ_2^* are used to generate the SJA dynamic model only. The parameters are assumed to be uncertain and are not used in the feedback control law. Our preliminary

results show that the robust nonlinear control method presented here is capable of achieving accurate tracking control of a SJA-based UAV system when the constant estimates $\hat{\theta}_1$ and $\hat{\theta}_2$ differ by as much as 1 % from the actual values θ_1^* and θ_2^* .

4.4 Wake Vortex Modeling

In order to determine the loads induced on the aircraft flying through the wake vortex, one need to model the flow field induced by the vortex pair as well as the forces and moments acting on the airplane while interaction. Knowing the characteristics of wake the generator aircraft with elliptically loaded wings, one can obtain the vortex flow field created by the vortex pair. The vortex pair in this study is modeled by Burnham-Hallock model (Burnham & Hallock, 1982) where tangential velocities induced by the wake are calculated with a constant core radius,

$$V_t = \frac{\Gamma_0}{2\pi} \frac{r}{r_c^2 + r^2} \quad (4.20)$$

The evolution of the wake vortex was simulated by the WVSS in the out-of-ground zone as well as near the ground, where the interaction of the wake vortex and surface boundary layer occurs. The forces and moments for both zones are calculated using the strip theory. Far from the ground, the wake vortex is modeled by using the low fidelity model, where the vortices are two-dimensional and the velocity field is calculated directly from Burnham-Hallock model and are stationary during the encounter. Also, Monte-Carlo simulations for this flight regime are performed. The full procedure of Monte-Carlo approach is discussed in our previous

work (Kazarin & Golubev, 2017a). Hence, the steady level flight phase is modeled in the out-of-ground zone.

In the vicinity of the ground, the behavior of the vortex is based on the data from the 3D LES simulations performed in OpenFOAM software and described in detail in our studies devoted to the wake vortex propagation near different types of ground surfaces (Kazarin & Golubev, 2017b, 2018). Then, the velocity fields are extracted from the 3D simulation and are used for the calculation of forces and moments acting on the airplane. When interacting with each other and with the surface boundary layer, the vortex pair generates a turbulent velocity field which can significantly affect the aircraft. The simulation close to the ground surface models take-off and landing phase of the flight.

4.5 Results

This section presents the analysis of the robust nonlinear controllers in comparison to a linear H_{inf} controller described above and also in (Dorobantu, Murch, Mettler, & Balas, 2013) with the same performance objectives. Results for several equilibrium points as well as wind gust amplitudes are presented in the (Kazarin et al., 2017). In this work, the results for one equilibrium points are shown. The aim of the regulation is to drive the altitude and pitch rate deviation to zero. The control gains selected for the nonlinear control law in the simulation are (see Equation (4.10)):

$$k_1 = 6, \quad k_2 = 10, \quad \alpha_1 = 50, \quad \alpha_2 = 90 \quad (4.21)$$

The detailed time evolution of the flight trajectories during closed-loop linear and nonlinear controller, the operation is performed for two trim conditions (23 m/s and 21 m/s) and equal gust amplitudes of 17 m/s. The pitch rate and pitch angle deviations for 21 m/s equilibrium point are lower in case of the nonlinear controller. However, the altitude deviation is slightly lower for linear control law. For nominal trim point, the altitude deviation remains almost the same for two controllers, but pitch rate and pitch angle disturbances turn out to be much lower for the nonlinear controller. For nominal equilibrium point, nonlinear controller significantly outperforms the linear one in terms of elevator deflection, however, throttle power required by the linear controller is much lower. When trim condition changes from nominal, the nonlinear controller still works better in terms of pitch rate and pitch angle deviations. The control power for elevator input is still small for the nonlinear case and throttle inputs are almost the same.

Figure 4.24 reflects the performance of two controllers under the impact of stronger gust. It is clear that the maximum altitude deviation is smaller for the linear controller. Pitch rate and pitch angle curves are much more disturbed in the linear case. However, the elevator deflection for nonlinear control law (Figure 4.25) is lower by an order of magnitude.

The reaction of the controllers to SJA uncertainty was also tested and is shown in Figures 4.27 and 4.26. The control power needed to suppress the gust in the presence of SJA uncertainty is significant. As for the state convergence, the linear controller is still stable but the offset from the zero is about 1.5 for the pitch angle

θ . The nonlinear control law, in this case, gives a constant offset of about 0.01 degree.

4.5.1 Interaction with Wake Vortex. Take-off and Landing Phases

The velocity fields are extracted from the LES simulation of the wake vortex in the ground vicinity for three cases: highly turbulent case, take-off, and landing cases. The corresponding vorticity fields are shown in Figure 4.6. The red dashed line displays the path along which the aircraft was swept through the domain.

Figures 4.7 - 4.15 show the result of the wake-vortex-aircraft interaction for each case.

The highly turbulent case reflects the turbulent nature of the real wake vortex. The parameters of the generator aircraft and flight regime determine the following characteristics of the wake vortex:

- Circulation $\Gamma_0 = 600m^2/s$
- Vortex core radius $r_c = 1.8m$
- Separation distance $30m$
- Current time $t = 132s$

The secondary vortices are being destroyed due to the interaction with the primary vortices. The destruction is accompanied by the generation of the turbulence with the opposite vorticity which triggers the breaking up of the vortex pair and formation of the smaller vortices. The similar process takes place when the vortex pair interacts with the turbulent atmosphere. The bigger the turbulence

intensity the more pronounced the decay is. This case demonstrates the behavior of the aircraft in the highly turbulent atmosphere provided with the interaction with the wake vortex.

Figure 4.7 and 4.8a demonstrate the response of the aircraft to the disturbance created by the highly turbulent velocity fields at $H = 54m$ from the ground surface and expressed in terms of roll rate disturbance and horizontal velocity disturbance (Figure 4.8b). For roll ϕ and yaw, ψ angles the nonlinear controller suppresses the deviation faster than the linear one. Roll rate p and yaw rate reactions are similar for both controllers in terms of amplitude and convergence rate. The horizontal velocity v oscillations tend to be bigger for the nonlinear controller. The rudder and ailerons' deflections (Figure 4.9) are also bigger in case of the nonlinear controller. In general, the highly turbulent case is characterized by sharp peaks in each state which correspond to intense oscillations in the velocity field and in forces and moments acting on the aircraft as a result.

The landing case is shown in Figure 4.6b and is characterized by fully formed secondary vortices revolving over the primary ones. The trajectory of the follower airplane crosses both of them at the $H = 37m$ from the ground. In this case, the nonlinear controller completely outperforms the linear one: the maximum amplitude of the states' deviation is lower and convergence time is shorter (Figures 4.10 and 4.11a). However, this advantage is reached at the expense of energy spent on the surface deflection (Figure 4.12). The wake vortex is characterized by:

- Circulation $\Gamma_0 = 300m^2/s$

- Vortex core radius $r_c = 1.8m$
- Separation distance $30m$
- Current time $t = 60s$

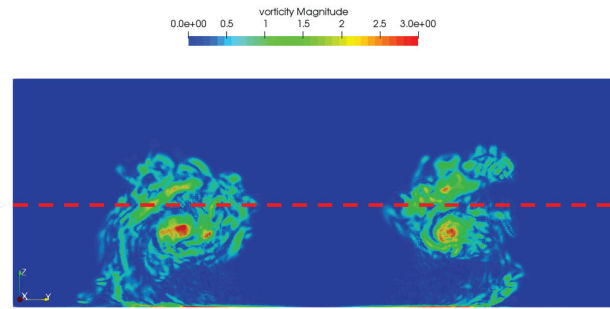
In the take-off case, the distance to the ground for the follower aircraft is $13.1m$, the secondary vortices formed due to the wake vortex interaction with the ground surface boundary layer cross the aircraft's trajectory. The characteristics of the vortex pair are as follows:

- Circulation $\Gamma_0 = 300m^2/s$
- Vortex core radius $r_c = 1.8m$
- Separation distance $30m$
- Current time $t = 42s$

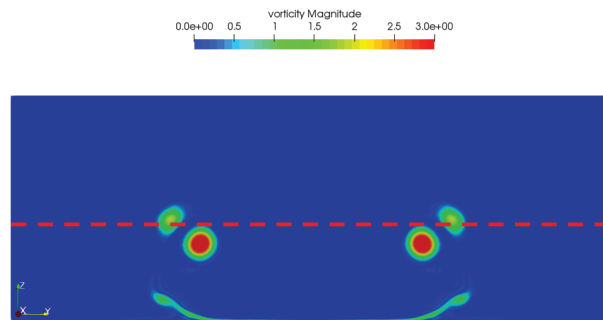
The convergence rate for roll angle ϕ , yaw angle ψ and roll rate p (Figure 4.13 and 4.14a) is higher in the nonlinear case. The maximum deviation for all the states is higher for the H_∞ controller which makes the nonlinear controller more efficient. The ailerons deviations are shown in Figure 4.15 are almost the same for both controllers, however, the rudder deflection is bigger in case of the nonlinear controller.

4.5.2 Interaction with Wake Vortex. Steady Level Flight Phase

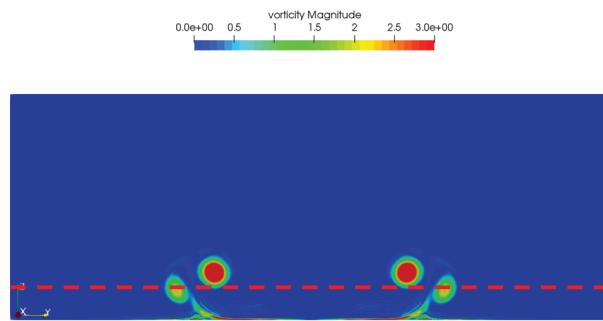
Two sets of Monte Carlo simulations were done to model the steady level flight of the aircraft in the presence of wake vortex. The first set was performed to form



(a)



(b)



(c)

Figure 4.6: (a) Highly turbulent case. $\Gamma_0 = 600m^2/s, t = 132s, h = 54.5m$ (b) Landing case. $\Gamma_0 = 300m^2/s, t = 60s, h = 37m$ (c) Take-off case. $\Gamma_0 = 300m^2/s, t = 42s, h = 13m$.

the cone of uncertainty for the wake vortex itself. The second set corresponds to the simulations for the control system and is performed for the several trim points.

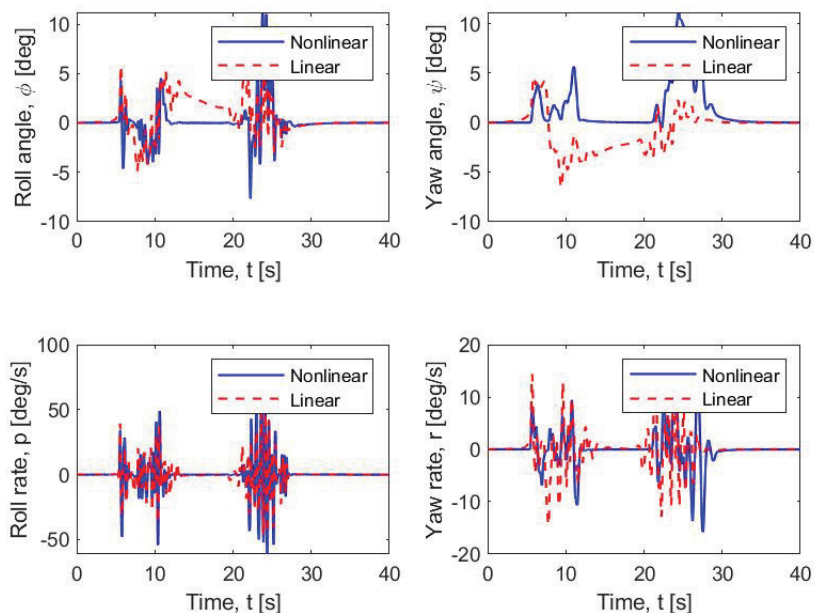


Figure 4.7: States deviations for nominal trim point, highly turbulent case.

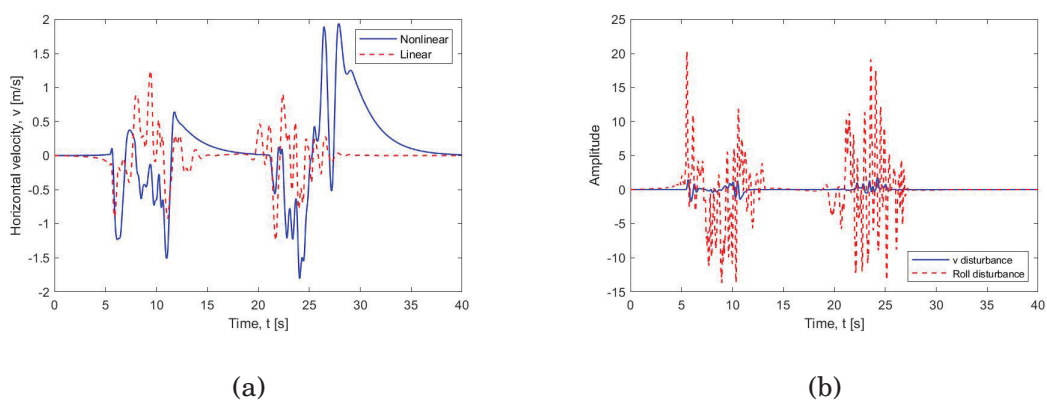
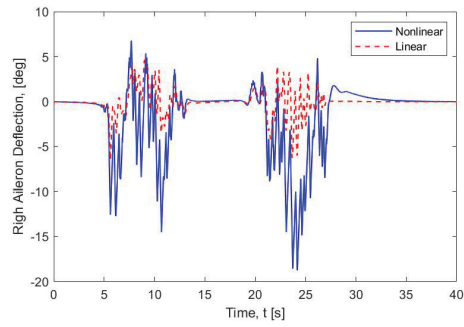


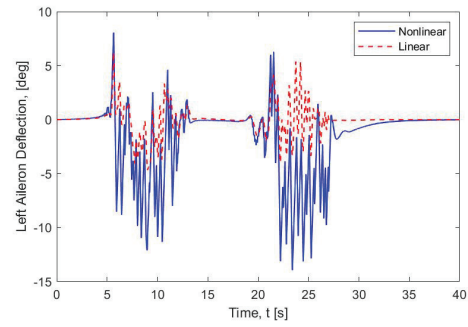
Figure 4.8: (a) Horizontal velocity and (b) Disturbance, highly turbulent case.

The Nominal Trim Point Simulations

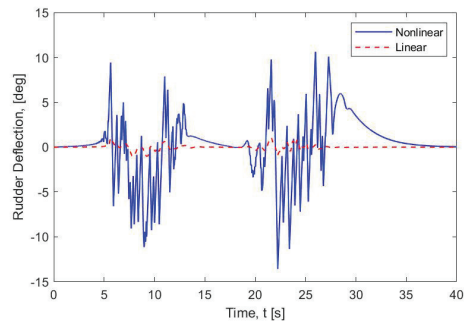
The Monte Carlo simulations for wake vortex pair were performed based on the real data case form Memphis'95 wake vortex data set. The approach is based on perturbing the initial wake vortex conditions (b_0, V_0, z_0) in the deterministic



(a)



(b)



(c)

Figure 4.9: Deflection surfaces deviations for (a)left aileron (b) right aileron and (c) rudder, highly turbulent case.

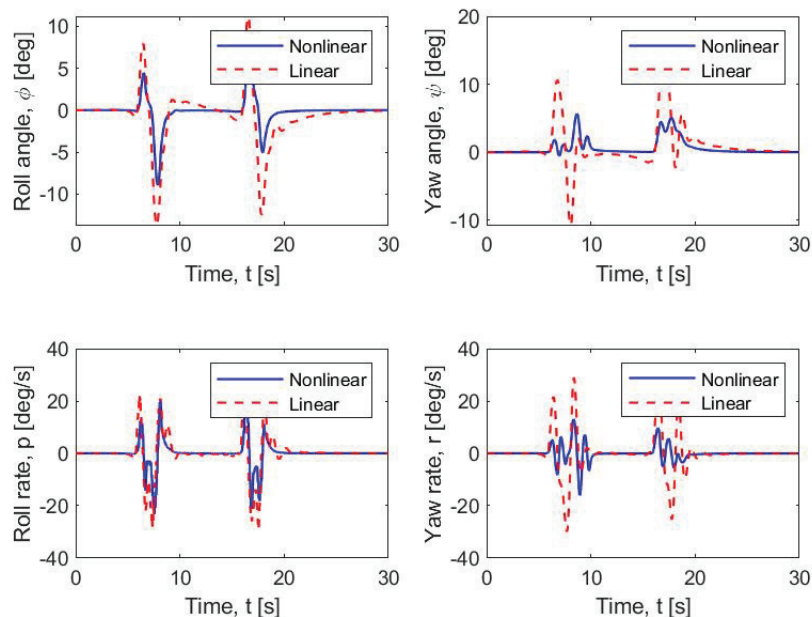


Figure 4.10: States deviations for nominal trim point, landing case.

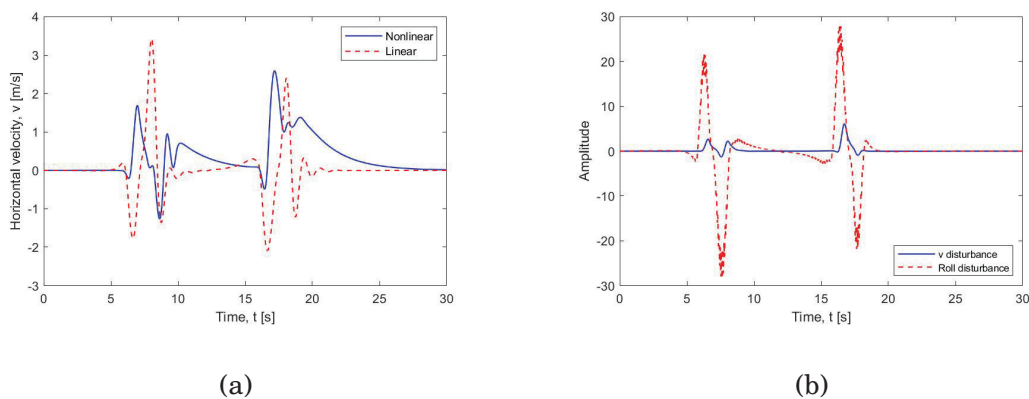
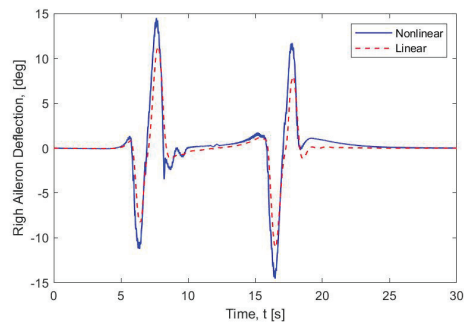
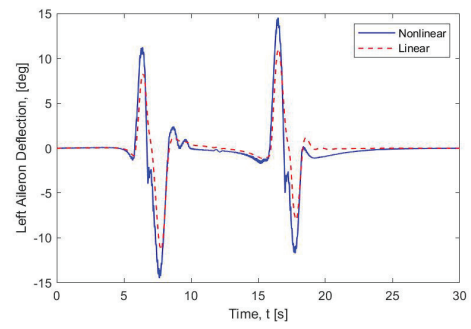


Figure 4.11: (a) Horizontal velocity and (b) Disturbance, landing case.

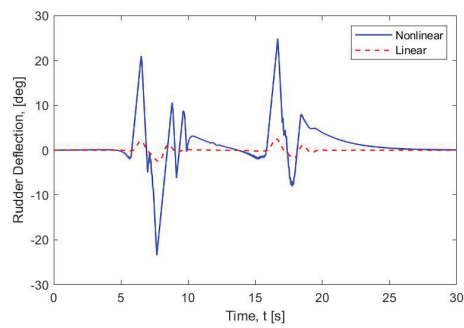
model and generating profiles of the ambient parameters (such as the EDR and potential temperature profiles) using the probability density functions (PDFs). The PDFs are obtained by applying the maximum likelihood estimation method to density histograms corresponding to a particular data set. The vertical profiles



(a)



(b)



(c)

Figure 4.12: Deflection surfaces deviations for (a) left aileron (b) right aileron and (c) rudder, landing case.

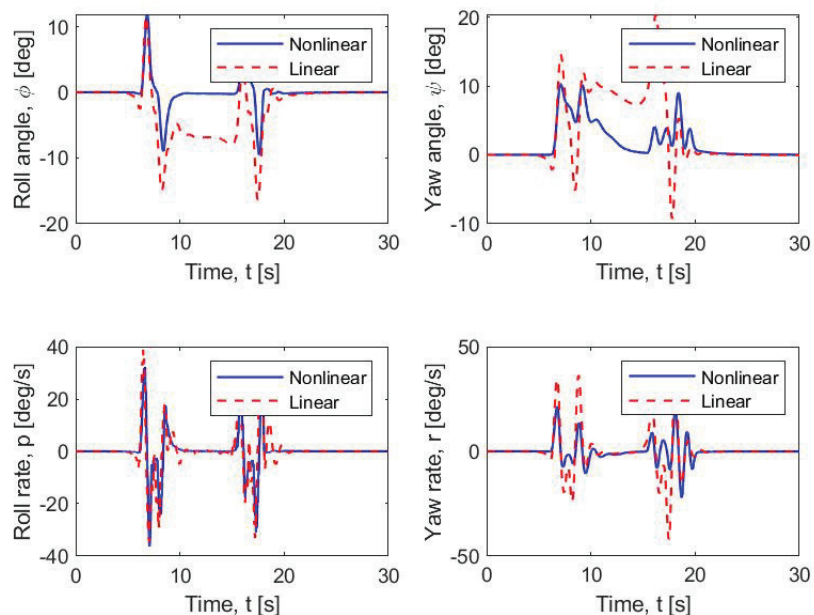


Figure 4.13: States deviations for nominal trim point, take-off case.

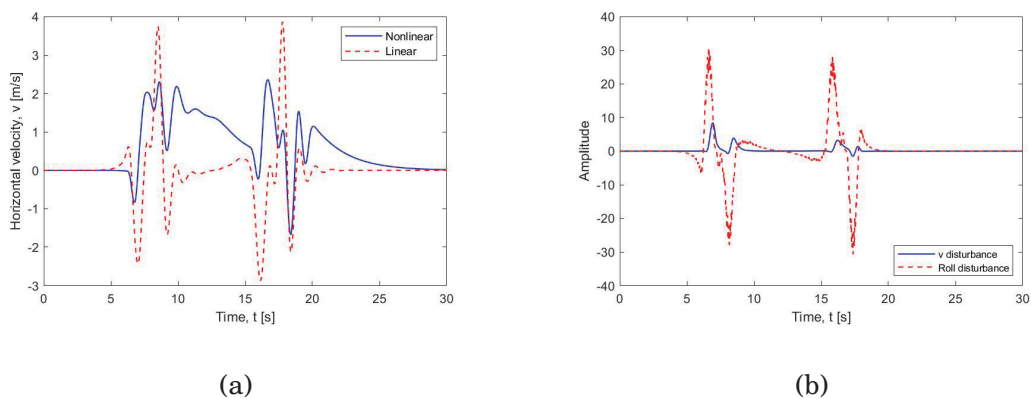
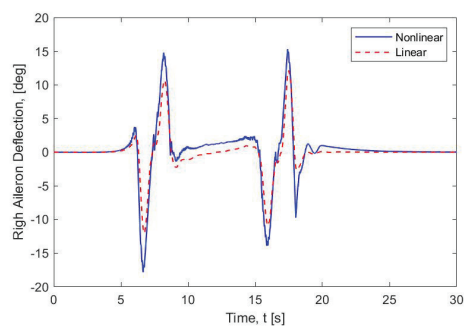
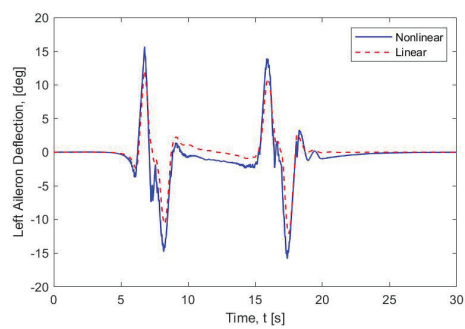


Figure 4.14: (a) Horizontal velocity and (b) Disturbance, take-off case.

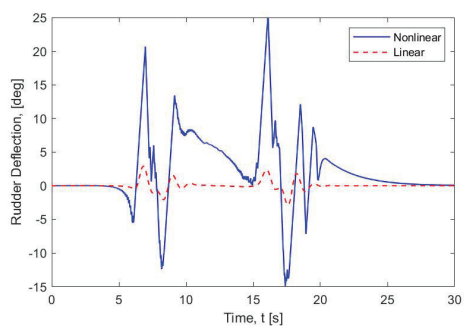
are truncated at the heights of the vortex generation and the mean values are calculated from the zero height to that value. 400 perturbations for vertical profiles were generated using PDFs and used as input parameters along with other parametric perturbations. More details of the method can be found in our previous



(a)



(b)



(c)

Figure 4.15: Deviations for (a) left aileron (b) right aileron and (c) rudder, take-off case.

work (Kazarin et al., 2016). The characteristics of the generator aircraft (B-722) are:

- Circulation $\Gamma_0 = 262m^2/s$
- Span $b = 32.9 m$
- Velocity $V = 77.8 m/s$

The distance to the generator's aircraft path line as well as 400 wake vortex realizations were used as an input to the linear and nonlinear control system. The Vertical position of the follower aircraft was fixed at $Z = 175 m$. The separation distance between the vortices in vortex pair, generator aircraft's weight as well as the vertical distance to the generator aircraft's flight path are the input parameters for controllers' Monte Carlo simulations. Figure 4.16 shows the nondimensionalized circulation and vertical coordinate of the vortex pair obtained in the first set of simulations which forms the cone of uncertainty in the real wake vortex. Several distances to the generator aircraft are considered. The response of the follower aircraft at the distances of $5.46 NM$, $4.16 NM$ and $2.34 NM$ which correspond to $\bar{t} = 5$, $\bar{t} = 3.84$ and $\bar{t} = 2.14$ is considered.

Figure 4.16 demonstrates the cone of the uncertainty of the wake vortex in terms of vertical coordinate and its strength. Blue dashed lines show the cut which corresponds to the moment of time considered. The plots of the states for each Monte Carlo simulation ($\bar{t} = 5$) are shown in the Figure 4.17. The average Root Mean Square Error (RMSE) and Average Maximum Deviations (AMD)

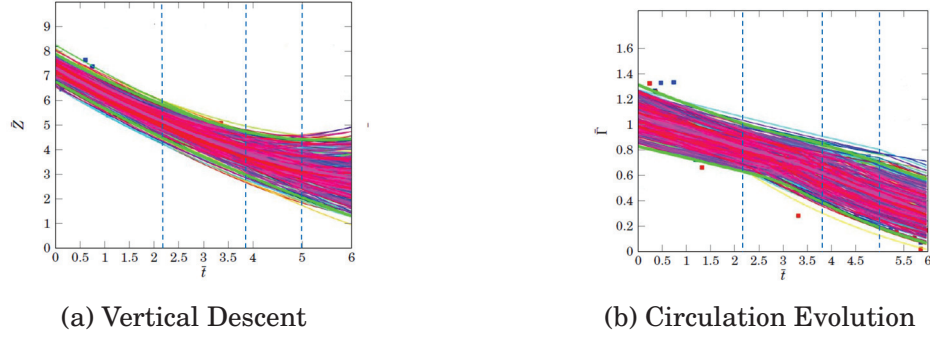


Figure 4.16: Wake vortex evolution results based on 400 Monte-Carlo simulations. The simulation is performed for $\bar{t} = 5$ (Blue dashed line).

of deflections surfaces metrics are chosen to demonstrate the performance of the controller. The values of the average RMSE and AMD for each state are summarizes in Tables 4.1, 4.2 and 4.3. The RMSE for all the states shows that the nonlinear controller is more effective than the linear one in terms of states' deviations. However, the nonlinear controller uses the rudder more actively and spends more energy on it as a result. Also, From the comparison of the RMSE values, one can see that the nonlinear controller works more effective than the linear one.

Table 4.1: Average states' RMSE and Maximum Deviations of Deflection Surfaces over 400 Monte Carlo simulations. $\bar{t} = 5$

Controller type	$\Delta\phi, \text{deg}$	$\Delta\psi, \text{deg}$	$\Delta p, \text{deg/s}$	$\Delta r, \text{deg/s}$	$\Delta v, \text{m/s}$	ΔA_L	ΔA_R	ΔR
<i>Nonlinear</i> _{ARMSE}	1.22	0.78	3.46	1.16	0.13	0.64	0.63	0.93
<i>Linear</i> _{ARMSE}	1.75	1.33	4.31	2.05	0.2	0.71	0.7	0.22
<i>Nonlinear</i> _{AMD}	6.52	3.5	23.53	6.51	0.5	2.93	2.97	4.06
<i>Linear</i> _{AMD}	7.83	5.69	27.2	9.81	1.03	3.39	3.27	1.22

Table 4.2: Average states' RMSE and Maximum Deviations of Deflection Surfaces over 400 Monte Carlo simulations. $\bar{t} = 3.84$

Controller type	$\Delta\phi, \text{deg}$	$\Delta\psi, \text{deg}$	$\Delta p, \text{deg/s}$	$\Delta r, \text{deg/s}$	$\Delta v, \text{m/s}$	ΔA_L	ΔA_R	ΔRr
<i>Nonlinear</i>	2.34	1.44	6.54	2.06	0.27	1.09	1.08	1.64
<i>Linear</i>	3.26	2.43	7.93	3.75	0.38	1.23	1.26	0.39
<i>Nonlinear</i> _{AMD}	12.53	5.92	45.49	10.93	1.02	4.88	5.04	6.96
<i>Linear</i> _{AMD}	14.66	9.94	51.08	17.05	2	5.7	5.58	2.09

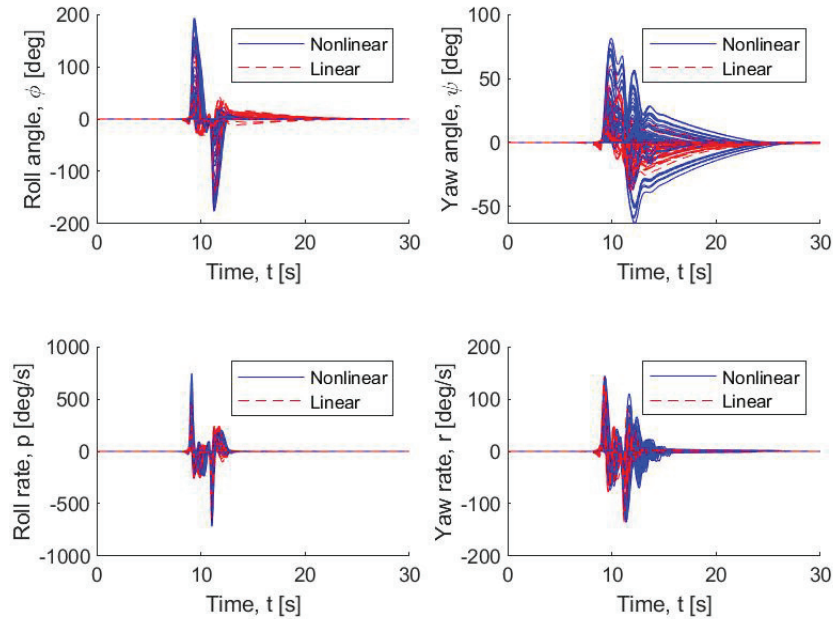


Figure 4.17: States deviations (nominal trim point, MC simulations).

Table 4.3: Average states' RMSE and Maximum Deviations of Deflection Surfaces over 400 Monte Carlo simulations. $\bar{t} = 2.14$

Controller type	$\Delta\phi, \text{deg}$	$\Delta\psi, \text{deg}$	$\Delta p, \text{deg/s}$	$\Delta r, \text{deg/s}$	$\Delta v, \text{m/s}$	ΔA_L	ΔA_R	ΔR
<i>Nonlinear</i> _{ARMSE}	7.71	5.1	17.72	6.5	0.76	2.52	2.22	3.42
<i>Linear</i> _{ARMSE}	9.44	7.21	19.47	9.76	0.9	2.54	2.46	0.94
<i>Nonlinear</i> _{AMD}	34.6	20.1	122.6	32.7	3.15	9.39	9.25	12.34
<i>Linear</i> _{AMD}	36.7	29.2	129.7	44.3	4.8	10.6	10.13	4.58

4.5.3 The Simulations with Parametric Uncertainty

The LPV simulation is performed for several trim points (equilibrium points) which corresponds to the change of parameters of the aircraft and the flight conditions. At the same time, the linear and nonlinear controllers are designed for the nominal trim point. The results are presented in Tables 4.4 and 4.5. The states' average RMSE and AMD are summarized for $\bar{t} = 2.14$ and $\bar{t} = 2.14$ and equilibrium points #7 and #8 which correspond to 27 m/s and 29 m/s (Figure 4.3). It is clear that

the nonlinear controller outperforms the linear one. However, this advantage is due to the usage of a higher amount of energy spent on the rudder deflection.

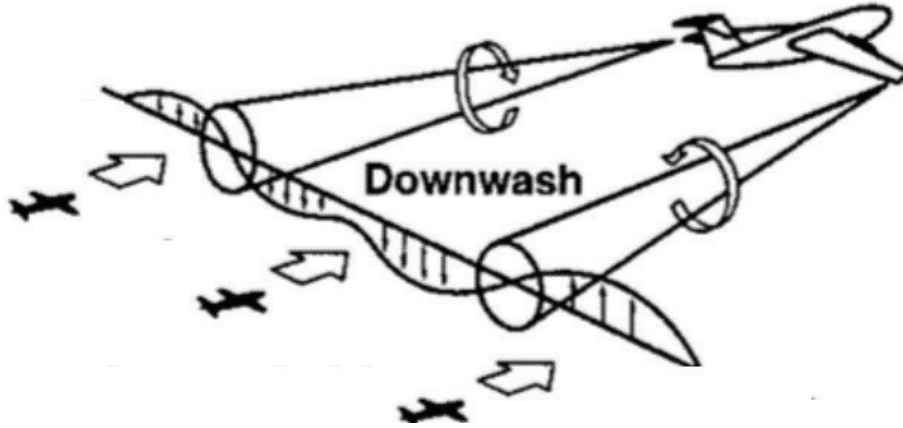


Figure 4.18: Generator aircraft and several positions of the follower aircraft.

Table 4.4: Average states' RMSE and Maximum Deviations of Deflection Surfaces over 400 Monte Carlo simulations. Equilibrium point #7. $\bar{t} = 3.84$

Controller type	$\Delta\phi, \text{deg}$	$\Delta\psi, \text{deg}$	$\Delta p, \text{deg/s}$	$\Delta r, \text{deg/s}$	$\Delta v, \text{m/s}$	ΔA_L	ΔA_R	ΔR
<i>Nonlinear</i> _{ARMSE}	1.88	0.03	5.5	1.49	0.22	0.69	0.69	1.07
<i>Linear</i> _{ARMSE}	2.2	0.9	6.24	2.6	0.22	0.88	0.87	0.3
<i>Nonlinear</i> _{AMD}	10.09	4.07	37.6	9.26	1	3.23	3.38	5.04
<i>Linear</i> _{AMD}	10.7	5.7	39.9	13.83	1.19	4.15	4.15	1.64

Table 4.5: Average states' RMSE and Maximum Deviations of Deflection Surfaces over 400 Monte Carlo simulations. Equilibrium point #8. $\bar{t} = 2.14$

Controller type	$\Delta\phi, \text{deg}$	$\Delta\psi, \text{deg}$	$\Delta p, \text{deg/s}$	$\Delta r, \text{deg/s}$	$\Delta v, \text{m/s}$	ΔA_L	ΔA_R	ΔR
<i>Nonlinear</i> _{ARMSE}	2.02	1.01	5.88	1.62	0.24	0.79	0.8	1.23
<i>Linear</i> _{ARMSE}	2.51	1.54	6.77	2.9	0.25	0.97	0.95	0.32
<i>Nonlinear</i> _{AMD}	10.8	4.5	39.85	9.82	1.01	3.55	3.85	5.58
<i>Linear</i> _{AMD}	11.89	6.6	43.27	14.75	1.36	4.54	4.55	1.77

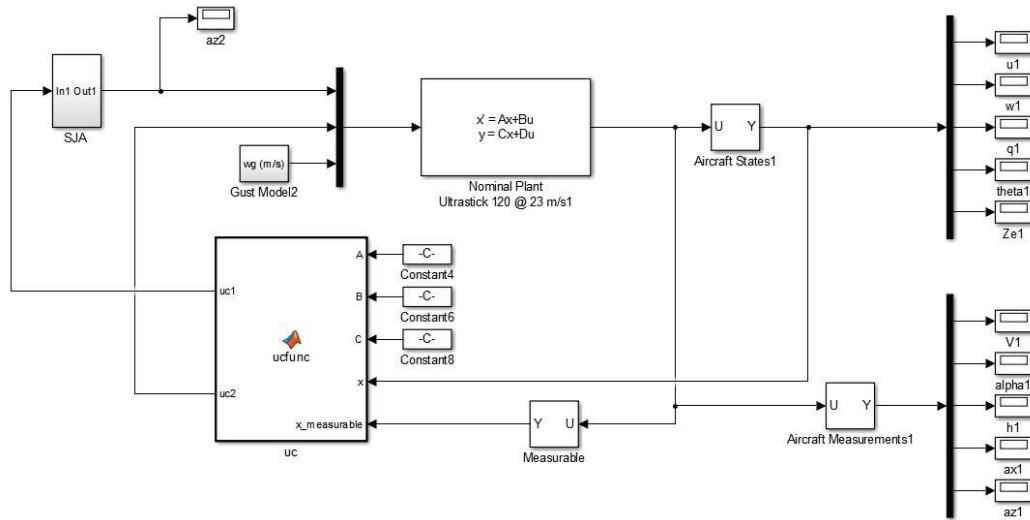


Figure 4.19: Simulink model diagram.

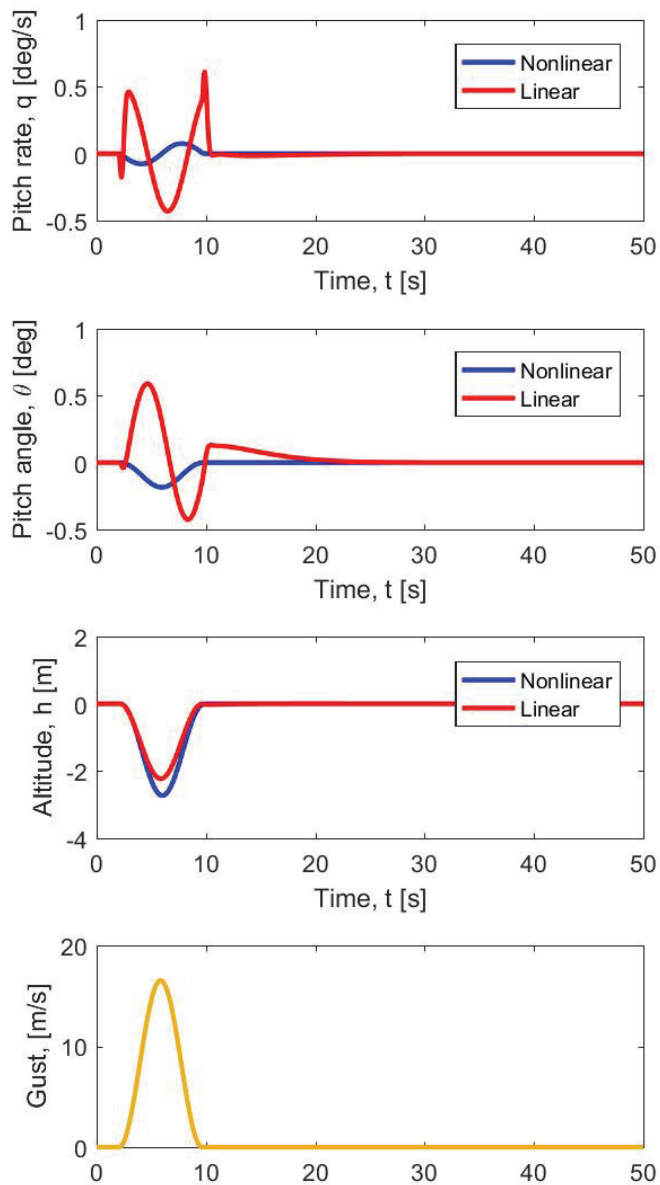


Figure 4.20: States deviations for nominal point (23 m/s point), 17 m/s gust.

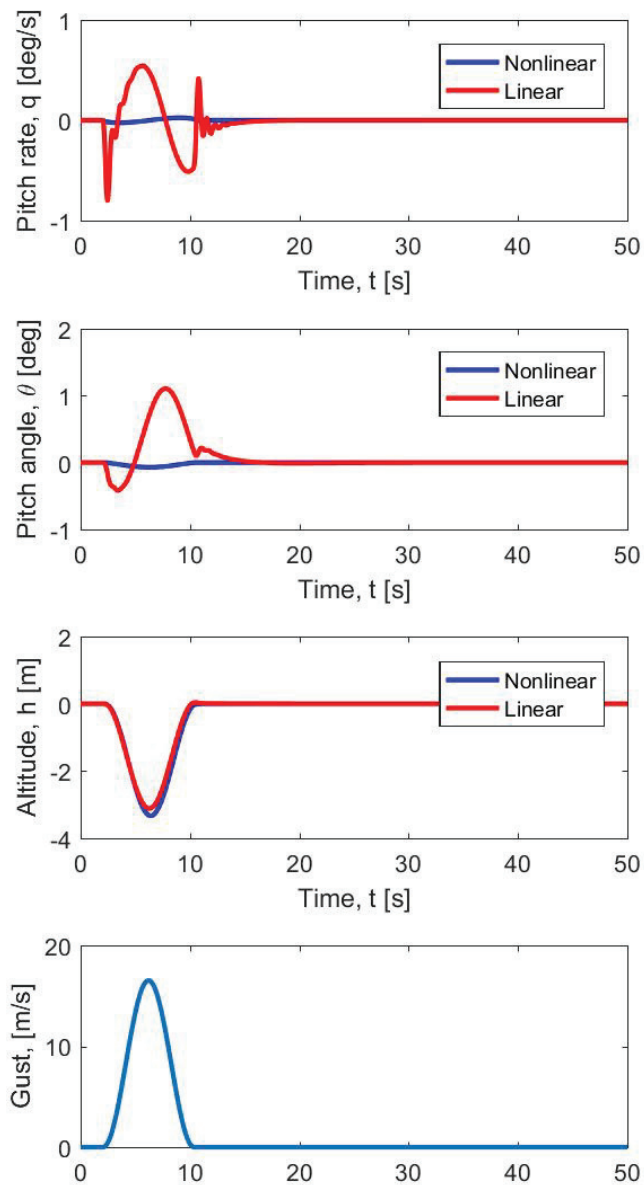


Figure 4.21: States deviations for 21 m/s point, 17 m/s gust.

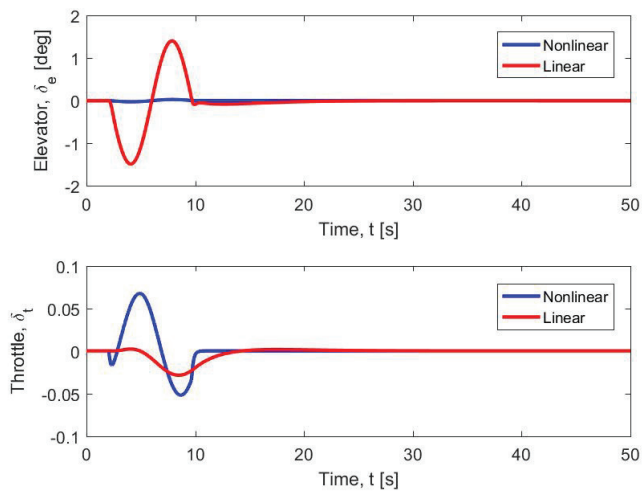


Figure 4.22: Control surface deviations for nominal point (23 m/s point), 17 m/s gust.

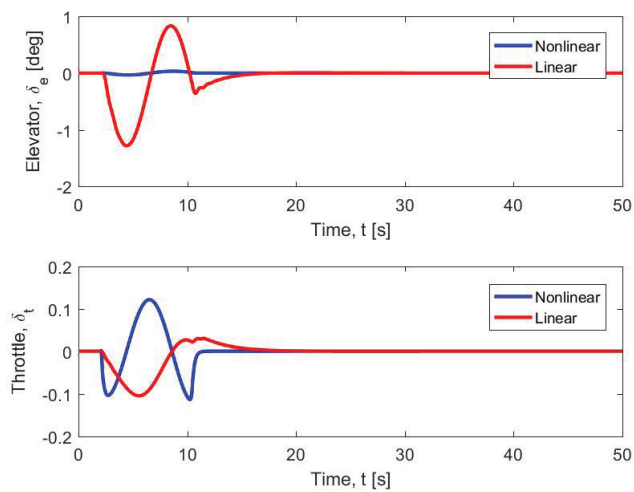


Figure 4.23: Control surface deviations for 21 m/s point, 17 m/s gust.

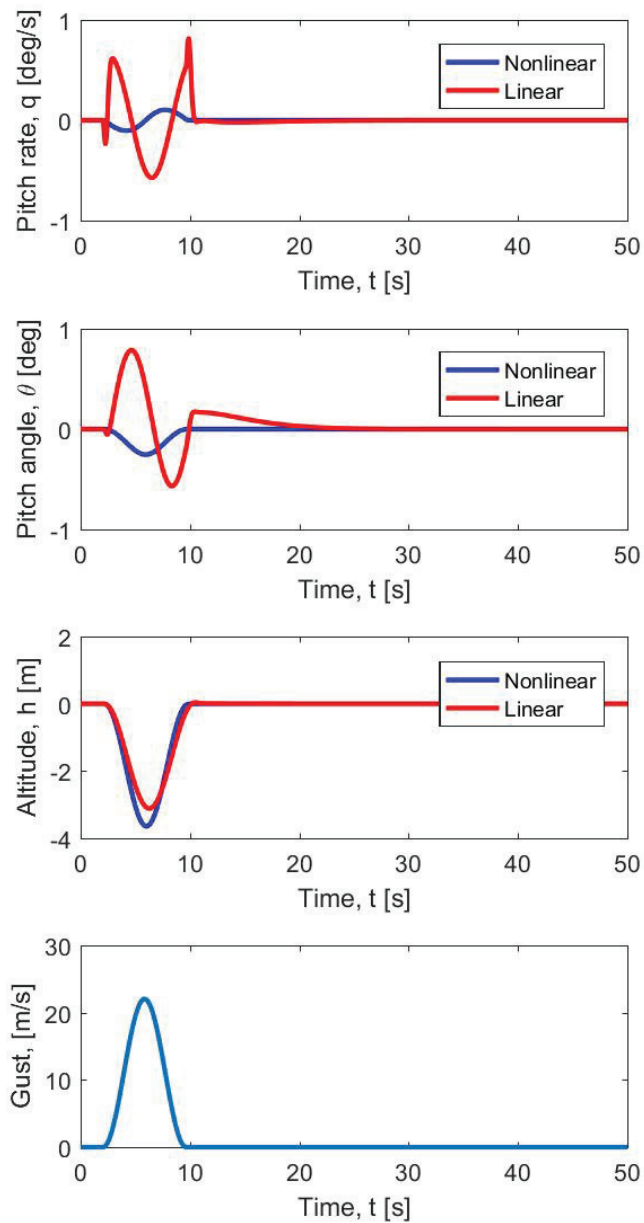


Figure 4.24: States deviations for nominal point, 23 m/s gust.

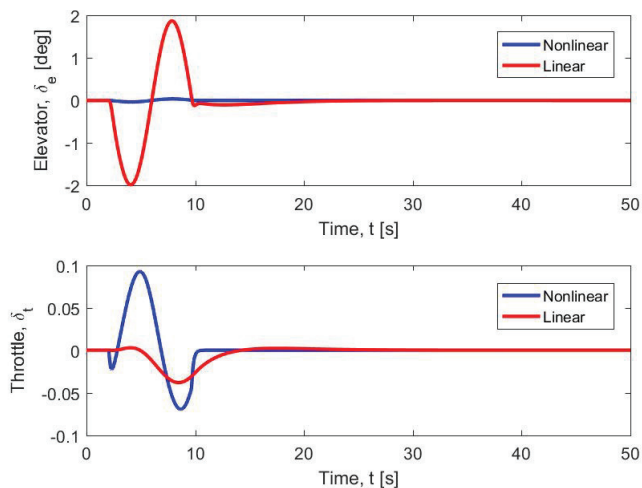


Figure 4.25: Control surface deviations for nominal point , 23 m/s gust.

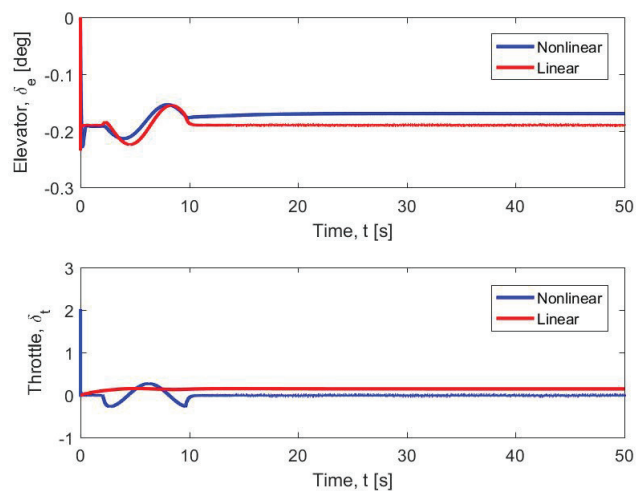


Figure 4.26: Control surface deviations for nominal point, 23 m/s gust, SJA case.

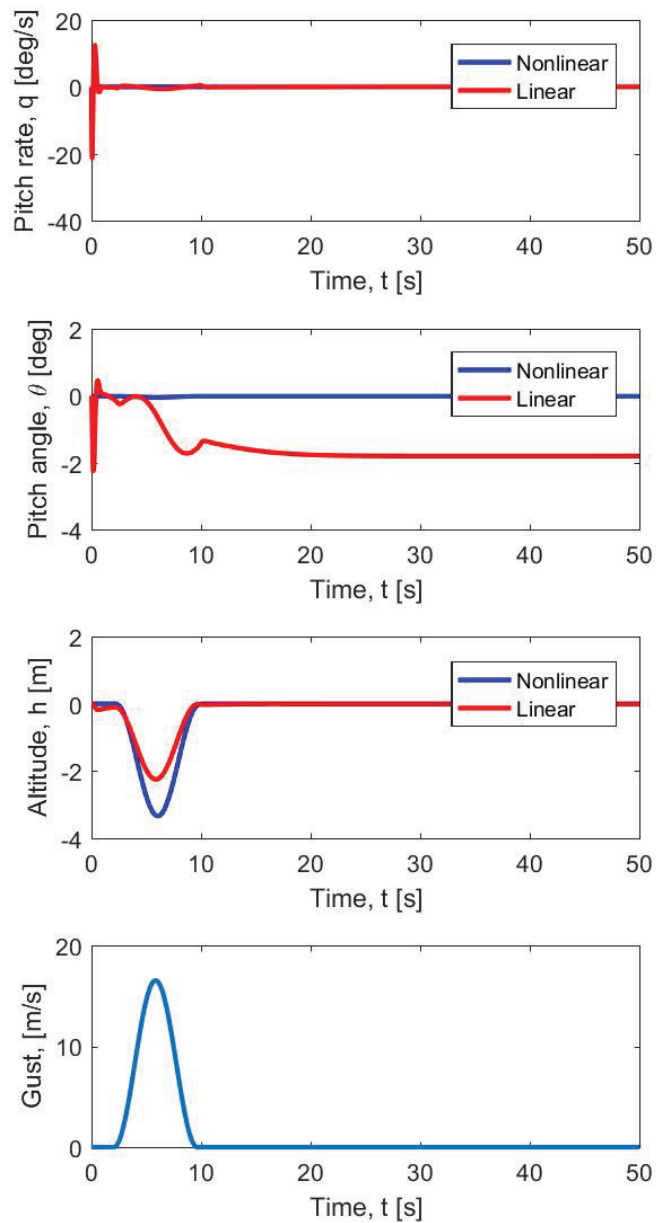


Figure 4.27: States deviations for nominal point, 23 m/s gust, SJA case.

5. CONCLUSION

The current work focuses on developing a variable-fidelity approach for addressing the safety of UAS operations in the NAS using the framework of simulation software SITAR WVSS. The latter is the dynamic low-fidelity model predicting generation, evolution, and interaction of aircraft wake vortices. The SITAR WVSS system consists of several sub-modules.

The “Generation” and “Evolution” sub-modules deal with wake vortex evolution and prediction of the position and strength of wake vortices in the atmosphere and atmospheric boundary layer using deterministic and probabilistic approaches. This part reported on validation studies performed for three probabilistic wake vortex evolution approaches implemented as part of WVSS code and compared against other existing models using Memphis’95 and Denver’03 data sets collected from LIDAR airport measurements. In terms of the overall success rates, the WVSS Monte-Carlo simulations outperformed APA 3.4, 3.8 and TDP 2.1 model predictions based on Memphis’ 95 dataset study and appeared close to the results from APA-TDP multi-model simulations. The implemented P2P and RMS based probabilistic approaches demonstrated better success rates compared to results from Monte-Carlo simulation. P2P and RMS based approaches are also easily implementable in any fast-time prediction model, require minimum input data and are numerically more efficient compared to the Monte-Carlo approach. On the other hand, they introduce wider bounds in the predicted cones of uncertainty for the evolution of wake vortex characteristics.

As for the evolution of wake vortex in the atmospheric boundary layer, the In-Ground LES simulations were conducted to investigate the transport and decay of the wake vortex pair in the vicinity of the hard surface, forest canopy (porous surface) and the water surface is studied and compared. The forest canopy and water surface were modeled by adding a porous and water subregions to the original computational domain. The case of the wake vortex propagation over the water surface is investigated using the VOF method. It is shown that the wake vortex evolutions over the hard and porous surfaces were similar in terms of the secondary vorticity production and vortex pair's dynamics. However, in the case of the porous surface, the jet entrainment affected the dynamics of the vortex pair. In the water surface case, the results appeared quite different from the hard and porous surface cases. Particularly, more intense turbulence generation is observed near the water surface during the wake vortex approach. As a result, the higher dissipation affected the wake vortex dynamics and decay.

The evolution of the wake vortex pair near different configurations of a forest canopy was also studied and compared using OpenFOAM LES simulations. Only the cases without ambient turbulence and formed atmospheric boundary layers were considered in this study. The change in the canopy height, the type of the forest canopy, canopy roughness, as well as the effect of the forest clearing on the wake vortex was investigated. The validation of the solver setup was performed against the experimental data.

Two configurations of the rough canopy were tested including the canopies formed with $3m \times 3m$ and $6m \times 6m$ cross sections. It was shown that the roughness triggers the formation of the secondary vorticity structures and has a great impact on the wake vortex strength decay. The effects of flat canopies of two heights were studied and compared. The dynamics of the vortex pair over the lower canopy was observed to be closer to that above the flat hard surface. The effect of the canopy clearing (i.e., a gap in the forest canopy) was shown to significantly change the dynamics of the vortex pair in comparison with the hard surface and forest canopy cases. The high-fidelity based low-fidelity in-ground effect model was developed, which can be incorporated into SITAR WVSS system. The results for the in-ground wake vortex propagation were compared to the results obtained using APA 3.8 model from NASA.

The “Interaction” sub-module is developed to simulate the wake vortex-aircraft interaction and assessing the operational safety risks. The assessment is based on examining the roll control ratios (RCR) of 3 variable-size UAVs (Osprey, Global Hawk, and Predator) induced by the wake of the leader B-737 aircraft. The impact areas were shown in terms of the vertical and horizontal offsets of the follower UAS with respect to the leader position. Three different autopilot response scenarios were further investigated including the time-delayed responses.

A robust nonlinear control method is developed as a part of the “Interaction” sub-module. It is proven to achieve altitude regulation in the presence of unmodeled external disturbances (e.g. wake vortices, wind gusts) and actuator

parametric uncertainty. A nonlinear UAV regulation control method is presented, which is proven to asymptotically regulate pitch angle and altitude in the presence of extreme wind gust disturbances. Detailed numerical simulation results were provided to demonstrate the performance of the proposed nonlinear control law. To provide a basis for comparison, the same control objective is simulated using a linear control law. It is shown that the nonlinear control method compensates for the wind gust disturbances significantly more effectively than the linear controller. Moreover, parameter variations in the state space model were introduced in the simulation. Both nonlinear and linear controllers were tested in the presence of uncertainty in the aircraft and SJA actuator dynamic model. The results showed that the nonlinear control design outperformed the linear control method for the simulated trajectory regulation objective under the tested levels of uncertainty.

Finally, the performance of the nonlinear controller is successfully tested in the presence of the wake vortex disturbance in the vicinity of the ground as well as far from the ground. The in-ground interaction was modeled using high-fidelity LES simulations, where the interaction with the secondary vorticity and turbulence is taken into account. The Monte-Carlo simulations for the out-of-ground interaction are performed based on the real cone of uncertainty for the wake-vortex. The performance of the nonlinear robust controller and H_∞ linear controller were compared for both in-ground and out-of-ground zone. The nonlinear controller outperformed the linear one in terms of average RMSE and AMD.

REFERENCES

- Ahmad, N. N., & Pruis, M. J. (2015). Evaluation of fast-time wake models using denver 2006 field experiment data. In *7th AIAA atmospheric and space environments conference* (p. 3318).
- Ahmad, N. N., VanValkenburg, R., Bowles, R., & Limon, F. (2014). Evaluation of fast-time wake vortex models using wake encounter flight test data. In *6th AIAA atmospheric and space environments conference*.
- Ahmad, N. N., VanValkenburg, R., Pruis, M., & Limon, F. (2016). NASA AVOSS fast-time models for aircraft wake prediction: User's guide (APA 3.8 and TDP 2.1).
- Aumond, P., Masson, V., Lac, C., Gauvreau, B., Dupont, S., & Berengier, M. (2013). Including the drag effects of canopies: real case large-eddy simulation studies. *Boundary-layer meteorology*, 1–16.
- Baranov, N., & Belotserkovsky, A. (2013). Modeling of vortex flight safety. *Nauka*(978-5-02-038083-7).
- Barker, S. J., & Crow, S. C. (1977). The motion of two-dimensional vortex pairs in a ground effect. *Journal of Fluid Mechanics*, 82(04), 659–671.
- Belcher, S., Finnigan, J., & Harman, I. (2008). Flows through forest canopies in complex terrain. *Ecological Applications*, 18(6), 1436–1453.
- Bitog, J. P., Lee, I.-B., Hwang, H.-S., Shin, M.-H., Hong, S.-W., Seo, I.-H., . . . Pang, Z. (2012). Numerical simulation study of a tree windbreak. *Biosystems engineering*, 111(1), 40–48.
- Burnham, D. C., & Hallock, J. N. (1982). *Chicago monostatic acoustic vortex sensing system. Volume IV. Wake vortex decay.* (Tech. Rep.). DTIC Document.
- Burnham, D. C., Hallock, J. N., Tombach, I., Brashears, M., & Barber, M. (1978). *Ground-based measurements of the wake vortex characteristics of a B-747 aircraft in various configurations.* (Tech. Rep.). Transportation Systems Center Cambridge Mass.
- Caraballo, E., Little, J., Debiassi, M., & Samimy, M. (2007). Development and implementation of an experimental-based reduced-order model for feedback control of subsonic cavity flows. *Journal of Fluids Engineering*, 129(7), 813–824.
- Cheng, M., Lou, J., & Lim, T. (2014). A numerical study of a vortex ring impacting a permeable wall. *Physics of Fluids*, 26(10), 103602.
- Crasto, G. (2007). Numerical simulations of the atmospheric boundary layer. *Universita degli Studi di Cagliari: Cagliari, Italy*.
- Deb, D., Tao, G., Burkholder, J. O., & Smith, D. R. (2005). An adaptive inverse control scheme for a synthetic jet actuator model. In *Proceedings of the 2005, American Control Conference, 2005.* (pp. 2646–2651).
- Deb, D., Tao, G., Burkholder, J. O., & Smith, D. R. (2006). Adaptive synthetic jet actuator compensation for a nonlinear tailless aircraft model at low angles of attack. In *2006 American Control Conference* (pp. 6–pp).

- Deb, D., Tao, G., Burkholder, J. O., & Smith, D. R. (2007). Adaptive compensation control of synthetic jet actuator arrays for airfoil virtual shaping. *Journal of Aircraft*, 44(2), 616–626.
- Deb, D., Tao, G., Burkholder, J. O., & Smith, D. R. (2008). Adaptive synthetic jet actuator compensation for a nonlinear aircraft model at low angles of attack. *IEEE Transactions on Control Systems Technology*, 16(5), 983–995.
- Delisi, D. P., Robins, R. E., & Pruis, M. J. (2016). APA 3.8 fast-time, numerical wake model description and first results. *American Institute of Aeronautics and Astronautics, AIAA Paper*.
- Dorobantu, A., Murch, A., Mettler, B., & Balas, G. (2011). Frequency domain system identification for a small, low-cost, fixed-wing uav. In *AIAA guidance, navigation, and control conference* (pp. 6–11).
- Dorobantu, A., Murch, A., Mettler, B., & Balas, G. (2013). System identification for small, low-cost, fixed-wing unmanned aircraft. *Journal of Aircraft*, 50(4), 1117–1130.
- Drakunov, S. V. (1992). Sliding-mode observers based on equivalent control method. In *Decision and control, 1992., proceedings of the 31st IEEE conference on* (pp. 2368–2369).
- Dubrasich, M. E., Hann, D. W., & Tappeiner I, J. C. (1997). Methods for evaluating crown area profiles of forest stands. *Canadian Journal of Forest Research*, 27(3), 385–392.
- Ergun, S. (1952). Fluid flow through packed columns. *Chem. Eng. Prog.*, 48, 89–94.
- Fayad, I., Baghdadi, N., Bailly, J.-S., Barbier, N., Gond, V., Hérault, B., . . . Perrin, J. (2016). Regional scale rain-forest height mapping using regression-kriging of spaceborne and airborne lidar data: application on french guiana. *Remote Sensing*, 8(3), 240.
- Freeman, P. M. (2014). *Reliability assessment for low-cost unmanned aerial vehicles* (Unpublished doctoral dissertation). University of Minnesota.
- Gavrilov, K., Accary, G., Morvan, D., Lyubimov, D., Méradji, S., & Bessonov, O. (2011). Numerical simulation of coherent structures over plant canopy. *Flow, Turbulence and Combustion*, 86(1), 89–111.
- Gerz, T., Holzäpfel, F., & Darracq, D. (2002). Commercial aircraft wake vortices. *Progress in Aerospace Sciences*, 38(3), 181–208.
- Ghisalberti, M., & Nepf, H. (2009). Shallow flows over a permeable medium: the hydrodynamics of submerged aquatic canopies. *Transport in Porous Media*, 78(2), 309–326.
- Gludemans, T., Van Lochem, S., Ras, E., Malissa, J., Ahmad, N. N., & Lewis, T. A. (2016). A coupled probabilistic wake vortex and aircraft response prediction model.
- Golubev, V., Kazarin, P., MacKunis, W., Borener, S., & Hufty, D. (2016). On safety assessment of novel approach to robust UAV flight control in gusty environments.
- Greene, G. C. (1986). An approximate model of vortex decay in the atmosphere. *Journal of Aircraft*, 23(7), 566–573.

- Hafsteinsson, H. E. (2009). *Porous media in OpenFOAM* (Tech. Rep.). Chalmers University.
- Harris, D., & Williamson, C. (2012). Instability of secondary vortices generated by a vortex pair in ground effect. *Journal of Fluid Mechanics*, 700, 148–186.
- Harvey, J., & Perry, F. J. (1971). Flowfield produced by trailing vortices in the vicinity of the ground. *AIAA journal*, 9(8), 1659–1660.
- Hirt, C. W., & Nichols, B. D. (1981). Volume of fluid (vof) method for the dynamics of free boundaries. *Journal of Computational Physics*, 39(1), 201–225.
- Holzäpfel, F. (2006). Probabilistic two-phase aircraft wake-vortex model: further development and assessment. *Journal of Aircraft*, 43(3), 700–708.
- Holzäpfel, F. (2014). Effects of environmental and aircraft parameters on wake vortex behavior. *Journal of Aircraft*, 51(5), 1490–1500.
- Holzäpfel, F., & Steen, M. (2007). Aircraft wake-vortex evolution in ground proximity: analysis and parameterization. *AIAA journal*, 45(1), 218–227.
- Kazarin, P., & Golubev, V. (2017a). Comparison of probabilistic approaches for predicting the cone of uncertainty in aircraft wake vortex evolution. In *9th AIAA atmospheric and space environments conference* (p. 4369).
- Kazarin, P., & Golubev, V. (2017b). On effects of ground surface conditions on aircraft wake vortex evolution. In *9th AIAA atmospheric and space environments conference* (p. 4368).
- Kazarin, P., & Golubev, V. (2018). High-fidelity simulations of terminal-zone heterogeneous terrain effects on aircraft wake vortex evolution. In *2018 AIAA aerospace sciences meeting* (p. 1279).
- Kazarin, P., Golubev, V., Provalov, A., Borener, S., & Hufty, D. (2016). A variable-fidelity approach to wake safety analysis in the context of uas integration in the nas. In *16th AIAA aviation technology, integration, and operations conference* (p. 3452).
- Kazarin, P., MacKunis, W., Moreno, C., & Golubev, V. (2017). Robust nonlinear tracking control for unmanned aircraft with synthetic jet actuators. In *AIAA atmospheric flight mechanics conference* (p. 3730).
- Kumar, N., & Jain, S. (2014). Identification, modeling and control of unmanned aerial vehicles. *International Journal of Advanced Science and Technology*, 67, 1–10.
- Lim, T., & Adhikari, D. (2015). The impact of a vortex ring on porous surfaces—a review. In *Vortex rings and jets* (pp. 33–60). Springer.
- Luckner, R., Höhne, G., & Fuhrmann, M. (2004). Hazard criteria for wake vortex encounters during approach. *Aerospace Science and Technology*, 8(8), 673–687.
- MacKunis, W., Subramanian, S., Mehta, S., Ton, C., Curtis, J. W., & Reyhanoglu, M. (2013). Robust nonlinear aircraft tracking control using synthetic jet actuators. In *52nd IEEE conference on decision and control* (pp. 220–225).
- Marshall, B. J. (1998). *Wind flow structures and wind forces in forests* (Unpublished doctoral dissertation). University of Oxford UK.

- McCormick, B. W. (1995). *Aerodynamics, aeronautics, and flight mechanics* (Vol. 2). Wiley New York.
- Meteorological and wake vortex data set, dallas-fort worth international airport. (1998). *NASA Langley Research Center*.
- Misaka, T., Holzäpfel, F., Gerz, T., Manhart, M., & Schwertfirm, F. (2011). Large-Eddy Simulation of wake vortex evolution from roll-up to vortex decay. In *49th AIAA aerospace sciences meeting including the new horizons forum and aerospace exposition* (p. 1003).
- Momentum equations for porous media*. (n.d.). <https://tinyurl.com/ya2yjf84>. (Online; accessed 14-May-2017)
- Mondschein, S. T., Tao, G., & Burkholder, J. O. (2011). Adaptive actuator nonlinearity compensation and disturbance rejection with an aircraft application. In *Proceedings of the 2011 American Control Conference* (pp. 2951–2956).
- Mueller, E., Mell, W., & Simeoni, A. (2014). Large eddy simulation of forest canopy flow for wildland fire modeling. *Canadian Journal of Forest Research*, *44*(12), 1534–1544.
- Natesan, K., Gu, D.-W., & Postlethwaite, I. (2007). Design of static H8 linear parameter varying controllers for unmanned aircraft. *Journal of Guidance, Control, and Dynamics*, *30*(6), 1829–1835.
- Nelson, R. C. (1998). *Flight stability and automatic control* (Vol. 2). WCB/McGraw Hill.
- Part, F. A. R. (2002). 25: Airworthiness standards: Transport category airplanes. *Federal Aviation Administration, Washington, DC*, 7.
- Proctor, F., Hamilton, D., & Han, J. (2000). Wake vortex transport and decay in ground effect-vortex linking with the ground. In *38th aerospace sciences meeting and exhibit* (p. 757).
- Proctor, F., Hamilton, D., & Switzer, G. (2006). Tass driven algorithms for wake prediction. In *44th AIAA aerospace sciences meeting and exhibit* (p. 1073).
- Proctor, F., & Han, J. (1999). Numerical study of wake vortex interaction with the ground using the terminal area simulation system.
- Raupach, M., Finnigan, J., & Brunet, Y. (1996). Coherent eddies and turbulence in vegetation canopies: the mixing-layer analogy. In *Boundary-layer meteorology 25th anniversary volume, 1970–1995* (pp. 351–382). Springer.
- Robins, R. E., & Delisi, D. P. (1993). Potential hazard of aircraft wake vortices in ground effect with crosswind. *Journal of Aircraft*, *30*(2), 201–206.
- Rood, E. P. (1994). Interpreting vortex interactions with a free surface. *Transactions-American Society of Mechanical Engineers Journal of Fluids Engineering*, *116*, 91–91.
- Rood, E. P. (1995). Vorticity interactions with a free surface. In *Fluid vortices* (pp. 687–730). Springer.

- Sarpkaya, T. (1996). Vorticity, free surface, and surfactants. *Annual Review of Fluid Mechanics*, 28(1), 83–128.
- Sarpkaya, T. (2000). New model for vortex decay in the atmosphere. *Journal of Aircraft*, 37(1), 53–61.
- Sase, S., Kacira, M., Boulard, T., & Okushima, L. (2012). Wind tunnel measurement of aerodynamic properties of a tomato canopy. *Transactions of the ASABE*, 55(5), 1921–1927.
- Schindler, D. (2004). *Characteristics of the atmospheric boundary layer over a scots pine forest*. Meteorologisches Institut der Universität.
- Schwarz, C., & Fischenberg, D. (2014). *Wake turbulence hazard analysis for a general aviation accident*. Deutsche Gesellschaft für Luft-und Raumfahrt-Lilienthal-Oberth eV.
- Shaikh, N., & Siddiqui, K. (2010). An experimental investigation of the near surface flow over air-water and air-solid interfaces. *Physics of Fluids*, 22(2), 025103.
- Shaw, R. H., & Schumann, U. (1992). Large-eddy simulation of turbulent flow above and within a forest. *Boundary-Layer Meteorology*, 61(1-2), 47–64.
- Singhal, C., Tao, G., & Burkholder, J. O. (2009). Neural network-based compensation of synthetic jet actuator nonlinearities for aircraft flight control. In *Proceedings of the AIAA guidance, navigation, and control conference, Chicago, IL, USA* (Vol. 1013, p. 119).
- Stephan, A., Holzäpfel, F., Misaka, T., Geisler, R., & Konrath, R. (2014). Enhancement of aircraft wake vortex decay in ground proximity. *CEAS Aeronautical Journal*, 5(2), 109–125.
- Suga, K., & Kuwata, Y. (2014). Turbulence over/inside porous surfaces and challenges to its modelling. In *Journal of physics: Conference series* (Vol. 530, p. 012004).
- Tchieu, A. A., Kutay, A. T., Muse, J. A., Calise, A. J., & Leonard, A. (2008). Validation of a low-order model for closed-loop flow control enable flight. *AIAA Paper*, 3863, 2008.
- Wallbank, T. (2008). Windsim validation study. *CFD validation in complex terrain*.
- Wang, J., Zhao, D., Schlüter, J., Holzäpfel, F., & Stephan, A. (2017). LES study on the shape effect of ground obstacles on wake vortex dissipation. *Aerospace Science and Technology*, 63, 245–258.
- Wang, J., Zhao, D., Schluter, J. U., Holzäpfel, F. N., & Stephan, A. (2016). Effect of ground obstacle of different aspect ratio on wake vortex dissipation. In *8th AIAA atmospheric and space environments conference* (p. 3134).
- Weigand, A., & Gharib, M. (1995). Turbulent vortex ring/free surface interaction. *Journal of Fluids Engineering*, 117(3), 374–381.
- Yu, Z., Qu, Y., & Zhang, Y. (2018). Safe control of trailing uav in close formation flight against actuator fault and wake vortex effect. *Aerospace Science and Technology*, 77, 189–205.

- Zak, J. (1996). Cases of interesting meteorological conditions during wake vortex measurements at memphis, tennessee during august 1995. *Vigyan Interim Report for NASA Contract NAS1-19341*.
- Zheng, Z. C., & Wei, Z. (2013). Effects of surface roughness and patterns on a surface-approaching pair of aircraft wake vortices. In *51st AIAA aerospace sciences meeting including the new horizons forum and aerospace exposition* (p. 364).
- Zhou, K., Doyle, J., & Glover, K. (1995). *Robust and Optimal Control*. Prentice Hall.